1-1-2017

Mri Methods For Imaging The Feto-Placental Vasculature And Blood

Uday Krishnamurthy
Wayne State University,

MRI METHODS FOR IMAGING THE FETO-PLACENTAL VASCULATURE AND BLOOD FLOW

by

UDAY BHASKAR KRISHNAMURTHY

DISSERTATION

Submitted to the Graduate School

of Wayne State University,

Detroit, Michigan

in partial fulfillment of the requirements

for the degree of

DOCTOR OF PHILOSOPHY

2017

MAJOR: BIOMEDICAL ENGINEERING

Approved By:

_____

Advisor Date

_____

_____

_____

_____

_____

DEDICATION

I dedicate this work to my parents and family

ACKNOWLEDGMENTS

The successful completion of my work would be incomplete without expression of gratitude to the people who have directly or indirectly helped me through my graduate work. Though words are not enough to express the sense of gratitude towards everyone who encouraged me in my endeavor this is only a humble attempt to do so.

First of all, I would like to express my sincere gratitude to Prof. Mark Haacke, and Asst. Prof. Jaladhar Neelavalli, for shaping me into who I am today. I thank them for their invaluable guidance and encouragement. They have given me the freedom to plan out strategies myself and for listening patiently to my ideas (even though some were not really feasible) and for correcting me time and again. Not many are fortunate to have such amazing mentors like you. I also acknowledge them for involving me in other projects and for helping me become an independent researcher.

I would like to thank my dissertation committee: Prof. Jeffery Stanley, Prof. Zhifeng Kou, Dr. Swati Mody and Dr. Edgar Hernendez for their guidance, the inputs and constructive criticism to help improve my work. I would like to extend a special acknowledgment to my clinical mentors Drs. Mody and Hernandez for patiently discussing and explaining the physiology of the fetal/neonatal life and its implications in diagnosis and management. I am also thankful to all the co-authors of my papers for their inputs and contributions.

I would also thank Drs. Yongquan Ye, Wei Feng, Charbel Habib, Yimin Shen, Sagar Buch, Norman Cheng, Lami Yeo and Sheena Saleem for the uncountable discussions and for their invaluable comments/suggestions. I am also deeply indebted to my colleagues and friends Zahid Latif, Brijesh Yadav, Pavan Jella and Yang Xuan for creating a relaxed working environment and for the days and moments we shared both on and off the academic settings. I was also fortunate to work with other staff members Lisa Brownchidle, Rachel Martis-Laze who were always accommodating and for putting up with my last minute requests. I also want to thank all the current and former colleagues at the MR Research Centre particularly Yashwanth Katkuri, Karthik Sekar, Ehsan Hamateai, Paul Kokeny, Anabella

Trifan, Maria Cabrera, Shadi Ehterami and Feifei Qu. I also thank Dr. Sagar Buch and Brijesh Yadav for proofreading my dissertation.

Needless to say, none of this would have been possible without the love and support from my family. My parents who have been a source of my confidence and for keeping me motivated at all times. And my sister, brother-in-law and my baby niece for their unconditional love, support and keeping me sane during this whole process.

Finally thanks to all those brave would-be mothers who volunteered for this study.

TABLE OF CONTENTS

LIST OF TABLES

LIST OF FIGURES

LIST OF ABBREVIATIONS

US:	Ultrasound
MRI:	Magnetic Resonance Imaging
MRS:	Magnetic Resonance Spectroscopy
MRA:	Magnetic Resonance Angiography
PC:	Phase Contrast
SWI:	Susceptibility Weighted Imaging
IUGR:	Intrauterine Growth Restriction
PI:	Pulsatality Index
SNR:	Signal to Noise Ratio
SAR:	Specific Absorption Rate
Ng-PCMRI:	Non-Gated Phase Contrast Magnetic Resonance Imaging
TOF:	Time-Of-Flight (TOF)
RF:	Radio Frequency
FSE:	Fast Spin Echo
CHD:	Congenital Heart Diseases
PET:	Positron Emission Tomography
CT:	Computer Tomography
SPECT:	Single Photon Emission Computer Tomography
FID:	Free Induction Decay
EMF:	Electromotive Force
SE:	Spin Echo
GE:	Gradient Echo
HASTE:	Half Fourier Acquired Single Shot Spin Echo
TE:	Echo Time

TR:	Relaxation Time
PE :	Phase Encode
ETL:	Echo Train Length
RARE:	Rapid Acquisition with Relaxation Enhancement
TSE:	Turbo Spin Echo
FOV:	Field-of-view
GRE:	Gradient Recalled Echo
DWI:	Diffusion Weighted Imaging
PWI:	Perfusion Weighted Imaging
BOLD:	Blood Oxygenation Dependent
SSFSE:	Single Shot Fast Spin Echo Sequence
ROI:	Region Of Interest
DICOM:	Digital Imaging and Communications in Medicine
IQR:	Inter Quartile Range
RI:	Resistance Index
STIC:	Spatiotemporal Image Correlation
CS:	Compressed Sensing
ICNIRP:	International Commission on Non-Ionizing Radiation Protection
IRB:	Institutional Review Board
FDA:	Food Drug Administration
IEC:	International Electrotechnical Commission

CHAPTER – 1: INTRODUCTION AND MOTIVATION

Fetal development is one of the most complicated and intriguing physiological process, which involves not only structural change but is also accompanied by increasing functional complexity of the systems. Ultrasound (US) imaging is the most common technique to probe the fetus and track the development in-utero. Fetal magnetic resonance imaging (MRI) in recent times has become a well-established adjunct to US in routine clinical prenatal care and diagnostics. Owing to ongoing research and development of advanced MRI routines, today we can visualize and image fine details of the growing fetus. A major thrust has been to understand structural changes in the brain (e.g. brain volumes, sulcation, gyration, and myelination patterns etc.) and other organs (e.g. volumes) [1, 2]. However, a similar understanding of the vascular system such as blood flow, blood oxygenation, vascular visualization …etc. in-utero has been limited. The primary focus of this thesis is to address this by optimizing and developing novel MR imaging sequences for vascular imaging in the human fetus.

1.1 MOTIVATION: Recent advances in MRI/US have made detection of many conditions possible in-utero. However clinical diagnosis/interpretation of fetal MRI is subjective and predominantly depends on tissue signal differences between normal and abnormal tissue. In majority of the fetal conditions, the tissue differentiation becomes appreciable only after the damage is irreversible. Under such conditions, it would be impossible to design clinical interventions to prevent/mitigate damage. Quantitative imaging, on the other hand, can help by providing objective measures which are indicative of the underlying biomolecular, microstructural and functional tissue characteristics that would precede any structural manifestation. Often these are the earliest measurable biomarkers of tissue injury, changes in metabolite concentration measured using magnetic resonance spectroscopy (MRS), blood flow visualized and quantified using magnetic resonance angiography (MRA) and phase contrast MRI (PCMRI), blood oxygenation quantified using susceptibility weighted imaging (SWI) are some of the quantitative measures that have already proven to be of use in early identification of injury in adult and pediatric populations [3, 4]. Even from a basic research standpoint, these techniques have enhanced our understanding of the normal physiology and to evaluate the dynamics of these processes in vivo [5, 6].

The following paragraph underscores the importance of quantitative fetal MRI in diagnosis and early detection of intrauterine growth restriction (IUGR), which is a serious condition that affects about 8-10% of babies in the USA and about 16% worldwide [7, 8]. IUGR is just highlighted here as a case in point to emphasize the importance of quantitative imaging.

IUGR is a serious perinatal condition that is associated with increased risk of neonatal mortality and serious short and long-term health problems and cognitive deficits [9, 10]. While the causal factors for IUGR are not clearly known, lack of sufficient supply of oxygen and nutrients to the developing fetus is considered to be the primary factor. Even with the use of advanced Doppler US (flow, biometric indices) assessments, only 15-25% of IUGR cases are detected prenatally in-utero [11, 12]. While our knowledge on the etiology is still evolving, based on studies performed in animal models (or ex-utero studies), reduction in oxygen and nutrient supply to the fetus results in adaptation of the placental vasculature [13, 14]. Following this there is a cascade of events, where this vascular remodeling leads to increased vascular resistance, which when crosses a threshold, manifests as flow abnormalities [15]. These changes reflect in an appreciable change in the pulsatility index (PI) and the flow indices can then be measured using Doppler US [16]. It would be ideal to diagnose this condition before vascular remodeling and hemodynamic fetal adaptation, following which there is little scope for clinical intervention and prevention. Under these conditions, oxygenation in the vessels supplying the fetus, and the blood flow may serve as a sensitive and potentially early marker for diagnosis of IUGR. Furthermore, these measures would also provide an objective way of clinical assessment. Hence vascular imaging is critical for early identification that could lead to better management of the pregnancy and individualized postnatal intervention which can help prevent neurodevelopmental deficits [17]. The key challenges in fetal MRI are the limited baseline signal, artifacts due to fetal motion and lack of standards regarding parameters and scanning protocols [18].

While the previous paragraph has focused exclusively on IUGR, the detection rate of some of the other prenatal conditions is also woefully low. For example, in-utero diagnosis of perinatal stroke is missed in most cases. 40% of these cases are diagnosed only outside the neonatal period or go undetected

until the babies present with neurological deficits or other symptoms [19, 20]. In fact, the needs and current limitations for early diagnosis across many other fetal anomalies and prenatal conditions are similar. While the need for quantitative MRI is evident, the practical implementation of this is limited due to multiple factors, the major ones being (a) requirement for sufficient signal to noise ratio (SNR) while concurrently having the need for high resolution imaging (b) requirement of fast approaches to avoid motion (maternal breathing, peristaltic motion in the maternal abdomen, pulsatility of the aorta/other major vessels and the unpredictable fetal motion) related artifacts (c) lack of standardization owing to rapidly changing local milieu (with changing gestation) and (d) the need to maintain low energy deposition (for safety concerns). As part of this thesis, we address some of these challenges by moving to higher fields, accelerating the scan time and optimizing the sequence parameters for fetal imaging.

1.2 SPECIFIC AIMS AND HYPOTHESIS:

In this proposal, MRI based vascular imaging techniques will be developed that can be applied in the human fetus for obtaining high quality in-utero data consistently. Accordingly, the specific aims and hypotheses are listed below:

Specific Aim 1: To improve the signal to noise ratio (SNR) in fetal imaging by migrating to higher field strength MRI, while lowering the energy deposition.

Hypothesis: Fetal MRI at 3.0 Tesla (T) can provide high resolution and high quality images compared to the standard clinical 1.5T MRI. This can be achieved by optimizing the sequence to minimize the specific absorption rate (SAR) while maintaining the SNR.

Specific Aim 2: To perform quantitative fetal flow imaging which is fast, accurate and does not need a cardiac/external trigger.

Hypothesis: It is possible to use non-gated phase contrast (ng-PCMRI) sequence to acquire flow data in a shorter time without the need for any trigger signal or need for complex post-processing algorithms.

Specific Aim 3: To develop a non-contrast enhanced MR angiography technique to image the vascular system of the fetus and the placenta.

Hypothesis: Time-of-flight (TOF) based non-contrast angiography can be optimized and applied on the fetus to visualize feto-placental vasculature

1.3 THESIS OUTLINE:

Although ultrasound (US) has been the primary modality used in prenatal diagnosis, the role of magnetic resonance imaging (MRI) in fetal diagnostic evaluation is increasing. Fetal MRI has multiple advantages over US in this field including improved soft tissue contrast and characterization and access to functional/quantitative data. The functional/quantitative data can almost exclusively be acquired only using MRI. It would be ideal to scan with high signal quality at higher image resolutions. However, imaging with high signal to noise (SNR) and imaging at a higher resolution are factors having conflicting demands. Currently, 1.5 T is the field strength of choice for MRI in pregnancy, although fetal MR imaging at 3.0T has been reported in several studies [21, 22]. The major advantage of 3.0T MRI (vs. 1.5T) is the increased SNR, which is linearly proportional to the imaging field strength. The 3.0T MRI has an operating frequency of 128 MHz (vs. 64 MHz of 1.5T), leading to higher radio frequency (RF) energy deposition. This increased SAR in pregnancy has limited the use of 3.0T MRI in fetal imaging. After a brief introduction to MRI and highlighting some of the sequences used in this thesis in chapter two, the techniques developed for fetal imaging will be discussed. The chapter three of this thesis tries to address the concerns of higher energy deposition by demonstrating the feasibility of fetal brain MRI using a fast spin echo imaging (FSE) sequence at 3.0T field strength with the simultaneous reduction in RF energy deposition while maintaining superior image quality compared to conventional 1.5T MRI. An appendix section of this thesis is also dedicated to discussing the local SAR and the temperature increase studied using simulations and the new advancements for patient specific SAR estimation.

Growth and development of the fetus are dependent on the functional maternofetal circulation. The human fetus receives nourishment, oxygen, metabolic wastes, and hormones through the umbilical vessels. The umbilical flow and flow dynamics are critically important for the normal growth of the developing fetus. Hence, evaluating the blood flow dynamics within the umbilical cord can provide valuable insights into the health of the fetus. Over the years Doppler US has been the workhorse tool for

studying the hemodynamics in the human fetus. But flow measurement, using this technique is challenging due to the irregular caliber/diameter and frequent twirl of the individual vessels owing to the braided structure of the umbilical cord, and the plug flow assumption. In recent years, PCMRI has been widely accepted as a clinical tool for assessment of flow dynamics and extensively used in adult diagnosis. But, this has not translated into applications in fetal imaging. In addition to issues of SAR and fetal motion, the application of PCMRI in the fetus is further hampered by the difficulty in measuring the fetal ECG or any other fetal physiological signal within the MRI scanner. In the fourth chapter, we demonstrate the feasibility of performing non-gated (ng- PCMRI) scans to measure the average flow in the umbilical vessels which eliminates the needs for a trigger and is comparatively fast.

Consistent application of the PCMRI methods and other quantitative methods like SWI for fetal blood oxygenation require a good technique to localize the vessels of interest. Even in vascular anomalies like congenital heart diseases (CHD), transposition of the great arteries …etc., it is vital to image the vascular system. Since the use of any exogenous contrast agent is a counter indication during pregnancy, we have to rely on other endogenous contrast mechanisms to image the vessels. TOF imaging which works on the intrinsic (T1) signal enhancement due to inflow effects would be a good fit given that the fetal blood flow is high. We optimized a non-contrast 2D TOF based sequence for fetal angiographic applications. In the fifth chapter, we demonstrate the feasibility of TOF imaging of the fetus and also briefly discuss the utility of non-Cartesian sampling in avoiding the artifacts caused due to motion.

Each of these chapters is presented independently wherein the research problem is introduced and our approach to address this is described. These chapters are followed by some concluding remarks and possible future directions of this work all bundled into the sixth chapter.

CHAPTER 2: INTRODUCTION TO MRI

This chapter gives a brief introduction to magnetic resonance imaging and also provides an overview of the different sequences discussed in the following chapters. The introduction and discussions are restricted to the key aspects relevant to the rest of the chapters in this thesis.

2.1 INTRODUCTION

MRI as a diagnostic tool was first introduced in the 1970s [23]. With rapid and continued technological and research advancements, it has since become an indispensable modality in clinical practice. Today, reports suggest there are about 10,000 MRI scanners installed across the USA, performing about 118 scans per 1000 people each year [24]. The MRI signal is generally obtained from hydrogen protons which are intrinsic and abundant in biological systems. MRI has many advantages, such as the ability to do 3D volume imaging, high-resolution scans, and the flexibility to obtain images of any cross-section as desired. However, the most important advantage of MRI compared to other imaging modalities such as positron emission tomography (PET), single photon emission computer tomography (SPECT), computerized tomography (CT) is the absence of ionizing radiation. Excellent soft tissue contrast and the ability to obtain different quantitative and/or functional parameters like relaxation times, diffusion, tissue perfusion, blood oxygenation and flow…etc which act as biomarkers for clinical manifestations, distinguish MRI from most other diagnostic modalities.

2.2 SIGNAL FORMATION

The following sections succinctly describe the basic signal formation and the concept of k-space that would be needed to comprehend the rest of the thesis. However, it is recommended to refer to more standard textbooks for a detailed description and understanding [25]. As mentioned earlier, the MRI signal is usually obtained from hydrogen protons. When the protons/hydrogen atoms are placed in an external magnetic field, in this case, the main magnetic field of an MRI scanner (B_0), they tend to preferentially align in the direction of the field due to their intrinsic magnetic moment ($\boldsymbol{\mu}$). However, due

to the intrinsic spin/angular moment ($\boldsymbol{J}$) of the proton, these protons precess around the main field direction at a rate referred to as Larmor frequency (ω_0). This is given by:

$$\overrightarrow{\omega_0} = \gamma\overrightarrow{B_0} \tag{2.1}$$

And intrinsic magnetic moment is given by $\boldsymbol{\mu} = \gamma J$ or in a form more relevant to MRI as

$$\frac{d\vec{M}}{dt} = \gamma\vec{M} \times \overrightarrow{B_0} \tag{2.2}$$

Because the net magnetization (M) is defined as the sum of all microscopic magnetic moments over a volume ($M = \boldsymbol{\Sigma}\ \boldsymbol{\mu}$). Where $\boldsymbol{\gamma}$ – gyromagnetic ratio (an intrinsic property of the nucleus in discussion, 42.58 MHz/T for a proton spin), and B_0 is the external magnetic field, M – net magnetization.

Consider a proton in a 3.0T MRI scanner (which is the setting used throughout this thesis), the Larmor frequency is 127.73 MHz. To interact with the protons precessing at this frequency, a small burst of a secondary electromagnetic field (B_1) is transmitted at this frequency and is called as the radio frequency (RF) pulse. This causes the net magnetization (M), of the spins to experience an angular deviation from the main field (B_0) by an angle referred to as flip angle and is given by $\boldsymbol{\theta} = \gamma B_1 \tau_{rf}$, Where $\boldsymbol{\theta}$ – flip angle (or) simply the angular deviation made by the net magnetic magnetization due to the RF pulse with respect to the main field (B_0), and τ_{rf} – duration of the RF pulse. Once this transient field is switched off, the magnetization returns to the equilibrium position along the main magnetic field (B_0). The relaxation rates or time constants of the relaxation in transverse and longitudinal directions are called as T_2 (spin-spin relaxation) and T_1 (spin-lattice relaxation) respectively. The recovery of the signal back to the main magnetic field with respect to time can be explained by the following mathematical equations.

$$\frac{\overrightarrow{dM}}{dt} = \gamma\overrightarrow{M} \,.\, \overrightarrow{B_{ext}} + \frac{1}{T_1}(M_0 - M_z)\vec{z} - \frac{1}{T_2}\overrightarrow{M_\perp} \tag{2.3}$$

Where M_0 is the equilibrium magnetization, $M_\perp$ is the transverse component of the magnetization. This changing magnetization along the transverse plane induces a small electromotive force (emf) in a coil which can be expressed as

$$\text{EMF} = -\frac{d}{dt}\int d^3r\vec{M}(\vec{r},t).B_{recieve}(\vec{r}) \tag{2.4}$$

This simple bulk signal from the sample, which is placed in a static magnetic field and excited by another RF pulse (short EM pulse), is referred to as FID signal or free induction decay. This FID is the basis for signal in MRI. The following sections describe the means to localize/obtain the spatial information from this bulk FID signal.

2.3 SPATIAL ENCODING/SIGNAL LOCALIZATION:

The bulk signal from the entire body must be isolated in three dimensions, to obtain any spatially localized information. This is achieved by manipulating the effective magnetic field seen by protons in different spatial locations. By application of magnetic field gradients, at specific times and in different directions spatial localization can be achieved.

2.3.1 Slice Select Encoding: To excite a slice (2D section) within the body, the magnetic field along the z-direction is made to linearly vary with respect to the distance from iso-center. Therefore, the frequency ω_0, which is required to excite the spins, can be tuned to match the spatial location of the spins. Consider, for example a linear gradient G_z applied along the z-direction of the magnet during excitation, a single slice can be excited by using the resonance frequency condition given by

$$\omega = (G_z Z + B_0) \tag{2.5}$$

In practice, this approach can be used to excite a single slice for 2D imaging applications or a volume for 3D volume imaging. However, exciting very thin slices require RF pulses (usually sinc) of broad width (based on the Fourier relation). Since this (temporally long RF pulses) is not practical, the Sinc pulses are truncated. Consequently, there is some leakage in excitation of the slice leading to non-rectangular slice profiles. This leads to crosstalk between successive slices and signal degradation in imaging. This challenge is easily overcome by using interleaved slice excitation's i.e. data from alternate slices are acquired in succession, while the previously excited slice has time to recover, leading to a homogeneous signal and no crosstalk. It is to be noted here that all 2D excitations described in this thesis are interleaved unless mentioned.

2.3.2 In-plane Encoding and k-space: Simply put, the use of gradients to modulate the precessional rates (ω) of spins along the same direction is referred to as frequency encoding. Often this is done along

the read direction and is interchangeably used with read-encoding. In the standard case of no additional gradients, the magnetization can be

$$M = M_0 \, e^{i\omega t} \tag{2.6}$$

Please note that the relaxation terms (T_1 and T_2) have been ignored for this discussion. Any additional linear gradient (with slope G) after the RF pulse starting at t = 0 would modify the angular frequency of the spins and can be written as:

$$\omega(x, t) = \omega_0 + \omega_G(x, t) \tag{2.7}$$

Where ω is the effective angular frequency and ω_G is the additional frequency term due to the presence of an external gradient. And, correspondingly the magnetization can be written as

$$M(x,t) = M_0(x) \, e^{(i\omega_0 t + \omega_G(x,t))} \tag{2.8}$$

The phase or angular displacement ($\boldsymbol{\varphi} = \omega t$) that is accumulated from the additional linear gradients, would be a time-varying spatially dependent value

$$\boldsymbol{\varphi} = \int_0^t \omega_G(x,t)d\tau = \int_0^t \gamma G(\tau).x \, d\tau$$

$$= \boldsymbol{\gamma} \int_0^t G(\tau)d\tau \, . x \; = 2\pi \, . K(t) \, . \, x \tag{2.9}$$

Where *K* corresponds to the k-space and is given by

$$K = \frac{\gamma}{2\pi} \int_0^t G(\tau) \, d\tau \tag{2.10}$$

This precessing magnetization induces a voltage in the receive coils and is given by

$$V(t) = Ç \int_0^t M_0(x) e^{i(\omega_0 t + \omega_G t)} d\tau$$

$$= Ç \int_0^t M_0(x) e^{i(\omega_0 t + 2\pi K_x(t))} dx) \tag{2.11}$$

Where the spatially invariant components and any other hardware coefficients (electronic gain terms) are included in the constant Ç. Since the Larmor frequency (ω_0) is known, the acquired voltage can be demodulated and the signal represented by

$$S(t) = Ç \int_0^t \rho(x) e^{i\omega_G \tau} \, d\tau$$

$$= Ç \int_0^t \rho(x) e^{-i2\pi K(t)x} \quad dx \tag{2.12}$$

If the above equation is carefully observed, it can be deduced that it is nothing but the Fourier transform of the proton density ($\boldsymbol{\rho}$(x)). While the above equation represents the signal behavior along one axis, in practice the signal and the k-space is a three-dimensional entity and the signal can be represented as

$$S(k_x,k_y,k_z) = \int \rho(x,y,z) e^{-i2\pi(K_x x + K_y y + K_z z)} dx dy dz \quad (2.13)$$

Where $K_x = \frac{\gamma}{2\pi} G_x t$; $K_x = \frac{\gamma}{2\pi} G_x t$; $K_x = \frac{\gamma}{2\pi} G_x t$ And from this the image can be reconstructed as

$$\boldsymbol{\rho}(x,y,z) = \int S(k_x,k_y,k_z) e^{i2\pi(K_x x + K_y y + K_z z)} dk_x dk_y dk_z \quad (2.14)$$

This is nothing but the inverse Fourier transform of the obtained voltage signal (S).

From the definition of K (K_x, K_y, K_z) it is evident that the position on the k-space is dependent on the slope of the linear gradient the spatial location and the time. By varying these independently or collectively along all the three axes we can move along the k-space to different points. The movement along the k-space is called as k-space trajectory. And this would determine the reconstruction method needed. Random, non-linear trajectories do not ensure that the data collected can be reconstructed by simple 2-dimensional or 3-dimensional Fourier transforms, e.g. as is the case of radial trajectory.

2.3.3 Sampling: In the conventional and widely used Cartesian k-space trajectory, the k-space is traversed in a raster format line-by-line. Here the data is sampled uniformly and can be easily reconstructed by inverse Fourier transformation along each direction sequentially. This results in a complex image which can be represented as a magnitude image and the phase image. Commonly the phase image is discarded, however depending on the application it might hold valuable information. As the data is encoded in Fourier space and is reconstructed using Fourier transformation, the reconstruction quality and artifacts thereupon are also dependent on the properties of the Fourier transforms. The original Fourier transform is defined over continuous space/analog space. However, our data in k-space is sampled discretely. This can be mathematically written as the analog signal convolved with a comb function (infinite series impulse function) in the Fourier space. This convolution produces a function which is a self-replicating signal each separated by the reciprocal of the spacing of the comb function.

$$\frac{1}{\Delta K} = L = FOV \quad (2.15)$$

This is referred to as the Nyquist sampling rate along read direction in MRI. This relationship applies along all three orthogonal directions.

2.4 BASIC MRI SEQUENCES:

For the most part, in the above introduction to MRI, the magnetic relaxation times have been ignored. The emf that is detected in the coil is in fact modulated by the relaxation properties of the tissues being imaged. While the signal decay over time is generally attributed to the T2 – decay, the dephasing of the magnetization caused by field inhomogeneities leads to an additional damping of the signal and the net decay can be modeled using T2*. In many practical cases, the T2' (additional damping due to non-uniform fields) are very small and dominate the T2 decay causing high signal loss. Fortunately, these additional T2' signal loss can be reversed using an additional π-pulse, this approach is referred to as spin echo (SE). The following section discusses the basics of spin echo (SE) and gradient echo (GE) sequences followed by a fast version of the SE referred to as HASTE (Half Fourier acquired single shot spin echo).

2.4.1 Spin Echo (SE) Sequence: Following the initial excitation, the longitudinal magnetization signal drops exponentially at the rate of T2*, which is a combination of the irreversible spin relaxation (T2) and a reversible component due to field inhomogeneity (T2'). Using a combination of an excitation pulse ($\pi/2$ - pulse) and a refocusing pulse (π - pulse) the T2' signal loss can be recovered. Due to magnetic field inhomogeneity following the 90^0 pulse, there is a loss of phase among the spin isochromats. An 180^0 pulse applied after a time τ, reverses the phase loss and progressively the isochromats come in-phase to form an echo at 2τ (fig 2.1). The main advantage of SEs is the greater immunity to artifacts from off-resonance affects e.g. B_0- field disturbances or susceptibility related fields. Specifically for heavy T2-weighting a long echo time (TE) and long repeat time (TR) are used, the acquisition time for a 2D slice is given by

$$T_{acq} = TR \times N_{PE} \tag{2.16}$$

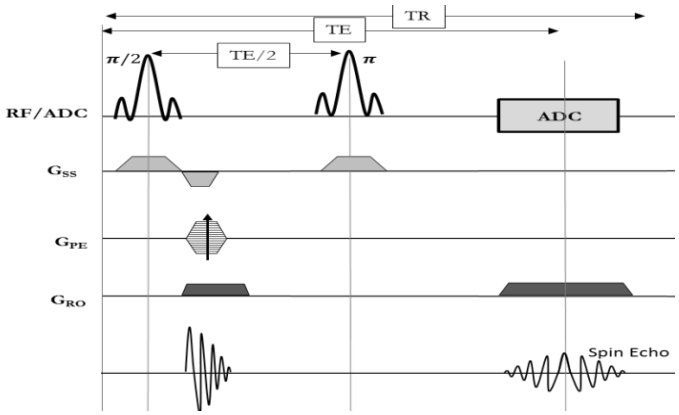

Figure 2.1: Simple schematic sequence diagram of a spin echo sequence

For an image of 256 phase encode (PE) lines and a TR of about 2000ms, the time required to collect a single slice is about 8.5 min. This long scan times with huge dead times between the echo and the next RF pulse has led to the development of multi-echo spin echo. In this dead time the experiment is repeated and data of the same slice at a different echo is collected. Hence within a TR images corresponding to multiple different echos are reconstructed. It was hence possible to have multiple echos of the data within the same scan time.

2.4.2 Gradient Echo (GE) Sequence: Gradient echoes do not use additional RF pulses for refocusing and creating the echo. Instead, the FID signal is manipulated by first forcing a faster decay using an external dephasing gradient. The dephasing gradient is usually applied along the frequency encoding axis and this creates slightly different local fields across the spatial field-of-view (FOV) causing an accelerated dephasing. Then they are rephased with a similar gradient (rephasing gradient) but with opposite polarity (fig 2.2). An echo occurs when the areas of the two gradients (dephasing and rephasing) areas are equal. Hence this is often also referred to as gradient recalled echo (GRE). It is important to note that the rephasing gradient only refocuses the spin isochromats that were initially dephased by the external gradient, the intrinsic T2, and T2* signal decay are not affected and cannot be recovered. A smaller area of the dephasing gradient can be used to create a partial echo.

GE's are faster than SE because only one RF pulse is applied per TR and the TE can be short. Practically, they are further accelerated by the fact that the excitation flip angle is less than 90^0, whereby

the magnetization is not fully inverted to the transverse plane and the time for T1 recovery is very quick (leading to shorter TR). This short TE and short TR create a unique hyperintense blood signal. Combining this with the time-of-flight (TOF) effect forms the basis of many angiography techniques.

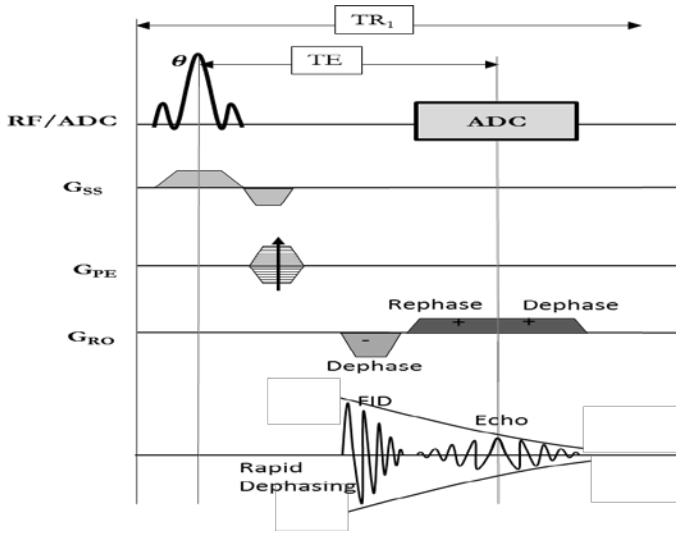

Figure 2.2: Simple schematic sequence diagram of a simple gradient echo sequence. Note the changes in the intensity of the signal due to the dephasing gradient and the echo formation when the areas of the dephasing and rephasing gradient are equal.

2.5 HASTE Sequence (Half Fourier Acquired Single Shot Spin Echo):

As described earlier, the use of long TRs for a SE echo sequence can be used to our advantage and collect multiple echoes. Henning in 1986 [26] described an approach (fig 2.3), wherein unlike a multi-echo spin echo sequence, each of the echoes is independently phase encoded so that multiple k-space lines can be acquired within a TR. The 180^0 pulses are repeatedly used to refocus the spins to create series of echoes. This process is called as echo train imaging, and the number of echoes obtained within a TR is called as echo train length (ETL). The spin echoes are refocused at echo times represented by TE_1, TE_2, TE_3, … etc. Each echo fills out its own independent k-space of the same slice. Because of the 180^0 pulse, the images from the even and odd numbered echoes are flipped in the PE direction. This approach is widely accepted as RARE (Rapid acquisition with relaxation enhancement) or Turbo spin echo (TSE)

or Fast spin echo (FSE) [27]. Compared to the spin echo the acquisition time of a 2D slice is lower by a factor of the ETL. One of the main difficulties of long ETL (enough to do single shot imaging) is the signal decay due to T2 during the echo train, i.e. after a few echoes there is no magnetization left in the transverse plane; this limits the practical ETLs possible. Another concern of the decay is that successive echoes are acquired with different signal intensities depending on the transverse relaxation and the echo spacing (ΔTE). This causes a blurring in the PE direction.

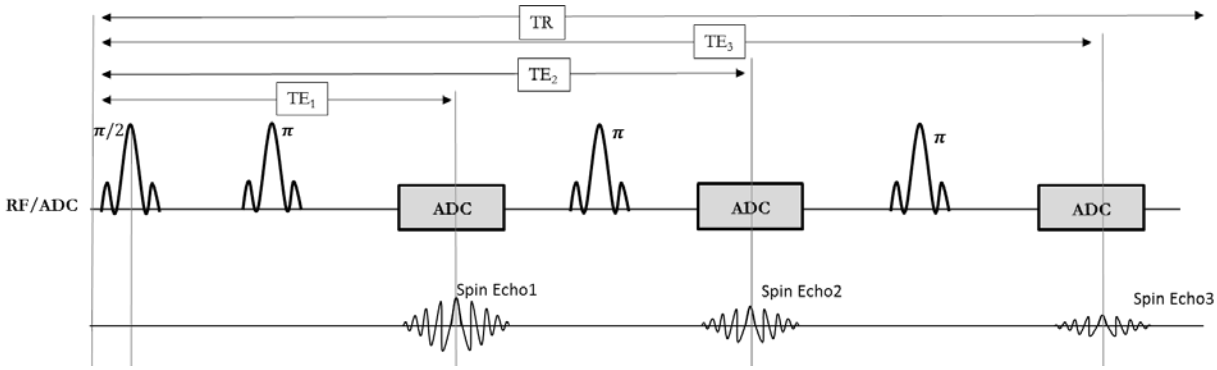

Figure 2.3: Simple schematic sequence diagram of a multi-echo spin echo sequence. Only three echoes are shown here but the actual number is only limited by the T2 of the sample.

To overcome these issues, TSE/RARE is often combined with half-Fourier techniques which reduce the number of PE required to reconstruct the image by half, hence the name HASTE [28]. In addition, the acquisition is combined with parallel imaging to further reduce the PE lines required. For example, consider an image to be reconstructed with 256 PE lines. With the use of half-Fourier approaches, the image can be reconstructed with 128 PE lines. Further using parallel imaging factor 2 the PE lines can be reduced to 64 and considering the auto calibration lines (~32) we would need 88 lines. Under practical brain imaging conditions the T2 of the tissue range from 40ms to 150ms, which limits the maximum possible longest echo to about 400ms (~ 5T2). Given the use of partial Fourier to enable shorter TE, about 96 echoes can be incorporated within 400ms. Hence the 2D image can be acquired in a single shot. The use of shorter echoes is also advantageous as there is a smaller difference of the signal intensities between the successive PE lines. Using all these approaches, a 2D slice using HASTE can be

acquired in a matter of 3-4 sec at 3.0T and hence is the most commonly used sequence in fetal imaging. However, the series of refocusing pulses carries considerable RF energy and might be a concern at higher fields.

2.6 PHASE CONTRAST MRI:

Gradient-echo (GE) MRI is sensitive to any sort of field perturbations, including motion. For most standard imaging sequences, the flow/velocity induced phase loss is eliminated by nulling the first moment of the gradients i.e. the integral of the product of time and gradient amplitude is made zero at the echo. However, instead of completely nulling this moment, we can modulate the gradient structure such that the constantly moving spins accumulate a known phase at the echo. Phase contrast (PC) is this approach of imaging the moving spins by applying specific flow-encoding gradients. The flow encoding gradient structure is usually a bipolar structure inserted after the slice select (for flow encoding in the slice direction). However it can be applied on any of the axes. Hence the spins moving with a constant velocity v along the direction of the encoding-gradient will develop a phase

$$\phi_{v\pm} = \pm \boldsymbol{\gamma G v \tau^2} \tag{2.17}$$

Where G is the amplitude of the gradient and τ is the duration of constant gradient. It is important to note that in the above relation the phase is directional dependent and is based on both the order of the bipolar and the direction of the motion of the spins. Given that there are other sources that induce a phase in the images, the PC sequence is used to acquire two set of images with the same imaging parameters except for the opposite bipolar gradients. These two set of complex images are then subtracted. This subtraction serves the dual role of accentuating the flow signal while suppressing all other sources of phase contributions.

2.7 TIME-OF-FLIGHT MRI:

Under standard imaging, the spins approach steady state equilibrium signal intensity when they are exposed to multiple RF pulses. However, when a moving spins like the ones in moving blood do not see the same number of RF pulses they do not approach steady state, a phenomenon called as inflow effects. This difference in the saturation of the background static signal and the moving blood signal

causes a contrast between them and enables us to perform magnetic resonance angiographic (MRA) imaging. For optimal inflow affects, the slice thickness must be so chosen that all the pool of the blood in that slice is completely refreshed before the next RF excitation i.e. v*TR > TH. (v – velocity of blood, TR – relaxation time; TH – slice thickness) Since the approach to equilibrium is governed by the T1 of the sample, optimal signal differences can be observed when a flip angle closer to the Ernst angle ($\boldsymbol{\theta} \sim \sqrt{\frac{2TR}{T1}}$) is used. The enhanced signal from moving spins can be understood as a tissue with a shorter T1.This pseudo T1 can be represented as $T1_{flow} = \frac{TH}{v}$ and the effective T1 is given by

$$\frac{\mathbf{1}}{\boldsymbol{T1_{eff}}} = \frac{\mathbf{1}}{\boldsymbol{T1}} + \frac{\mathbf{1}}{\boldsymbol{T1_{flow}}} \tag{2.18}$$

Most TOF MRA based sequences uses short TE, short TR flow compensated spoiled gradient echo sequences. Other approaches of performing MRA include the use of contrast agents (works by decreasing the effective T1 of the blood pool) or using selective tagging pulses. For optimal contrast the choice of MRI sequence parameters depends on the velocity of the blood flow.

CHAPTER – 3: FETAL BRAIN IMAGING AT 3.0T: A COMPARISON OF IMAGE QUALITY AND SPECIFIC ABSORPTION RATE [1]

This chapter discusses a work where the HASTE MRI sequence was modified to lower the energy deposited during the scan at 3.0T. Quality (quantitative and diagnostic) assessments were also performed to understand the implications of these sequence adaptations and all results were compared with standard scans at 1.5T field strength.

3.1 INTRODUCTION

While ultrasound has been the primary modality used in prenatal diagnosis the role of magnetic resonance imaging (MRI) in fetal diagnostic evaluation is increasing [29]. Fetal MRI has multiple advantages over ultrasound in this field.[30-63] Such advantages include: 1) improved soft tissue contrast and characterization [32, 48, 64-66]; 2) access to functional data [e.g. diffusion weighted imaging (DWI), [67-75] perfusion weighted imaging (PWI) [39, 59, 76, 77], blood oxygenation dependent (BOLD), [78-82] MR spectroscopy (MRS) [37, 83-92]]; and 3) larger field of view (FOV). Fetal MRI has been shown to be useful in the diagnosis of fetal pathologies [93-95]. In particular, fetal MRI has been shown to be superior to ultrasound in evaluating the fetal central nervous system. [32-34, 43, 44, 96-104]

Three decades have passed since the first application of MRI in the human pregnancy. [105] Currently, 1.5 Tesla (T) is the field strength of choice for MRI in pregnancy, although fetal MR imaging at 3.0T has also been reported in several studies. [82, 100, 106-109] Adult, pediatric, and neonatal populations routinely undergo clinical MR examinations at 3.0T. [110-113] The major advantage of 3.0T MRI (vs. 1.5T) is the increased signal to noise ratio (SNR), which is linearly proportional to the imaging field strength. Demonstrated benefits of such increased signal include 1) higher imaging resolution; 2) shorter imaging time; 3) improved tissue biochemical profiling through MRS, and 4) improved functional data.[114-117] However, susceptibility related artifacts are more pronounced at 3.0T MRI than 1.5T. [115-117] More importantly, 3.0T MRI has an operating frequency of 128 MHz (vs. 64 MHz of 1.5T),

[1] This work has been published: "**Krishnamurthy, Uday**, et al. "MR imaging of the fetal brain at 1.5 T and 3.0 T field strengths: comparing specific absorption rate (SAR) and image quality." Journal of perinatal medicine 43.2 (2015): 209-220". All contents and results are thereupon reproduced from this manuscript.

leading to higher radiofrequency (rf) energy deposition. [118-120] Specific absorption rate (SAR) measures energy deposition and is defined as rf power absorbed per unit mass of the tissue (Watts/Kg). [121-123] This issue of increased SAR in pregnancy has limited the use of 3.0T MRI in fetal imaging. [100, 109] Yet, radiofrequency energy deposition (SAR) can be reduced through pulse sequence modifications. [124-127] Therefore, we hypothesized that by using modified pulse sequences, imaging the fetal brain at 3.0T (vs. 1.5T) could be performed at a higher resolution with improved image quality, while simultaneously reducing the SAR.

The objectives of this study were to: 1) evaluate the feasibility of fetal brain MRI using a fast spin echo imaging sequence at 3.0T field strength with simultaneous reduction in radio frequency (rf) energy deposition; 2) quantitatively compare the image quality with conventional 1.5T MRI, and 3) compare tissue contrast and conspicuity for specific anatomical structures in the brain between 1.5T and 3.0T MRI.

3.2 MATERIALS AND METHODS

Pregnant women (19-40 weeks of gestation) scheduled to undergo a 1.5T MR exam for clinical indications were approached to also undergo a 3.0T exam afterwards. All women recruited as part of this study were referred for a clinical MRI through Hutzel Women's Hospital in Detroit, MI. The 1.5T MRI scans were performed at Children's Hospital of Michigan, Detroit, MI, while 3.0T MRI scans were performed at Wayne State University's Magnetic Resonance Research Facility at Detroit Medical Center, Detroit, MI. All women were enrolled in a research protocol approved by the Human Investigation Committee of Wayne State University, and all participants provided written informed consent for the use of MR images for research purposes.

3.2.1 MRI Examination: To compare the image quality and SAR between 1.5T and 3.0T MR, the T2 weighted single shot fast spin echo sequence (SSFSE) was chosen, since it is the most frequently acquired sequence for evaluating fetal anatomy, and has the highest SAR values in typical fetal MRI protocols. [128].

Clinical MRI scans were performed on a 1.5T General Electric Signa system (Milwaukee, WI) with an 8 channel cardiac array and spine receive coils. Following the scout/localizer scans, anatomical

data of the fetal brain were acquired using a T2 weighted SSFSE technique with the following imaging parameters (Table 3.1): repeat time (TR) 1192-1240 milliseconds (msec), echo time (TE) 90 - 240 msec, slice thickness of 4 mm, voxel size 0.93 x 0.93 mm^2 - 1.3 x 1.3 mm^2, and flip angle 90^o. Images were obtained sequentially in three planes (axial, coronal, and sagittal) relative to the fetal brain. Acquisitions were repeated when fetal motion was encountered.

Field Strength	**TE (msec)**	**TR (msec)**	**Resolution (mm^3)**	**Flip Angle (degree)**	**Band width (Hz/pixel)**
1.5 T	90 - 240	1192-1240	(0.93 to 1.3) x (0.93 to 1.3) x 4	90	244
3.0 T	139-140	2600-5000	(0.87 to 1.1) x (0.87 to 1.1) x (3 to 4)	75	369 or 372

Table 3.1: MR imaging parameters for the single shot fast spin echo (SSFSE) sequence at 1.5T and 3.0T.

All 3.0T MRI scans were performed on a 3.0T Siemens Verio system (Erlangen, Germany) with a 6 channel body flex array and spine receive coils. An additional 2 channel flex extremity receive coil was used in some patients having a larger abdominal girth. Following scout/localizer scans, a T2 weighted single-shot turbo spin echo sequence with half-Fourier reconstruction (HASTE) was acquired for anatomical purposes. This sequence implementation is essentially the same as SSFSE on the GE system. [129] The following imaging parameters were used for the HASTE sequence: repeat time (TR) 2600-5000 milliseconds (msec), echo time (TE) 139-140 msec, slice thickness of 3 or 4 mm, voxel size 0.87 x 0.87 mm^2 - 1.1 x 1.1 mm^2, and flip angle 75^o with hyper-echo acquisition. Images were obtained sequentially in three planes (axial, coronal, sagittal) relative to the fetal brain. Acquisitions were repeated when fetal motion was encountered.

3.2.2 Data Analysis: T2 data was first reviewed for general image quality, including image or motion artifacts. From data collected at a given field strength, the best dataset (defined as a volume without motion or image artifacts) for each anatomical plane relative to the fetal brain was chosen for further

analysis. Each fetus had 3 datasets collected at 1.5T that were compared with the corresponding datasets acquired at 3.0T.

3.2.2a Signal to noise ratio (SNR): Quantitative comparison of image quality was performed by computing the SNR of the fetal brain. For a given fetus, SNR measurements were computed for each T2 dataset. For all cases, SNR was measured by defining a region of interest (ROI) within the white matter, and the mean signal was measured from this ROI. The noise was estimated by measuring the signal standard deviation (SD) from a homogenous white matter region within the ROI. SNR was then defined as a ratio of the mean value of the signal from the ROI and SD measured from the homogeneous signal region. For a given dataset, a central slice within the multislice data was first chosen, such that both cerebral hemispheres were clearly visualized. Next, the mean and SD values from two ROIs (one from each cerebral hemisphere) were obtained and then averaged to minimize the bias due to coil drop-off or non-uniform excitation.[115, 117, 130, 131] Compared to the 1.5T scan, higher resolution data were acquired at 3.0T with a corresponding higher pixel bandwidth. Therefore, the SNR measures were normalized to a fixed voxel volume of 1 mm^3 and a fixed pixel bandwidth of 244 Hz/pixel, so that a direct comparison could be made between SNR measures of the 1.5T and 3.0T data. Finally, SNR measures from the three T2 data acquisitions were averaged to obtain a single SNR measure for each fetus at a given field strength.

3.2.2b Specific absorption rate (SAR): Whole body SAR values, as estimated by the MR system console, were noted from the DICOM [132] (Digital Imaging and Communications in Medicine) image header. For a given patient, SAR values from the three separate views were noted and averaged to obtain a single SAR measure for each patient at a given field strength. It is noteworthy that whole body SAR values are calculated based on maternal physical parameters, which are also the criteria used to assess safety in rf dosimetry studies for fetal imaging. [133-135]

3.2.2c Diagnostic image quality and scoring system: Diagnostic image quality was assessed in a blinded fashion for all 1.5T and 3.0T MR images by a senior pediatric neuroradiologist (SM) with more than 10 years of experience with fetal MRI. The following nominal scoring scheme was used: 1) Score 1:

images of diagnostic quality without any artifacts; 2) Score 2: images of diagnostic quality, but with minor artifacts or low SNR; and 3) Score 3: images of non-diagnostic quality. Three datasets were evaluated for each fetus, and the best score was used to represent the overall data quality for that fetus respective to the field strength of the image.

3.2.2d Comparison of tissue contrast and conspicuity between 1.5T and 3.0T MRI: High soft tissue contrast occurs when different tissues are reflected by different intensity levels in the images. [64] Conspicuity is the property of being clearly discernible. [136, 137] Both tissue contrast and conspicuity of anatomical structures in the fetal brain were compared in a blinded fashion between 1.5T and 3.0T MRI by a senior pediatric neuroradiologist (SM) with more than 10 years of experience with fetal MRI. Specifically, tissue contrast for the fetal cortex, basal ganglia, dentate nucleus, and germinal matrix were evaluated due to their inherent discernibility. Conspicuity was evaluated for the fetal optic chiasm, basilar artery and vein of Galen due to their small size. Assessment was performed using the following nominal scoring scheme (performance of 3.0T relative to 1.5T): 1) Score 0: inferior; 2) Score 1: same as 1.5T data; 3) Score 2: superior; and 4) NA: not applicable (some structures cannot be visualized due to either early gestational age or pathology). After reviewing all T2 data acquired in different orientations at a given field strength, a single score was assigned (one for tissue contrast and one for conspicuity) for a given fetus.

3.2.2e. Statistical Analysis: Normality was assessed using the Kolmogorov-Smirnov test and visual plot inspection. Differences in distributions of normalized SNR and SAR were tested using either the paired t-test or its non-parametric equivalent, the Wilcoxon signed rank test, as appropriate. A 5% threshold was used in determining statistical significance. All analyses were performed using SAS version 9.3 (Cary, N.C.).

3.3 RESULTS

Twelve pregnant women prospectively underwent both a 1.5T and 3.0T fetal MR examination. Patients were referred for MRI examination due to the presence of fetal congenital anomalies, which included: Dandy-Walker malformation (n = 2), mild cerebral ventriculomegaly, hydrocephalus, mega

cisterna magna, myelomeningocele, hypoplastic left heart syndrome, distended small bowel loops, congenital heart disease including left heart syndrome, diaphragmatic hernia, cytomegalovirus infection, and monochorionic/diamniotic twins (with one viable fetus). The median (range) age of mothers was 24 (19-34) years. The median (IQR) gestational age at the time of 3.0T scan was 31.4 (27-34.2) weeks, and the median (IQR) time interval between the 1.5T and 3.0T scans was 2.5 (0.75 -5.25) days. All but three women were imaged within 3 days of the 1.5T scan; these women underwent a 3.0T MRI at 12, 19, and 20 days after the first scan.

3.3a SNR and SAR: Placement of the ROI on the T2 datasets for SNR measurements are shown in Figure 1. For all cases, normalized SNR and SAR measurements for fetal images obtained at 1.5T and 3.0T are depicted in Table 3.2. The SNR per unit voxel volume of 1 mm^3 (arbitrary units, a.u.) was significantly higher for images obtained using 3.0T than those obtained at 1.5T [median (IQR):4 (3.1-5.6) vs. 3.35 (2.5-3.65), respectively; $p = 0.03$]. Conversely, the whole body SAR value was significantly lower for images obtained at 3.0T than those obtained at 1.5T (mean ± SD: 0.6 ± 0.12 vs. 1.6 ± 0.2 Watt/kg, respectively; $p < 0.0001$) (Figure 3.2). Even when excluding the three subjects with more than 3 days between the 1.5T and 3.0T scans, such differences remained significant (SNR; $p = 0.03$ and SAR; $p < 0.0001$).

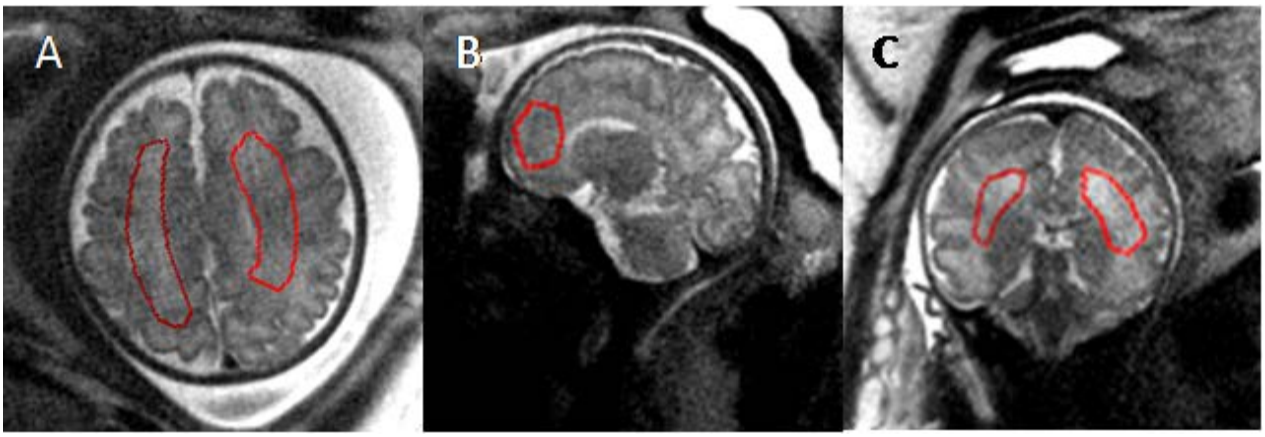

Figure 3.1: Placement of the ROI on T2 MRI datasets. ROIs were drawn on data acquired in three orientations for SNR measurements. Gestational age (weeks) A: 34 1/7; B: 34 4/7; C: 22 3/7. Images shown were acquired at 3.0T field strength

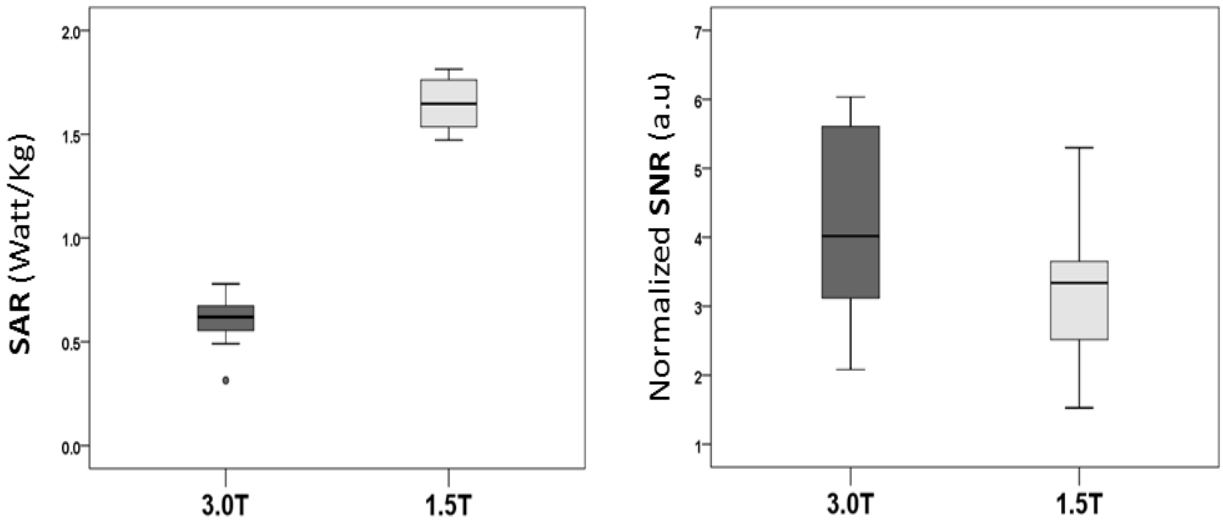

Figure 3.2: Comparison of normalized SAR and SNR values between T2 weighted single shot fast spin echo (SSFSE) sequence data obtained at 1.5T and 3.0T fetal MRI field strengths. (a.u., arbitrary units)

	1.5T		**3.0T**	
Subject #	**SNR (a.u.)**	**SAR (Watt/kg)**	**SNR (a.u.)**	**SAR (Watt/kg)**
1	3.2	1.1	5.5	0.6
2	3.4	1.8	2.1	0.3
3	2.0	1.8	3.1	0.7
4	1.5	1.8	3.7	0.5
5	3.4	1.5	5.3	0.7
6	3.4	1.7	5.8	0.5
7	5.3	1.7	5.7	0.6
8	2.3	1.7	4.3	0.7
9	2.7	1.5	3.6	0.6
10	3.9	1.5	2.9	0.7
11	3.3	1.5	3.1	0.8
12	3.9	1.5	6.0	0.6
Mean (SD)		1.6* (0.2)		0.6* (0.1)
Median (IQR)	3.35† (0.9)		4† (2.4)	

*P-value < 0.0001; †P-value = 0.03

Table 3.2: Comparison of normalized signal to noise ratio (SNR, arbitrary units) per unit voxel volume of 1 mm^3 and specific absorption rate (SAR, Watt/Kg) between T2 weighted single shot fast spin echo sequence data (n=12 subjects) obtained at 1.5T and 3.0T fetal MRI field strengths.

3.3b Diagnostic Image Quality: Anatomical data sets in different orientations were acquired from all fetuses at both field strengths. The best score was used to represent the overall data quality for a specific fetus. Scores assigned for diagnostic image quality are shown in Table 3.3. All cases at both field strengths were scored as having diagnostic quality present (Score of 1 or 2). Thus, there was no case which received a Score of 3 (non-diagnostic quality). Of all the cases, 83.3% (10/12) demonstrated equal diagnostic quality between both field strengths: 1) 75% (9/12) received a Score of 1 at both 1.5T and 3.0T (indicating diagnostic image quality without any artifacts), and 2) 8.3% (1/12) received a Score of 2 at both 1.5T and 3.0T (indicating diagnostic image quality, but with minor artifacts or low SNR). In 16.7% (2/12) cases, images from 3.0T received a Score of 2, while the corresponding images from 1.5T received a Score of 1. Nevertheless, for a given fetus, data from at least one anatomical orientation had diagnostic quality present at both imaging field strengths.

3.3c Tissue Contrast: Tissue contrast was evaluated and compared between field strengths for four anatomical structures in the fetal brain: cortex, basal ganglia, dentate nucleus and germinal matrix (Table 3.4). While the cortex could be visualized and evaluated in all 12 fetuses, the basal ganglia, and dentate nucleus were each visualized and evaluated in 11 fetuses, and the germinal matrix in 3 fetuses. Some anatomical structures were not visualized due to either early gestational age or the pathologic abnormality and were scored as NA (not applicable). Thus, a total of 37 scores were assigned. Images of the cortex, basal ganglia, dentate nucleus, and germinal matrix obtained from 3.0T were equal (57%; 21/37), or superior (35%; 13/37) to that of 1.5T for tissue contrast. In 8% (3/37), tissue contrast of the dentate nucleus was inferior on 3.0T (vs. 1.5T) MRI.

Diagnostic Image Quality Score		
Subject #	**3.0T**	**1.5T**
1	2	1
2	2	1
3	1	1
4	1	1
5	1	1
6	1	1
7	1	1
8	1	1
9	1	1
10	2	2
11	1	1
12	1	1

Score 1: images of diagnostic quality without any artifacts
Score 2: images of diagnostic quality, but with minor artifacts or low SNR
Score 3: images of non-diagnostic quality

Table 3.3: Scores assigned for diagnostic image quality for fetal images obtained at 1.5T and 3.0T MRI. The best score was used to represent the overall data quality for a specific fetus.

3.3d Conspicuity: Conspicuity was evaluated and compared between field strengths for three fetal anatomical brain structures: optic chiasm, basilar artery, and vein of Galen (Table 4.4). In one fetus, these structures could not be visualized due to early gestational age. Thus a total of 33 scores were assigned. Images of the optic chiasm, basilar artery, and vein of Galen obtained from 3.0T were equal (61%; 20/33) or superior (33%; 11/33) to that of 1.5T for conspicuity. In 6% (2/33), conspicuity of the optic chiasm and basilar artery was inferior on 3.0T (vs. 1.5T) MRI. Comparisons between MR images of the fetal brain obtained at 1.5T and 3.0T field strengths are shown in Figures 3.3 through 3.5. Figure 3.3 compares images from a 26-week fetus that was scanned on the same day at both field strengths. Figure 3.4 depicts 1.5T

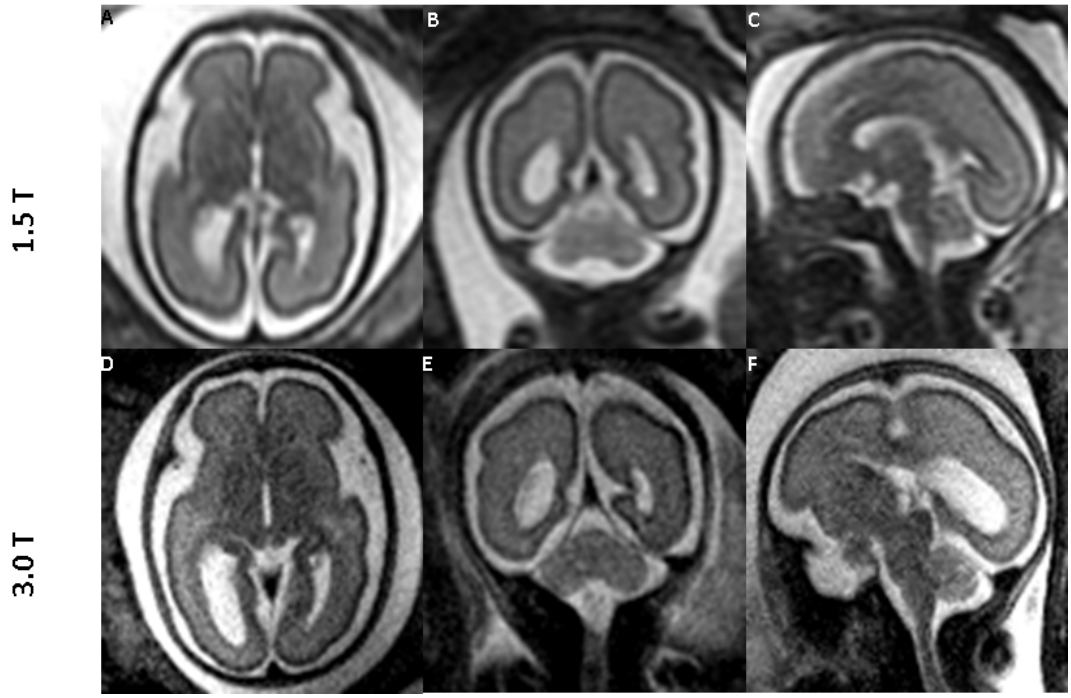

Figure 3.3: Comparing images of the fetal brain at 26 weeks of gestation obtained at 1.5T and 3.0T MRI (same fetus): 1.5T (top row, A-C) and 3.0T (bottom row, D-F) in all three orientations: Axial (A,D); Sagittal (B,E); and Coronal (C,F). Both 1.5T and 3.0T scans were performed on the same day. The images from 3.0T show superior tissue contrast and conspicuity to that of 1.5T.

images of the fetal brain and the corresponding 3.0T images of three different fetuses at varying gestational ages. Figure 3.5 compares the conspicuity and contrast of the germinal matrix, optic nerve, and basilar artery, as well as the migrational pattern seen between 1.5T vs. 3.0T MRI. Superior tissue contrast and conspicuity were observed in the 3.0T images.

3.4 DISCUSSION:

The principal findings of this study are: 1) SNR was significantly higher for images obtained using 3.0T than those obtained at 1.5T; 2) the average whole body SAR value was significantly lower for images obtained at 3.0T than those obtained at 1.5T; 3) all cases at both field strengths were scored as having diagnostic quality present, and 83.3% of cases demonstrated equal diagnostic quality between both

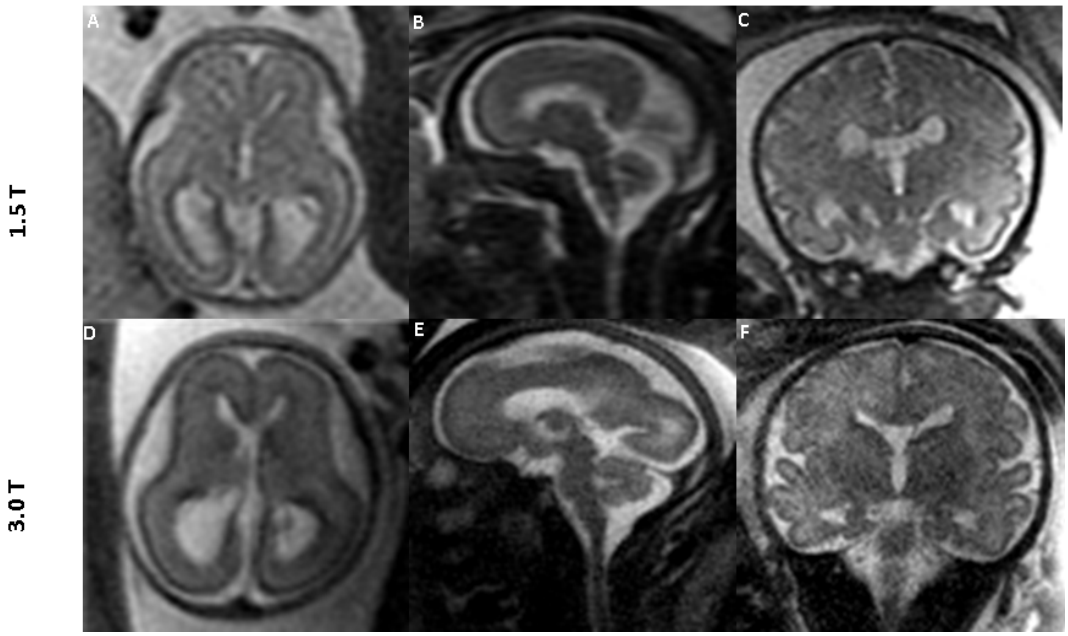

Figure 3.4: 1.5T MR images of the fetal brain (top row) and the corresponding 3.0T images (bottom row) across different gestational ages. Data were obtained from 3 different fetuses. Images in the top row and the corresponding images in the bottom row are from the same fetus. Gestational age (weeks) at the time of scan were: (A: 22, D: 22 3/7); (B: 27, E: 27 2/7); and (C and F: 35 1/7). Superior tissue contrast and conspicuity are demonstrated in the 3.0T images.

field strengths; 4) images from 3.0T MRI (compared to 1.5T) were equal (57%) or superior (35%) for tissue contrast; and 5) images from 3.0T MRI (compared to 1.5T) were equal (61%) or superior (33%) for conspicuity of anatomical structures. Such superior conspicuity could be attributed, in part, to higher resolution imaging with 3.0T MRI, and changes in the tissue relaxation times between 1.5 and 3.0T. The smaller voxel size allowed for clearer visualization of certain anatomical structures (e.g. optic nerve) (Figure 3.5) and thus, improved conspicuity. Tissue T2 relaxation values are known to decrease with increasing field strength. [138-140] Due to the use of almost equivalent echo times between both field strengths, this effectively led to an increased T2 weighting at 3.0T compared to 1.5T, which may have contributed to the improved tissue contrast and conspicuity.

	Tissue contrast					Conspicuity		
	Cortex	**Basal Ganglia**	**Dentate Nucleus**	**Germinal Matrix**		**Optic Chiasm**	**Basilar Artery**	**Vein of Galen**
Inferior (Score 0)	0	0	3	0		1	1	0
Equal (Score 1)	6	7	5	3		6	7	7
Superior (Score 2)	6	4	3	0		4	3	4
NA	0	1	1	9		1	1	1

Table 3.4: Comparison of tissue contrast and conspicuity for anatomical structures in the fetal brain between 1.5T and 3.0T MRI data. Images are scored with regards to how 3.0T compares to 1.5T MRI (reference).

Signal to noise ratio (SNR) in MR imaging is roughly linearly proportional to the imaging field strength and is one of the main incentives for moving to fetal imaging at 3.0T. Practically, the factor 2 gain in SNR is not always seen at 3.0T due to various factors, such as rf inhomogeneity (excitation and reception) and field appropriate sequence modifications performed for optimizing image quality. In the study herein, additional sequence modifications were employed for SAR reduction. Yet, despite this, we observed a significantly higher SNR at 3.0T than at 1.5T. The higher SNR allowed for higher resolution acquisition at 3.0T (compared to 1.5T), which improved the definition of smaller anatomical structures, such as the optic chiasm.

SAR is a crucial factor to consider when imaging the fetus at 3.0T. Importantly, when imaging the fetal brain at 3.0T, there were lower SAR values (despite better SNR) compared to that of 1.5T (by almost a factor of 2). The SAR values compared in the current study are average whole body SAR values as calculated by the MRI scanner, which assumes certain standard adult imaging conditions. [141] SAR is also dependent on multiple factors, such as body shape, surface area, composition, and spatial location within the scanner. Recent rf dosimetry studies of pregnant human models report that, provided the

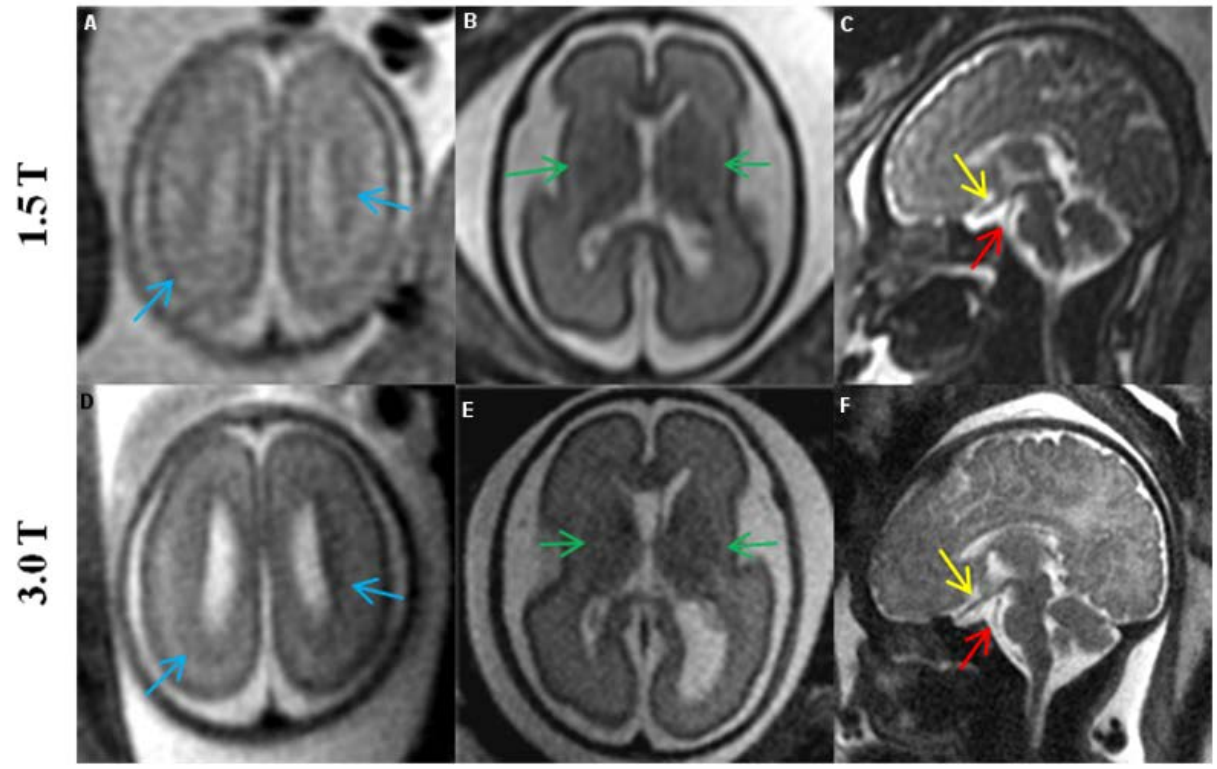

Figure 3.5: Comparison of 1.5T (top row) vs. corresponding 3.0T (bottom row) MR images of the fetal brain, showing the advantages of increased resolution at 3.0T. 1) Blue arrows (A, D) show the pattern of migration more clearly at 3.0T; 2) green arrows (B, E) show increased contrast in the germinal matrix; and 3) yellow and red arrows (C, F) show clear delineation of the optic nerve and basilar artery, respectively, at 3.0T. Images in the top row and the corresponding images in the bottom row are from the same fetus. Gestational age (weeks) at the time of scan were: (A: 22 , D: 22 3/7); (B and E: 26 1/7) ; (C: 35 1/7, F: 35 4/7).

scanner calculated maternal whole body SAR is < 2W/kg, the local fetal SAR values and tissue temperature increase at 3.0T field strength are well within the safety limits.[133-135] Moreover, the lower the maternal whole body average SAR, the lower is the rf energy deposition in the fetus. [133-135] The SAR parameter also has the following dependency on MR imaging parameters and patient weight: [119, 120, 141, 142]

$$SAR \alpha (\theta)^2 (B_0)^2 * (1/TR) * (1/\tau_{rf}) * (1/W) \quad (3.1)$$

where θ is the rf pulse flip angle of the imaging sequence, τ_{rf} is the rf pulse duration, TR is the repetition time of the MR imaging sequence, and W is the weight of the patient. Therefore, SAR is directly proportional to the imaging flip angle, and inversely proportional to the rf pulse duration and the TR of the sequence. In this study, a HASTE sequence with hyperecho option was used for imaging at 3.0T. [127, 143-145] Along with the use of lower flip angle pulses of 75^{o}, this hyperecho option helped to reduce rf energy deposition. [127, 143-145] In addition, rf pulses with a longer pulse duration (using the 'low SAR' option on the scanner) and a longer TR were used for the HASTE sequence at 3.0T. All of these factors contributed towards significantly lowering SAR values at 3.0T compared to 1.5T. The SAR values at 3.0T reported herein are also lower than those reported by Victoria et al in a recent review paper. [109] Indeed, in the study herein, the maximum SAR for the HASTE sequence at 3.0T field strength was 25% less than the 2 W/Kg limit corresponding to the 'normal' operating mode of clinical MRI scanners. [146, 147] While the lower nominal excitation flip angle does affect the SNR to some extent, this did not significantly reduce the quality of the images at 3.0T, which is evident from the diagnostic image quality scores.

The image quality is also dependent on the sequence parameters in addition to the field strength, the SNR relationship can be given by the following equation:

$$\text{SNR} \propto \frac{\omega_0 * \Delta x * \Delta y * \Delta z * \sqrt{N_{avg}} * Sin^3\,\theta * \frac{TR}{T1}}{\sqrt{\frac{BW}{N_x * N_y * N_z}}}$$

Where ω_0 has the field strength dependence, $\Delta x, \Delta y, \Delta z$ are the image resolution, BW – bandwidth, TR, T1 and θ are as described earlier. The proportionality relation with flip angle and TR/T1 is assuming that the sequence is a simple spin echo sequence, however practically the relationship would be different as the sequence used here was a HASTE with hyper echo and a single-shot FSE. For the sequence parameters used in our scans and assuming that the T1 at 3.0T is about 40% greater than the T1 of fetal brain at 1.5T (based on adult abdominal tissue). The SNR at 3.0T should be approximately about 0.9 times the SNR at 1.5T. ($SNR_{3.0T} = 0.92*SNR_{1.5T}$). As expected the images of 3.0T scans in figure 3.5 is

nosier compared to the 1.5T scans. The plot in figure 3.2 shows the normalized SNR per unit volume as a given BW. However the true image SNR was measured was $SNR_{3.0T} = 0.78*SNR_{1.5T}$. The aim of the study was to compare the image quality. This was done qualitatively based on the scoring by a radiologist. We also wanted to quantitatively measure an image metric that is representative of the image quality. Hence we measured the SNR from both hemispheres and in 2D slices that was acquired in all three orientations relative to the fetal brain. While the average of all these local SNRs does not represent the true SNR, we believe that it would be an equivalent representation demonstrating the image quality. A true quantitative comparison between the two field strengths is very challenging due to: (1) the use of different coils, a phased array 6-channel cardiac coil at 1.5T versus a 4-channel body flex coil at 3.0T; (2) differences in the position of the mother with respect to the coil; (3) differences in the position of the fetus within the mother and also with respect to the coil; (4) the position of the coil within the axis of the magnet; and (5) the use of hyper-echo and half Fourier acquisition at 3.0T.

Some limitations of this work include the small sample size and variation in the time duration between 1.5T and 3.0T studies. However, even when excluding the three subjects with more than 3 days between the 1.5T and 3.0T scans, the differences in SNR and SAR between field strengths remained significant and did not alter our findings.

MR imaging at 3.0T offers tremendous advantages in terms of SNR and improved spectral separation in MRS. This could allow the use of faster and more sensitive advanced sequences to image the human fetus (e.g. brain) at 3.0T, such as susceptibility weighted imaging, diffusion-weighted imaging, and magnetic resonance spectroscopy, all of which are typically low in SAR. [148]

3.5 CONCLUSION:

This is the first study in the human fetus to systematically compare SNR, SAR and image quality between 1.5T and 3.0T MRI. With appropriate sequence adaptations, examining the fetal brain using 3.0T MRI results in higher image resolution and SNR, with simultaneously lower radio frequency energy deposition than that of 1.5T. Moreover, 3.0T images demonstrate superior tissue contrast and conspicuity than images obtained using 1.5T MRI in approximately one-thirds of cases.

CHAPTER 4: QUANTITATIVE FLOW IMAGING IN THE HUMAN UMBILICAL VESSELS

This chapter shows the feasibility of performing quantitative average blood flow measurements in the fetal vessels using phase contrast MR imaging without the necessity of a triggering signal. Numerical simulations suggest that the error is within permissible limits. We show one of the first applications of simple non-triggered quantitative phase contrast imaging in human fetal imaging for measuring flow in the umbilical vessels that does not require any major sequence modification and/or complex post-processing methods.

4.1 INTRODUCTION:

The growth and development of the human fetus are supported through an effective maternofetal circulation. Assessment of fetoplacental hemodynamics using measures like pulsatility index (PI), resistance index (RI), peak velocities during diastole or systole (S/D ratio), presence or absence of the notch in the flow waveforms, etc., is performed routinely during clinical assessment of pregnancy [149, 150]. Indeed, in cases of severe intra-uterine growth restriction (IUGR) and moderate fetal growth restriction (FGR) conditions, umbilical artery PI/waveform is found to be a useful indicator of fetal distress and predictor of postnatal outcome [151, 152]. While these indices characterize important hemodynamics, additional volumetric blood flow rate measurements could help in estimating important physiologic parameters like bulk organ perfusion. Doppler ultrasound (US) may be used for such measurements. However, the accuracy and repeatability of Doppler based volumetric flow measurements in fetal vessels are affected by factors like insonation angle and the absence of accounting for the spatial velocity profile [153]. Furthermore, in situations, where the vessels are located in close proximity to echogenic tissue like bone, or cases of oligohydramnios, could preclude flow measurement entirely. Magnetic resonance imaging (MRI), on the other hand, is a great adjunct to US in fetal diagnostic imaging [154, 155] and offers quantitative imaging capability with large fields-of-view at high resolutions that is relatively operator independent. Furthermore, phase contrast magnetic resonance imaging (PCMRI), is one of the most accurate methods for measuring in-vivo blood flow rates and is routinely

used clinically in neonates, in pediatric and adult subjects for blood or cerebrospinal fluid flow quantification. Measuring blood flow rates in fetoplacental vessels using MRI makes quantitative hemodynamic studies like evaluating bulk organ perfusion or evaluation of oxygen delivery and/or consumption rates possible in-utero. Such approaches are increasingly becoming important in the study of the great obstetric syndromes.

Studies applying PCMRI for evaluating fetal and/or placental blood flow, however, are scant [156-158], primarily due to a) the lack of physiologic gating signal (fetal echocardiography or fetal pulse monitor) within the MRI system that facilitates synchronization of data acquisition for time-resolved flow quantification; and b) fetal motion. Specifically, the latter aspect necessitates fast imaging methods that minimize chances of data corruption from fetal motion. Today both data-driven self-gating [157], and use of MR safe fetal cardiotocography equipment are active areas of research [159, 160]. However, application of these methods requires either complex reconstruction algorithms or custom hardware. Furthermore, due to their long acquisition times, these techniques are prone to bulk fetal motion which precludes any useful measurement. Alternatively, non-gated phase contrast MRI (ng-PCMRI) is a fast method that can map time-averaged velocity in a spatially resolved manner, without the necessity of any gating signal [161]. In this work, we study the applicability of 2D ng-PCMRI technique for blood flow measurements in umbilical blood vessels in human fetuses. We first validated the flow measurements in the major arteries in the adult neck. And, after studying the expected errors in flow assessment for typical umbilical arterial flow conditions through simulations, ng-PCMRI was applied to measure blood flow rates in human umbilical vessels in normal pregnant subjects in second and third trimesters.

4.2 MATERIALS AND METHODS:

4.2.1 Non-gated phase contrast MRI (ng-PCMRI): The conventional 2D time-resolved PC imaging sequence with Cartesian data sampling was modified to phase encode without any gating and with the bipolar velocity encoding with positive and negative polarity occurring in consecutive repeat-times (TR_i and TR_{i+1}), as shown in Figure 4.1. Flow encoding is applied along the slice direction and two images are obtained as the output of the sequence - one with positive and the other with negative bipolar velocity

encoding. The final PCMRI image is obtained by complex dividing the positive and negative velocity encoding d

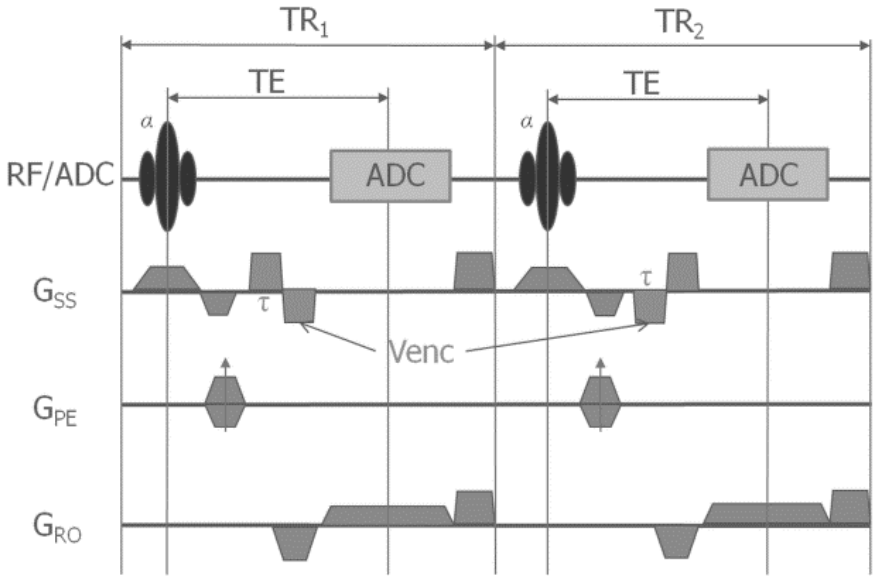

Figure 4.1: Sequence diagram of the non-gated phase contrast MRI (ng-PCMRI) showing the continuous acquisition without the need for any physiological trigger. RF – radio frequency excitation pulse; ADC – analog to digital converter; Venc –velocity encoding gradients; Gss- slice select gradient; G_{PE}- phase encoding gradient; G_{RO}- readout gradient.

4.2.2 Validation in normal adult volunteers: Flow measurements from ng-PCMRI were compared with that obtained from the conventional pulse gated PCMRI (pg-PCMRI) technique. Six healthy adult subjects (5 male, 1 female, median age: 27.5 years, IQR 7.5 years) were imaged after obtaining an informed consent, in accordance with the local institutional review board (IRB) guidelines. The conventional pg-PCMRI sequence and the ng-PCMRI sequences were applied in an interleaved manner for measuring flow in the common carotid arteries at the C6/C7 level of the cervical spine. Imaging was performed on a 3.0T Siemens Verio system (Erlangen, Germany). Measurements were carried out under free-breathing conditions and repeated 5 times in each subject. The imaging protocol consisted of the anatomical localizer followed by an MRA sequence for localization of the carotid vessels to guide placement of the PCMRI acquisitions. This was followed by the conventional pg-PCMRI and the ng-PCMRI acquisitions, applied at the same anatomical location, perpendicular to the common carotid

arteries. Imaging parameters for the conventional pg-PCMRI were: repeat time (TR) = 54ms, echo time (TE) = 3.98, Venc = 50cm/s, bandwidth = 243Hz/pixel, field-of-view (FOV) = 295mm, resolution = 0.67x0.67x4mm^3, flip angle = 15^0,and a total acquisition time of 58sec with 30 cardiac time-points. The ng-PCMRI sequence was acquired with the same voxel size and venc as that of the conventional PCMRI with the following imaging parameters: TR = 14ms, TE = 6.9ms, flip angle =15^0, bandwidth = 248Hz/pixel, number of averages = 6, total acquisition time = 75 sec. Blood flow rates in the left and right common carotid and vertebral arteries were assessed by two independent observers by drawing a manual freehand region of interest (ROI). The resolution ensured that the vessel lumen (area) occupied at least 30 voxels. Agreement between the conventional gated (pg-PCMRI) and non-gated (ng-PCMRI) measurement methods was statistically evaluated using the Pearson's correlation (*r*). Inter-observer agreement between the two independent observers was assessed using intraclass correlation (ICC). A p value less than 0.05 was considered statistically significant.

4.2.3 Numerical simulations for umbilical flow measurement: In ng-PCMRI, phase-encoding occurs over different cardiac phases, providing an average velocity measure in the final image. In the case of pulsatile flow, vessel phase varies from view-to-view (i.e., phase encode to phase encode). This could introduce a bias in the average velocity measured, depending on the relative position of the phase-encode order and the pulsatile velocity-time curve. Averaging over multiple measurements can reduce such variability [162].

To understand the nature and extent of such errors for a typical velocity-time profile of blood flow observed in the umbilical vessels, we performed numerical simulations using a 2D digital flow phantom. For steady flow conditions without any pulsatility, as in the umbilical vein, ng-PCMRI does not lead to any systematic quantification error [162]. Hence, velocity-time profile of umbilical arteries, which have pulsatile flow, was considered in these simulations. Two sets of simulations were carried out to assess the degree of error in flow due to 1) the typical variability in fetal heart rate and the pulsatility in the flow during data acquisition [163]; and 2) due to partial voluming. A laminar spatial flow profile was considered [164] (Eq. 4.1). Anonymized umbilical artery blood flow velocity waveform from a normal

fetus in the third trimester was obtained from the local obstetrical care as measured using Doppler US. Using this waveform, a fetal blood flow velocity curve was generated for the entire duration of a simulated ng-PCMRI acquisition (Figure 4.2), with a velocity value available for each TR of the acquisition. In generating this waveform, for multiple repeated simulations (see N_{sim} parameter below) typical fetal heart rate variability and amplitude variation in the flow were considered. Gaussian variability in the fetal cardiac period was introduced with a mean value 445msec and a standard deviation 50msec. Similarly, the peak amplitude of the velocity-time curve was also varied – mean peak value of ~45 cm/sec and a standard deviation of 4.5 cm/sec (10%). Figure 2 illustrates one instance of the velocity-time curve generated for digital simulation of ng-PCMRI.

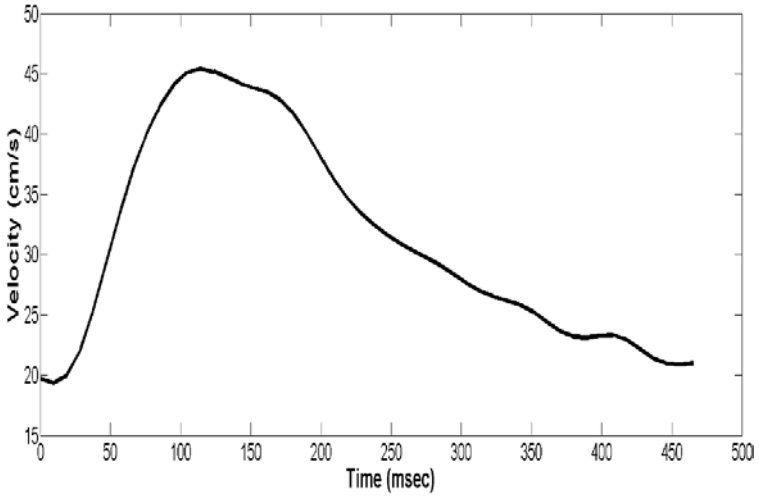

Figure 4.2: Instantaneous velocity-time curve created for one time instance from the nominal velocity and using a random 10% variation in amplitude and a random 50ms variation in the cardiac cycle.

The digital flow phantom consisted of two concentric cylinders, set up within a 256x256 matrix. The inner cylinder, which represented the vessel (radius 16 pixels), was embedded in a larger outer cylinder (radius 103 pixels) simulating the background tissue. An arbitrary amplitude of 100 and 25 units was assigned to the vessel and background respectively which defined the magnitude M(x,y). A laminar flow profile within the vessel lumen was simulated using the equation:

$$v(x) = V_{max}\left(1 - \frac{r}{R}\right)^2 \tag{4.1}$$

where, r is the radial distance of a point in the vessel from its center and R is the radius of the vessel.

Similar to the actual data acquisition procedure in MR, velocities corresponding to each pair of consecutive TRs, were taken and assigned to the vessel to generate the positive and negative bipolar phase-encode lines. The following equations summarise this process.

$$p(k_{pe,j}) = FT\left[M(x,y) \cdot e^{i\varphi_{p,vessel}(r,t)}\right]_j \tag{4.2}$$

$$n(k_{pe,j}) = FT\left[M(x,y) \cdot e^{i\varphi_{n,vessel}(r,t)}\right]_j \tag{4.3}$$

$$\varphi_{p,vessel}(r,t) = \begin{cases} \left(\pi \cdot \frac{v(r,t)}{V_{enc}}\right) & -Inside\ the\ vessel \\ 0 - In\ the\ background\ tissue \end{cases} \tag{4.4}$$

$$\varphi_{n,vessel}(r,t) = \begin{cases} -\left(\pi \cdot \frac{v(r,t)}{V_{enc}}\right) & -Inside\ the\ vessel \\ 0 - In\ the\ background\ tissue \end{cases} \tag{4.5}$$

Here, $p(k_{pe,j})$ and $n(k_{pe,j})$ are the k-space corresponding to the positive and negative bipolar velocity encoding; j indicates the j^{th} phase encode line; $\varphi_{p,vessel}(r,t)$ and $\varphi_{n,vessel}(r,t)$ are the vessel phase corresponding to the positive and negative bipolar lobe encoding. V_{enc} is the velocity that corresponds to a phase of π in the vessel. Gaussian noise was added during the k-space generation such that the signal to noise ratio in the background tissue was 5:1. A venc value of 50cm/sec was used. The final positive and negative bipolar encoded images were then complex divided to obtain the velocity encoded ng-PCMRI image. Short term averaging (N_{avg} - number of averages) was simulated similarly, but with consecutive pairs of TRs now corresponding to the same phase encode step, for a duration = 2xTRxN_{avg}. The generated N_{avg} phase-encode lines for a given phase encode step were averaged (positive and negative encoding lines separately). The final ng-PCMRI image was generated by complex dividing the images corresponding to the positive and negative bipolar encodings according to equation.

$$I(x,y) = \frac{FT^{-1}[p(k)]}{FT^{-1}[n(k)]} \tag{4.6}$$

The simulations were carried out for averages, N_{avg}, ranging from 1 to 10 (step size = 1). The percent error in the velocity (or flow) measured from the vessel cross-section in ng-PCMRI with respect

to the corresponding theoretical average velocity, obtained from the input velocity-time curve was then evaluated. The simulation was repeated, N_{sim} = 300 times, wherein each instance a different (random) heart rate variability and amplitude variation were introduced in the umbilical velocity-time curve. For a given N_{avg}, the standard deviation of the percent error, over the N_{sim} values, represented the systematic error expected from ng-PCMRI in the umbilical artery flow.

Large voxel sizes relative to the vessel size leads to partial voluming and consequent errors in the measurement of velocity as well as vessel cross-sectional area. For assessing the influence of these factors in ng-PCMRI for pulsatile flow, a procedure similar to the one used by Jing et al. [164], was employed. Briefly, instead of starting with matrix size was 256x256, a larger matrix size was taken and condensed to the final matrix size of interest, by taking the central k-space region, to simulate partial voluming. Vessels of radii 2, 3, 4, 6 and 8 voxels in the final matrix size were simulated by starting with a vessel of size 32, 48, 64, 96 and 128 respectively in a matrix size of 4096x4096. Laminar flow profile as described earlier (equ. 1) was used and velocity and flow error in the final partial-volumed vessel were evaluated as a function of vessel diameter. Simulations were carried out for N_{avg} = 6 and N_{sim} = 20. In this assessment, the vessel cross-sectional area was measured from the outer rim of the vessel, as advised in Jing et al [164].

4.2.4 Fetal Imaging: Pregnant women who were receiving care at Hutzel Women's Hospital in Detroit, MI, USA, were non-consecutively recruited in this study. Pregnant women, with singleton pregnancies, between the age of 18 to 38 years and who were between 19 and 40 weeks gestation were approached for recruitment. The imaging study was approved by the local IRB and was compliant with HIPAA regulations. All subjects imaged in this study were recruited in accordance with local IRB guidelines and written informed consent was obtained from them prior to the MRI scan. All the subjects were considered normal pregnancies based on their routine US examinations.

Fetal MRI scans were performed using a 3.0T Siemens Verio system (Erlangen, Germany) with a 4 channel body flex array coil along with the spine coil. As part of a larger study, ng-PCMRI data was acquired whenever possible. The umbilical vessels were first localized using a non-contrast, non-breath

hold time-of-flight angiography sequence [165]. Once the umbilical cord was localized, non-gated phase contrast images using the modified sequence were acquired using the following parameters: TR = 14/30 msec, TE = 7-9 msec, slice thickness = 3/4 mm, voxel size between (0.5 – 0.8) x (0.5 – 0.8) mm^2 and flip angle = 15^o. The energy deposited, measured as the average whole body SAR, was consistently maintained below 0.5 W/kg. Within the limitations of time, acquisitions were repeated when fetal motion was encountered. The flow was quantified using an in-house software 'FlowQ' developed in Matlab [166], that allowed for drawing of a manual ROI. For inter-rater reliability the intraclass correlation (ICC) was used.

4.3 RESULTS:

4.3.1 Adult Human Volunteers: There was excellent agreement between the measurements made from the two methods (Figure 4.3). The Pearson's correlation coefficient (*r*) between the two methods was 0.96 with a $p < 10^{-5}$.The results remain unchanged even when independently analyzed by a different observer. The intraclass correlation coefficients were 0.91 ($p < 10^{-5}$) for conventional gated flow (pg-PCMRI) and 0.99 ($p < 10^{-5}$) for the ng-PCMRI. There is clearly a trend to underestimate the total flow when using the ng-PCMRI.

4.3.2 Numerical Simulations: Figure 4.4 shows the mean percent error in the measured velocity and the corresponding standard deviation over N_{sim}=300, as a function of N_{avg}. While the error itself is small, the variance in this error also decreases with increasing N_{avg}. Even averaging over two acquisitions brings down the variance from 10% to 3%, which is a 30% increase in the confidence of our measurement. From these results, N_{avg} = 6, which corresponded to a mean error of 0.22% ± 1.5% was chosen as the reasonable trade-off point between total imaging time and variance in the measurement.

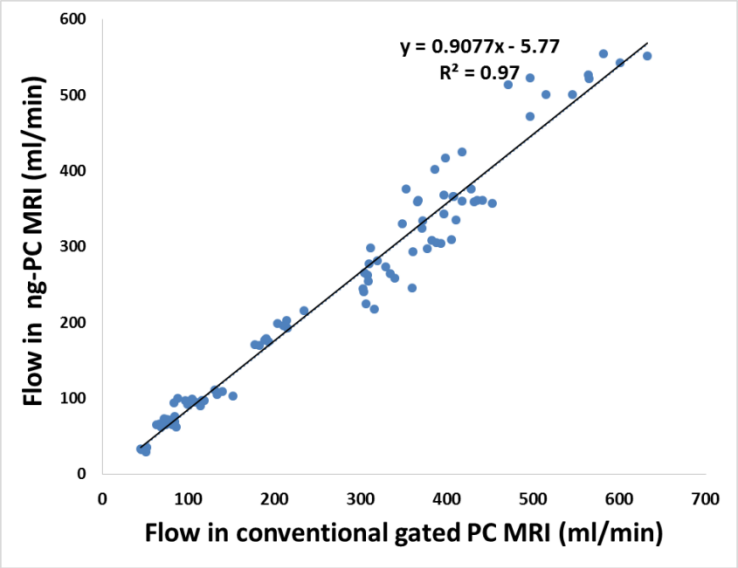

Figure 4.3: Plot of the average flow in the major arterial vessels of the adult neck measured using conventional gated PCMRI and ng-PCMRI.

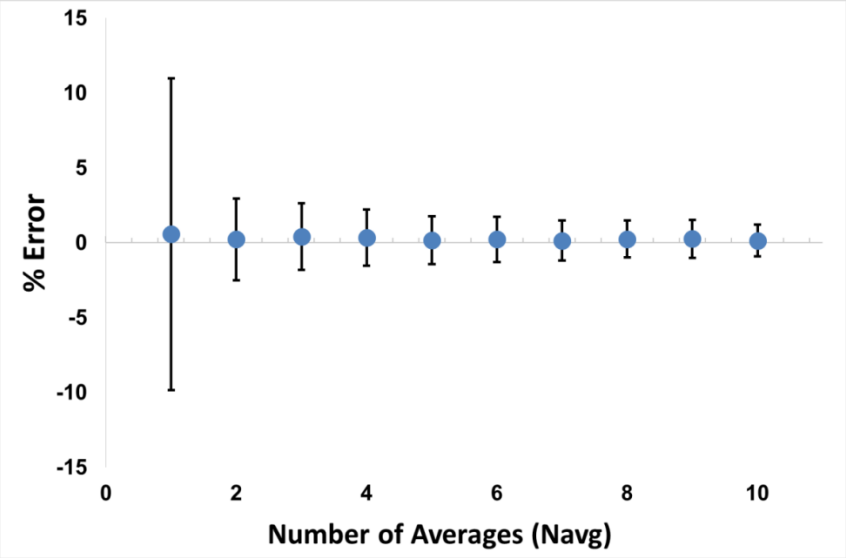

Figure 4.4: Plot of the errors in the measured velocity as a function of averages. Data was simulated using a nominal umbilical artery waveform incorporating beat-to-beat variations in amplitude and duration of the cardiac cycle

Figure 4.5 plots the percent error in the measured velocity and flow for vessels ranging from radius 2 to radius 8 voxels for N_{avg} = 6 and N_{sim} = 20. As expected the measurement error in both velocity and flow reduces as the vessel size (in voxels) increases. The velocity and flow were measured using an automatic intensity based threshold, which caused an underestimation of the lumen area and an over-estimation of the velocity (as it measured on the upper segments of the parabolic laminar profile), hence the negative error in the velocity. However, the flow error is significantly lower than the error in velocity.

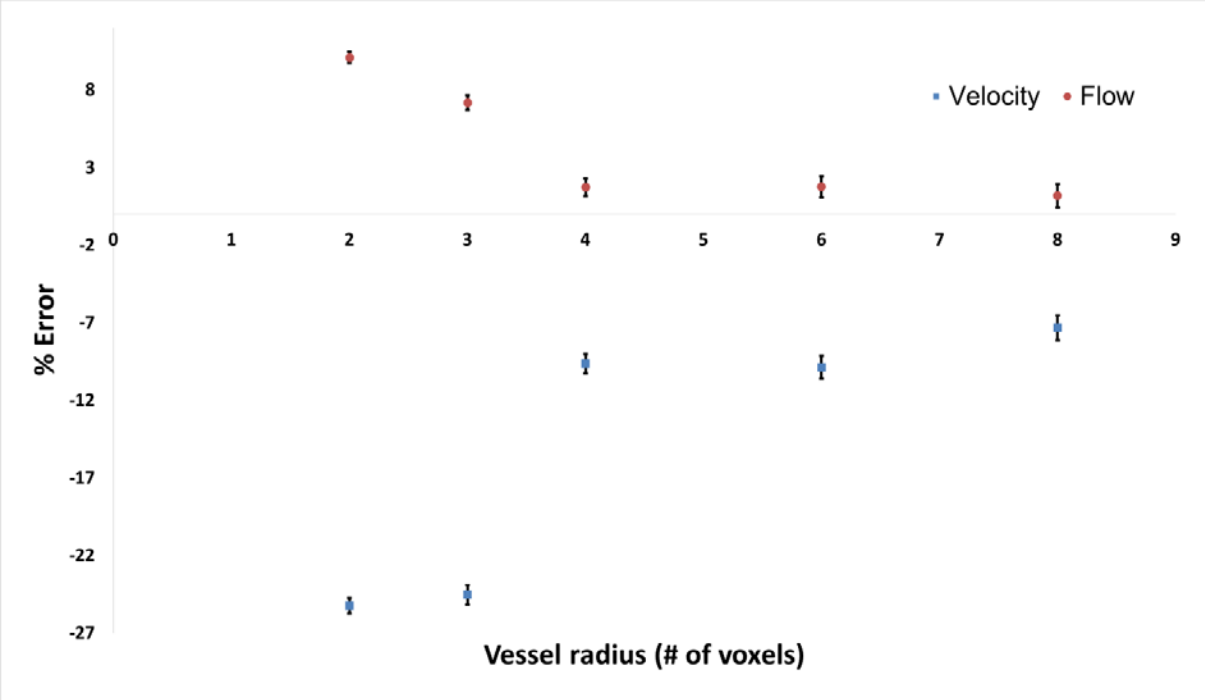

Figure 4.5: Plot of the errors in the measured velocity and flow as a function of vessel diameter in voxels. While velocity error is larger than flow error, both errors decrease as vessel size increases. Data was simulated using a nominal umbilical artery waveform incorporating beat to beat variations in amplitude and duration of the cardiac cycle. N_{sim} = 20, N_{avg} = 6.

These observations are in good agreement with previous findings done for pg-PCMRI[164]. For a vessel radius of 2 voxels, the error in flow was measured to be 10% ± 0.4% and at radius 3 voxels, 7.2% ± 0.5%. These results provided an estimate of the error to be expected in flow measurements from small vessels like umbilical arteries.

4.3.3 Fetal umbilical imaging: Fetal ng-PCMRI was acquired under the aegis of a larger study. Of these, 24 cases were included in this study. The median gestational age of the fetuses included in this study was 30 4/7 weeks and had an interquartile range of 8 1/7 weeks. The magnitude and phase images clearly show the umbilical vessels, the opposite flow in the arteries and veins is indicated by the opposite phase signature in the phase images (Figure 4.6). The combined average flow in the umbilical arteries was 203 ± 80 ml/min and in the corresponding flow in the umbilical vein was 232 ± 92 ml/min. Excellent inter-observer correlation coefficient (ICC) was found in non-gated umbilicus flow and velocity measurements: ICC-flow: (a) umbilical arteries *r*: 0.86 ($p < 10^{-6}$) and (b) umbilical vein *r*: 0.96 ($p < 10^{-10}$); ICC-velocity: (c) umbilical artery 1 *r*: 0.93 ($p < 10^{-10}$); umbilical artery 2 *r*: 0.79 ($p < 10^{-06}$); and (d) umbilical vein *r*: 0.97 ($p < 10^{-10}$). The flow in both the artery and the vein increased with increasing gestational age (Figure 7). When the arterial and venous flow measurements were plotted against each other, there was good correlation with a slope of 0.64. In all but one fetus (n=23), the estimated fetal weight was measured as part of their routine US scan that was done within a week prior to the MRI scan. The average flow normalized to the fetal weight was 140 ± 60 ml/kg per min and 158 ± 57 ml/kg per min in the umbilical artery and vein respectively.

4.4 DISCUSSION AND CONCLUSIONS:

We have presented preliminary results on the feasibility of measuring the umbilical blood flow using non-gated PCMRI. Using Monte-Carlo simulations, we assessed the systematic error for velocity and blood flow for representative data in umbilical vessels. While the basic idea of ng-PCMRI imaging for fast acquisition has been around for over two decades, its use has been confined to a few applications due to limited precision in high pulsatility flow conditions [161, 167]. While these previous works focused on the application of ng-PCMRI in major arteries in adults, this is the first study assessing its applicability in fetal vessels in-utero due to limited precision in high pulsatility flow conditions [161, 167]. While these previous works focused on the application of ng-PCMRI in major arteries in adults, this is the first study assessing its applicability in fetal vessels in-utero.

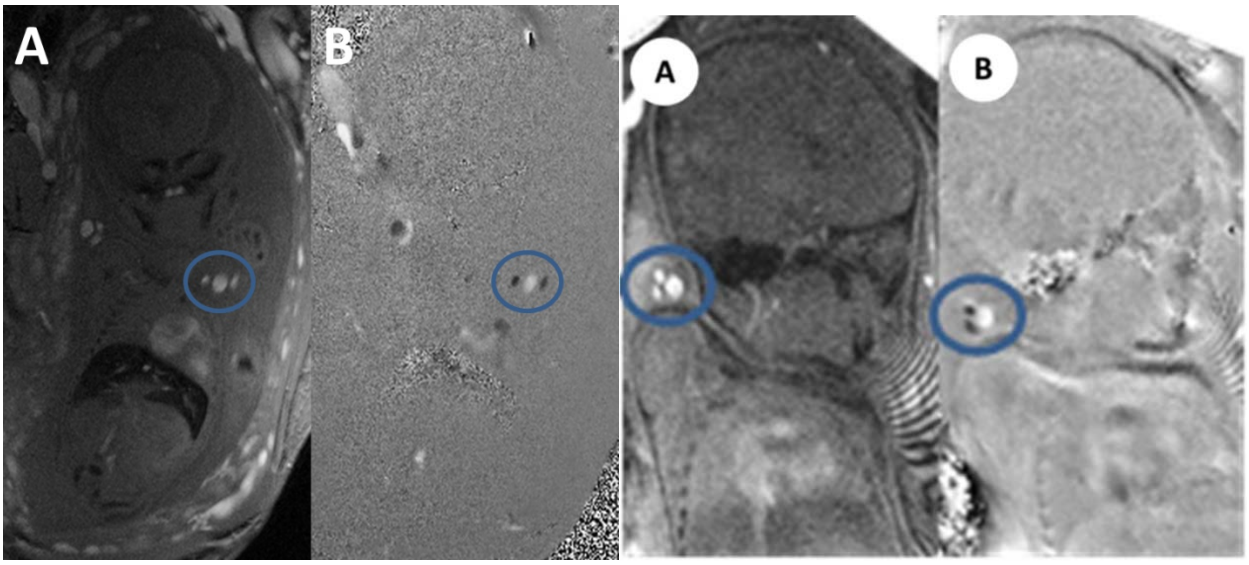

Figure 4.6: Magnitude (A) and the phase image (B) obtained from the PC-MRI. Representative images are shown from a second trimester fetus (left pair; GA – 25 4/7 weeks) and a third trimester (right pair; GA – 35 1/7 weeks) Note the different phase polarity in the artery and the vein.

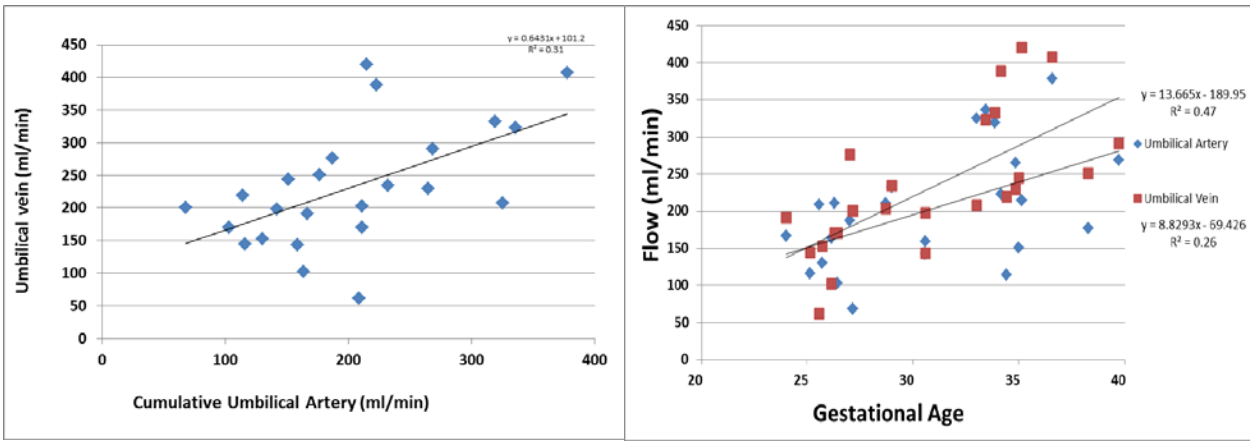

Figure 4.7: Plot of the arterial vs. venous flow in the umbilical cord. Note that the slope of the plot is close to 1, indicating equal arterial and venous flow. The plot on the right shows the arterial and venous flow plotted across gestational age.

As in previous studies, when applied in adult neck vessels, we found an excellent correlation (Pearson's r = 0.99) between ng-PCMRI measurements and measurements from conventional gated

methods. Furthermore, flow measures from umbilical vessels are in good agreement with flow measures reported in the literature, measured using ultrasound. The range of our flow varied from 68.4 – 378 ml/min and 61.8 – 420 ml/min (GA range: 24 – 39 5/7 weeks) in the umbilical artery and vein respectively. When extrapolated from the study of Lees et.al,[168] the average umbilical flow measure for the gestational ages used in our study was 261 ± 98 ml/min in the vein and 226 ± 67 ml/min in the artery, and those measured from our study was 232 ± 92ml/min and 203± 80 ml/min correspondingly. The average normalized flow in the umbilical vein in our cohort of subjects was 158 ml/min/kg, a similar measurement using retrospective gating has also been reported as 160 ml/min/kg [157]. And the average flow in the umbilical artery was 140 ml/min/kg, which is also in good agreement with previous studies[168, 169]. While the flow through the umbilical artery correlated well with what was measured in the umbilical vein (slope = 0.64), the flow in the vein was greater than that in both the arteries put together. This mismatch of ~12% is comparable to that seen in previous studies [168], pointing to a possible underestimate of flow in the umbilical arteries. This underestimation is in part explained by their small size and the subsequent partial voluming. At 33 weeks of gestation, the average area of the umbilical artery is 0.1 ± 0.01cm^2 (radius~2 voxels) and that of the vein is 0.46 ± 0.7 cm^2 (radius ~5 voxels) [168]. Simulation results showed that for vessels of radius 2 to 3 pixels, the error in flow estimation could be as large as 10% for a given vessel. The corresponding error in a vessel of radius ~ 5 voxels (umbilical vein) is less than 2%. Thus, the total flow in the two umbilical arteries could be underestimated by a factor greater than 10% which is what we see in our data. These systematic errors due to the partial voluming are similar to what has been reported even in conventional gated and could be responsible for the underestimation of the flow in the arteries[164]. Partial voluming leads to an error in both the quantified velocity as well as the area of the vessel, consequently leading to an error in the flow measure. One of the ways to minimize error in the final flow is by measuring the area of the vessel by considering the outer radius of the vessel [164]. Following this guideline, we also used the outer radius of the vessel while evaluating the vessel cross-sectional area. The flow encoding in this study was only in the through plane (slice direction), however, the umbilical artery has a helical coil geometry leading to

averaging over the slice thickness or only measuring the component of flow perpendicular to the slice. While the same was not a concern for the vein as they are homogeneous and the slice was positioned perpendicular to the umbilical cord.

The simulations included in this study only looked at the phase effects of the time varying velocity pattern. But, in fact, changes in velocity would also imply different reductions in the effective T1 of the blood within a cardiac cycle. Previous studies, however, have reported that the magnitude induced variations in the flow is low and can be reduced further using short TE and low flip angle, both of which were incorporated in our sequences [167]. In addition, the T1 relaxation of the fetal blood is comparable to the adult blood [170] and hence results from earlier studies can be readily extrapolated to fetal imaging. Signal-to-noise ratio (SNR) in fetal imaging is critical and can often be the limiting factor. In our simulation study, the starting SNR in the background tissue was 5:1, but the SNR in the final image is improved due to the averaging (N_{avg}). The precision of ng-PCMRI was not evaluated and the ability to detect differences could not be estimated practically. But, both these factors are heavily dependent on the experimental conditions of the vessel lumen (area and tortuosity), flow (pulsatality and acceleration factors), and physiology (heart-rate relative to TR). Further the changes in the lumen dimension within a heart rate was not simulated, fortunately this effect is not huge in the fetus as the maximal change in the diameter of the aorta in the third trimester is only about 6%.

Few previous studies have reported the use of MRI based methods to quantify umbilical flow [156, 158]. They are based on synthetic trigger approaches, where the data is oversampled and retrospectively sorted to reconstruct the images at different cardiac phases. However, this approach involves complex post processing and limitations in the techniques preclude it from being used in younger gestations [156]. The use of image based metric and periodicity constraints (modeled heart-rates) further possess challenges in the reconstruction and quantification. We have shown that this ng-PCMRI approach can even be used in the second trimester. In ng-PCMRI you can sensitize the measurements to the average velocity by reducing the venc, while in pg-PCMRI the Venc must be maintained high to correspond to the systolic velocity rates. This reduces the sensitivity for diastolic velocity, on the other

hand in ng-PCMRI there would be no aliasing (phase-wraps) in the final phase images even if the instantaneous velocity during a few phase encode lines is greater than the venc as it encodes the average velocity [171].

The data presented here could not be systematically compared with the triggered/standard measurements and the measure of accuracy is based on simulation, internal validation (artery vs.vein) or comparison with literature values. Comparative analyses across all gestational ages were not performed as this was a feasibility study. Fetal motion and poor SNR continue to be a challenge for the robust application of this in fetal imaging. This approach is readily transferable to clinical diagnostic studies due to the ease of imaging and reconstruction. Ng-PCMRI offers excellent potential to extend this approach beyond the umbilical cord and to all fetal vessels when care is taken to avoid partial voluming and positioning the imaging slice perpendicular to the vessel. This approach in combination with other quantitative MRI imaging tools can provide a more holistic understanding of the developmental physiology and provide a sensitive biomarker for diagnosis of fetal distress.

CHAPTER – 5: FEASIBILITY OF NON-CONTRAST FETAL MRA[2]

This chapter discusses a work where we optimized a conventional time-of-flight (2D TOF MRI) sequence for imaging the placental and fetal vessels without the need for any maternal breathold. This chapter also includes brief mention and preliminary results of the same sequence applied using a radial readout trajectory.

5. 1 INTRODUCTION:

Imaging the placental and fetal vasculature is clinically important for early identification of vascular malformations and anomalous vascular development especially in congenital heart disease [172-174]. Doppler imaging has been the mainstay for evaluating fetal vasculature by using 3D/4D ultrasound (US) and Spatiotemporal Image Correlation (STIC) [175-177]. However, issues related to limited US wave penetration in situations like maternal obesity, the presence of bony structures, abnormal fetal position, and oligohydramnios/anhydramnios could preclude proper US examination [178, 179]. In such situations, fetal magnetic resonance imaging has served as a valuable adjunct to ultrasound imaging (US) in obstetrics, especially for assessing the fetal central nervous system [180, 181]. However, the use of MR for assessing fetal vasculature has been extremely limited, due to fetal motion, contraindication for use of exogenous contrast agents during pregnancy, maternal respiratory motion, requirement of high resolution and the lack of fetal heart-rate based physiologic trigger signal which is required for some of the more advanced MR angiographic techniques [182, 183]. Countering fetal motion requires fast data acquisition schemes and high resolution for visualizing the small caliber vessels in the fetus. These are however, competing goals in MRI due to limited available signal to noise ratio (SNR). Imaging at higher field strengths offers high signal to noise ratio which could be leveraged for high resolution/fast imaging [184]. Imaging at the higher field of 3.0 Tesla (T), as opposed to conventional 1.5T, could provide this higher SNR. Fetal imaging at 3.0T field strength has been reported previously and recent studies have shown that it could be done safely with very low specific absorption rate (i.e., low rf energy deposition) [184, 185].

[2] This work has been published: "Neelavalli, J., **Krishnamurthy, U**., Jella, P. K., Mody, S. S., Yadav, B. K., Hendershot, K., ... & Hassan, S. S. (2016). Magnetic resonance angiography of fetal vasculature at 3.0 T. European radiology, 1-7.". All contents and results are thereupon reproduced from this manuscript.

Quantitative MR imaging techniques like arterial spin labeling [186] phase contrast MRI [187] and susceptibility weighted imaging based blood oximetry [188], that are increasingly being applied to the study of fetal physiology, often rely on the localization of afferent and efferent vasculature of the organ. Thus fetoplacental MRA also has an important role to play in the proper application of quantitative MR imaging methods in the fetus. In this work, we report the feasibility of obtaining non-contrast MRA in third-trimester fetuses at 3.0T that allows for 3D visualization of the fetal vasculature.

5.2 METHODS:

5.2.1 Sequence Optimization: Imaging parameters for the conventional 2D time of flight angiography sequences were modified keeping in mind the: a) expected range of physiologic blood flow velocities, b) size of the vascular structures, c) speed of acquisition and d) specific absorption rate of the sequence. The mean blood flow velocities in the umbilical vessels, the ductus venosus, aorta, inferior venacava and the fetal carotids are greater than 3cm/sec [189] from gestation 27 weeks and above (third trimester). Considering these speeds, the theoretical vessel contrast as a function of flip angle was plotted for blood flow velocities ranging from 3 to 30 cm/sec [189, 190], for 3.0T and 1.5T for a 2mm thick slice and a TR of 22ms (Fig. 5.1). A flip angle of 50^{o} was chosen to ensure enhancement of low velocities and for keeping the SAR low. The diameter of the umbilical vessels, the major vessels of the heart and its branches including the carotids is typically greater than 3mm in the third trimester [191, 192]. Therefore, a voxel size of 0.4 - 0.7 mm isotropic (in-plane) was used so that vessels occupy 3 to 4 voxels or above. The final sequence parameters of the 2D TOF for fetal MRA are provided in table 5.1. Parameters of the conventional TOF are included for comparison. A saturation band was not used in order to keep the SAR low. The resultant fetal MRA sequence acquired one image slice every 3 to 4 seconds (depending on the resolution used).

	Mode	TE (ms)	TR (ms)	Reconstructed Resolution (mm^3)	FA (degree)	BW (Hz/pixel)	# Slices	Acq. Time (min)	Parallel Imaging
Conventional	3D	3.4-11.3	25	(0.75-1) x (0.75-1) x (1.5-2)	20	42	50-70	5-7	2
Fetal MRA	2D	4.92	22	(0.4-0.7) x (0.4-0.7) x (1.5-2)	50	241	26-64	2-5	2

Table 5.1: Sequence parameters for 2D fetal MRA contrasted against the conventionally used 3D TOF MRA of adult imaging.

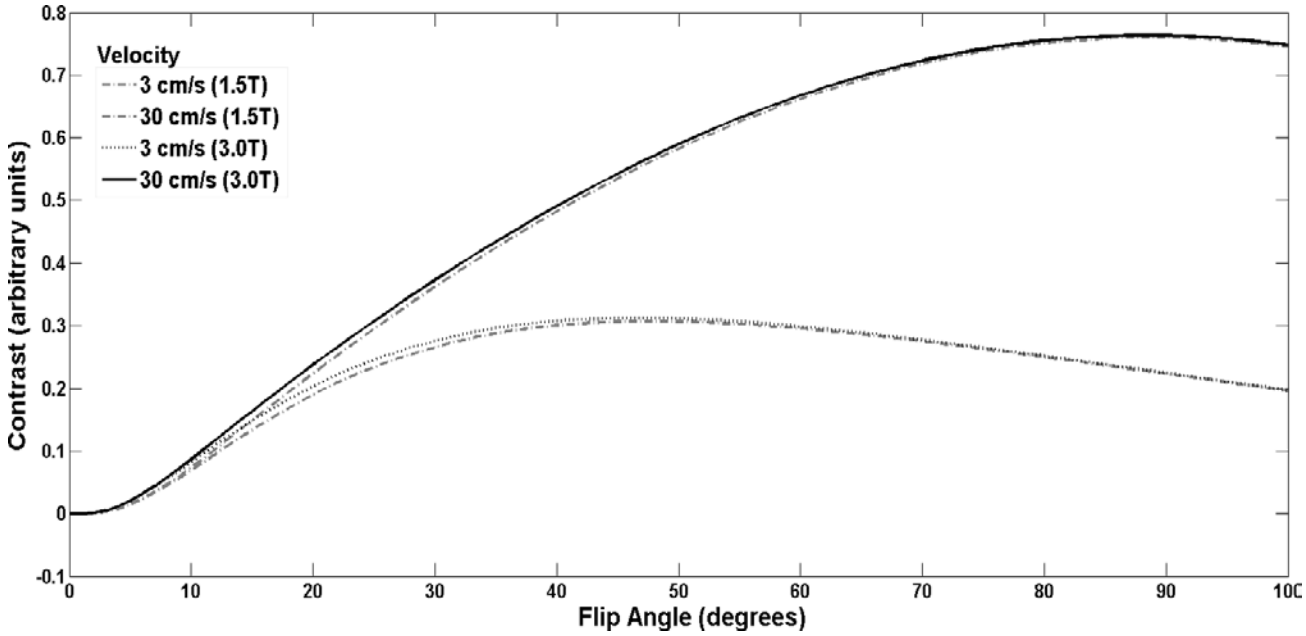

Figure 5.1: Theoretical contrast between the blood and background tissue vs. flip angle for blood velocities of 3 and 30 cm/sec. Experimental conditions; TR = 22 ms; TE = 5msec; T1 of blood [193, 194] = 1890ms (3.0T), 1400 (1.5T); T1 of background tissue [195, 196] = 2500ms (3.0T), 1700 (1.5T), spin density of blood and background [197] 0.82 and 0.83 (arbitrary units), T2 of blood and background tissue [196, 198]= 200ms. A flip angle of 50^o was used to ensure enhancement at low velocities while maintaining low SAR. Almost identical curves for 3.T and 1.5T indicate that similar data may be acquired at 1.5T as well, using these parameters.

5.2.2 MRI Data Acquisition: The study was approved by the local institutional review board and informed consent was obtained from all subjects before the MRI scan. As part of a larger ongoing study, the fetal/placental MRA data was acquired whenever the scan time permitted in a non-sequential manner in third trimester subjects and results from 5 subjects are presented here. The median and interquartile values for the subjects were 36 weeks 4 days and 1 day, respectively. All subjects had normal US examination within one week prior to the MRI scan.

Fetal MRI was performed on a 3.0T Siemens Verio system (Erlangen, Germany) using a four-channel body flex array and the spine coil. Routine anatomical scans using a 2D T2 weighted (HASTE) sequence were followed by the acquisition of the 2D fetal MRA sequence for imaging the fetal vessels. Placental and umbilical vessels were visualized when they were present in the imaging field of view. Whenever possible, the MRA was repeated to achieve appropriate coverage or when fetal motion was encountered. Images containing significant motion were excluded and image volumes were processed for vascular network visualization in 3D in VolView [199] (www.kitware.com). 2D maximum intensity projections (MIPs) where then created at the appropriate orientation from these 3D volumes. Videos of 3D reconstructions and the original DICOM data are provided in the supplementary material.

5.3 RESULTS

The great vessels of the fetal heart were clearly visualized (Fig 5.2). Umbilical circulation with the UAs joining the aorta and the umbilical vein joining the inferior vena cava was observed (Fig 5.3). Fetal neck vessels, the common carotids arising from the subclavian branches of the aorta, the internal carotids joining to form the circle of Willis, the transverse sinus, jugular veins, the vertebral arteries joining to form the basilar artery were clearly visualized in a 36 week and 4 day fetus (Fig 5.4). Intracranial vessels like superior sagittal sinus, transverse sinus and the middle cerebral artery, that were on the order of 1.5mm to 2mm in diameter, were visualized and reconstructed in the 3D view. Chorionic vessels of the placenta as well as the vessels on the maternal side were also visualized (Fig 5.5). The SAR of the MRA as well as that of the HASTE sequence were < 0.25 W/Kg and 0.9 W/Kg, respectively.

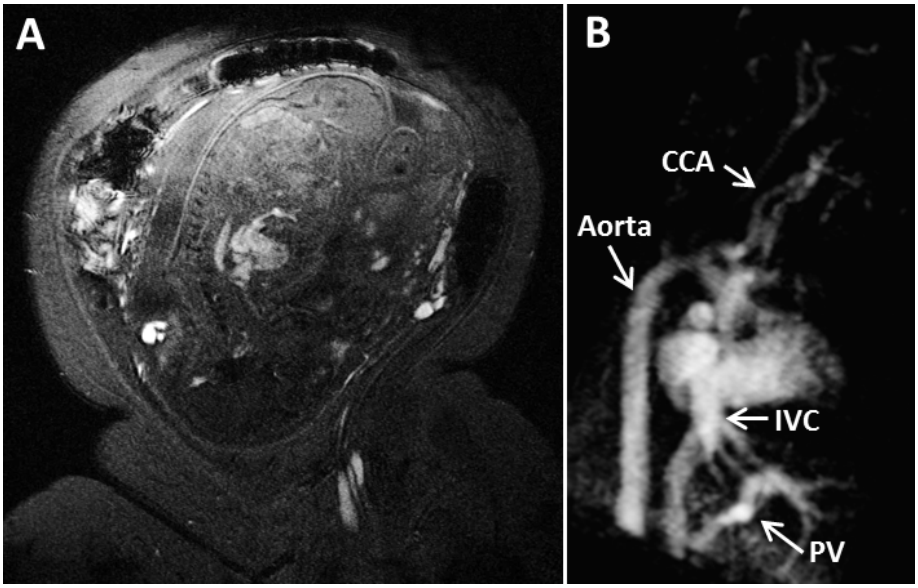

Figure 5.2: A) 2D TOF MRA image showing the fetus in the head down position with the fetal heart clearly visible. B) Maximum intensity projection obtained from the 3D vascular volume reconstructed from the 2D TOF data (shown in A). Fetal heart and its major vessels are visualized (Gestational Age – 37 weeks). IVC – Inferior Venacava; PV – Portal Vein, CCA – common carotid artery.

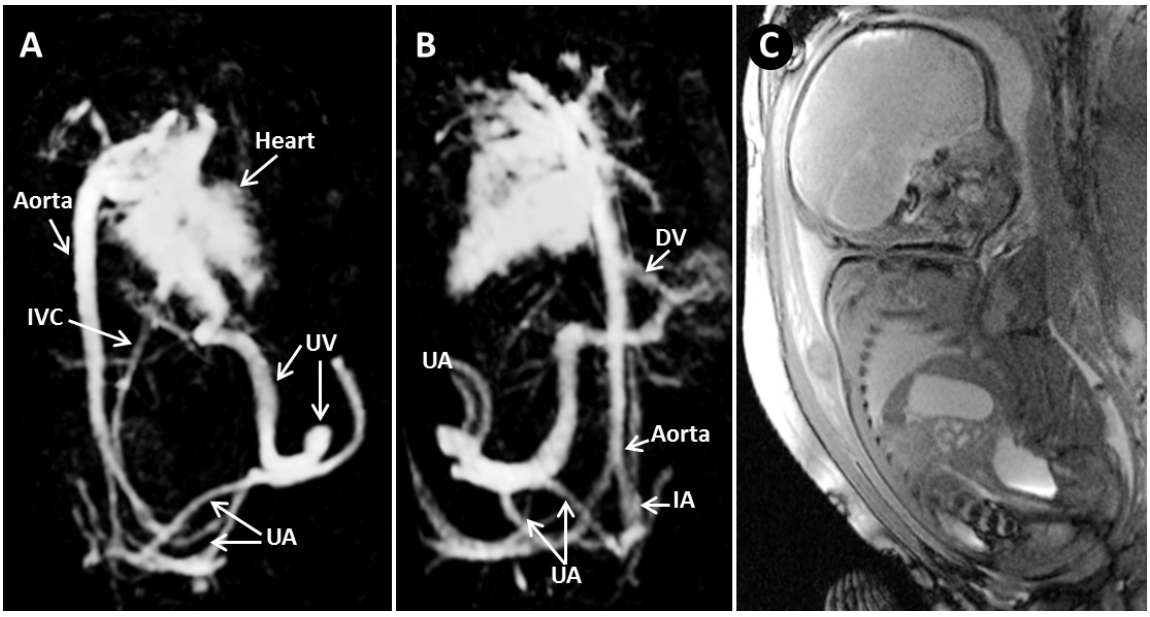

Figure 5.3: Visualization of the umbilical-fetal circulation. A,B – Orthogonal views of the umbilical-fetal vasculature MIPs (Gestational age – 36 weeks 4 days) showing the umbilical arteries joining branches of the descending Aorta and the umbilical vein joining the Ductus venousus. C – Anatomical image showing

the orientation of the fetal position; IVC – Inferior Venacava; UV – Umbilical vein; UA – Umbilical Artery; IA – Iliac Artery; DV – Ductus Venosus.

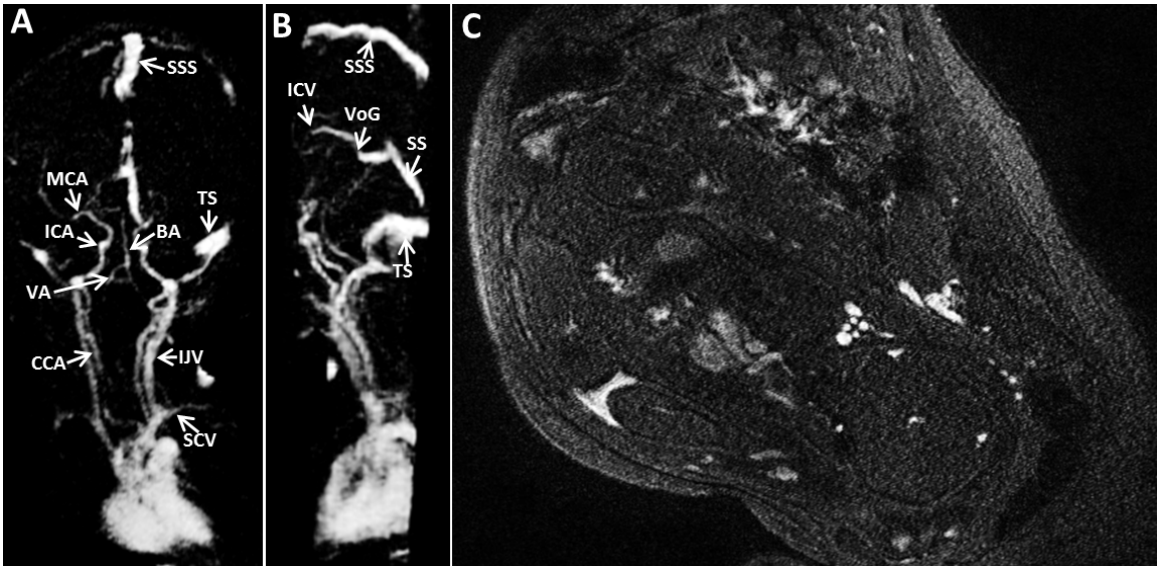

Figure 5.4: Coronal (A) and Sagittal (B) MIP views, relative to the fetus, of the fetal head and neck vessels. C) A single 2D slice from the TOF MRA volume from which the 3D MIPs were generated. (Gestational Age – 36 weeks 4 days). SSS – Superior Saggital Sinus; ICV – Internal Cerebral Vein; VoG – Vein of Galen; SS – Straight Sinus; MCA – Middle Cerebral Artery; TS – Transverse Sinus; ICA – Internal Carotid Artery; BA – Basillar Artery; VA – Vertebral Artery; CCA – Common Carotid Artery; IJV – Internal Jugular Vein; SCV – Sub Clavian Vein.

5.4 DISCUSSION:

These results show that 2D TOF MRA can indeed provide excellent depiction of fetal and placental vasculature as well at 3.0T. In many cases, minimal fetal motion allowed for the successful production of high quality 3D reconstructions despite the lack of maternal breath-hold. This may be largely due to the rough synchronization of the per-slice imaging time of 3 to 4 seconds with the typical maternal respiration rate, effectively leading to pseudo respiratory gating [200]. The relatively long TR helped in reducing the SAR while increasing the blood signal due to higher inflow effect of blood. Because of the high flow velocities in the fetus and placenta, using a similarly long TR and thin slice it

may be possible to obtain such MRA of the fetus in the third trimester at 1.5T as well as suggested by Fig 5.1.

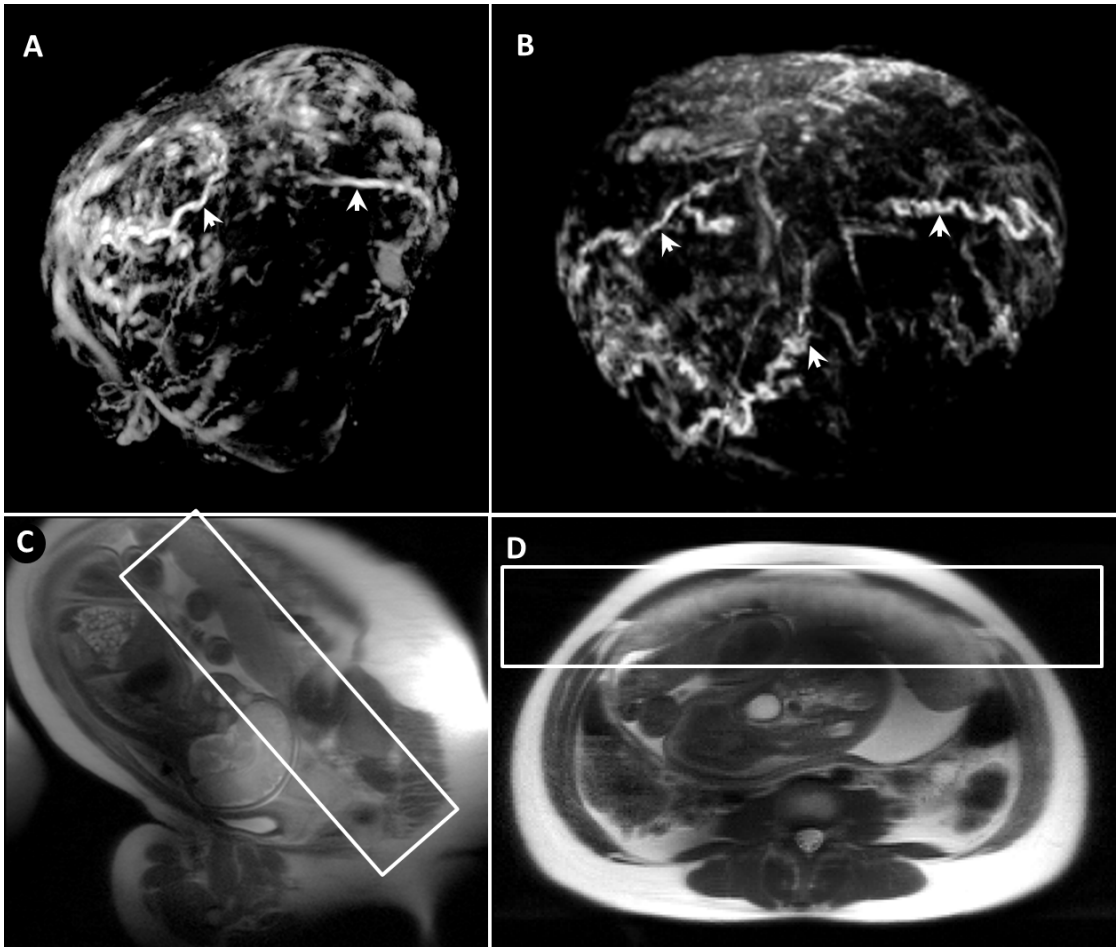

Figure 5.5.: (A) and (B) - Basal plate vasculature on the maternal side of the placenta. C) and D) T2 HASTE images showing the volume covered for the MRA scan for (A) and (B) respectively. The arrowhead indicates basal plate vessels on the Uterine Side of the placenta (A,C : Gestational Age – 36 weeks 4 days; B,D: Gestational Age – 36 weeks 5 days).

A major advantage of MRA is its larger field of view that provides a global perspective of the vascular network of mother and fetus in relation to the other anatomical structures which is helpful for identification of syndromic vascular malformations such as Klippel-Trenauny, Hereditary Hemorrhagic Telangiectasia (AKA Osler-Weber-Rendu), etc. In these cases, vascular malformations may be located

anywhere in the fetus, so a larger viewing window is advantageous for improved sensitivity over US as a screening modality. High resolution in MR helps in the visualization of small fetal vessels, particularly in

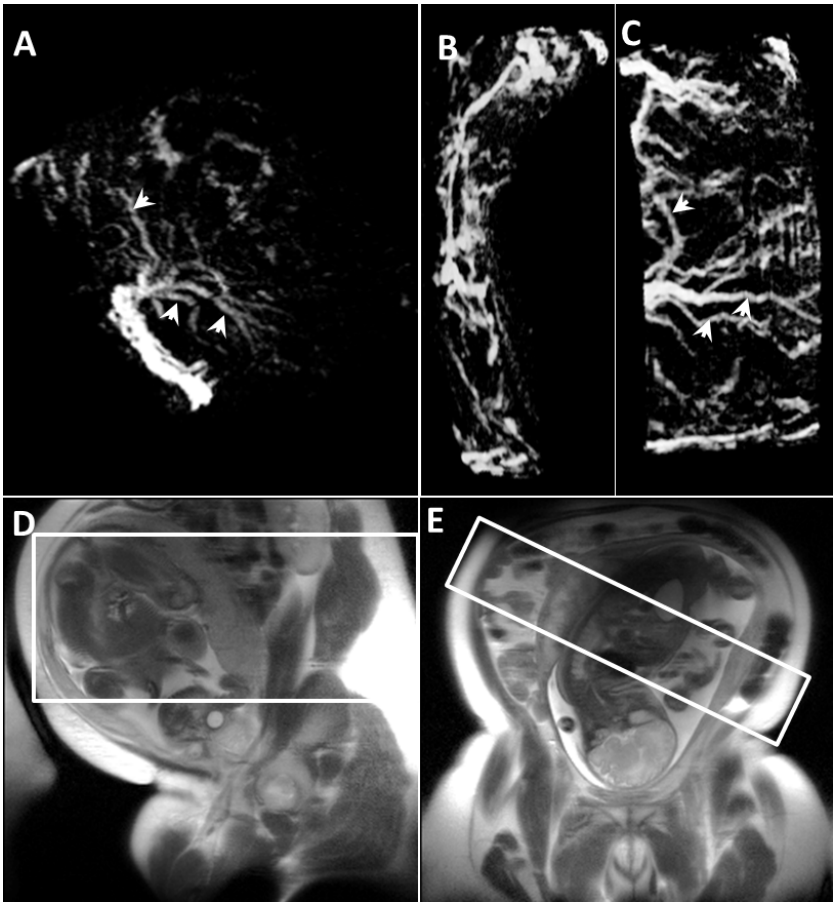

Figure 5.6: A,B,C – MRA of the placental chorionic plate vessels. Primary and secondary branches of the chorionic plate vessels (arrow heads) are visualized. D,E - Corresponding anatomical images showing the volume covered in the MRA acquisition. (A,D: Gestational Age- 36 weeks 4 days; B,C,E : Gestational Age – 37 weeks).

the head and neck, which are difficult to visualize with U/S due to the presence of the skull. Larger field of view also helps in global evaluation of the placental vasculature and higher resolution allows for evaluation of the chorionic surface vessels. Recent works have indicated that chorionic vessel density/distribution may be an important indicator of placental health [201, 202]. Placental MRA may have an important role to play in this assessment, especially in second and third trimesters.

There are a few limitations in this work. The technique was not applied in the same fetal anatomical location consistently. Furthermore, the technique was applied non-sequentially with variable volume coverage due to scan-time restrictions which precluded systematic analysis of the success rate of the technique. Systematic assessment of the diagnostic utility will be the focus of our future work. Nevertheless, the current report is the first step in showing the potential of the TOF MRA technique in visualizing fetal vasculature in-utero using MRI. Faster scanning speeds may be achieved using non-Cartesian sampling methods like radial/spiral combined with compressed sensing (CS) [203-205]. These trajectories are naturally insensitive to motion and/or amenable to motion correction [206] and thus may further improve the robustness of the technique for application in the second trimester as well. Combined with parallel imaging, these methods may further help speed up data acquisition and/or improve SNR. This feasibility study helps us validate the clinical viability of 2D TOF MR Angiography data for imaging the fetal vasculature at 3.0T. We report that 3D reconstruction and visualization of the fetal vasculature is possible on a conventional clinical MRI without the need for any new hardware or sequences.

5.5 ROLE OF NON-CARTESIAN SAMPLING IN FETAL TOF-MRA

In the above study, it was observed that the MRA technique was not robust in cases of younger gestation fetuses (second-trimester) or in cases where there was extreme fetal motion. Considering the small lumen dimensions, large field of view and the presence of fetal/maternal-respiratory motion, a high-resolution sequence with relative insensitivity to fetal motion is warranted to improve the success rate of the fetal MRAs. Non-Cartesian sampling, notably radial k-space sampling which oversamples the central k-space can provide immunity to motion related artifacts. It also has the ability to image at higher resolutions due to the absence of a phase encoding step. This also provides the added advantage of large FOV imaging as it is only dependent on the read/frequency encoding. One drawback of the radial k-space sampling method is the susceptibility to gradient delays causing relative shifts between the sampling window and the read-out gradient. Manufactures, address this delay by modifying the moment of the dephasing lobe which ensures that the echo center happens at the center of the sampling window. This approach is very robust for a non-flow compensated gradient structure; addition of a bipolar gradient as

required for MRA (or) SWI makes it extremely hard to shift the echo center by changing the moment of one gradient while satisfying the conditions that both the zeroth and first moment of the readout to be zero at the echo. We hypothesized that radial sampling MRA would be beneficial on two counts over conventional Cartesian MRA for fetal applications; (a) Improved image quality i.e. decreased sensitivity to fetal motion and (b) Ability to perform high-resolution imaging.

	Mode	Number of spokes (over 360^0)	Partial Fourier	TE (ms)	TR (ms)	Reconstructed Resolution (mm^3)	FA (degree)	BW (Hz/pixel)	# Slices
Radial MRA	2D	361	33%	5.3	22	(0.4-0.6) x (0.4-0.6) x 2	50	240-300	26-64

Table 5.2: Sequence parameters for 2D fetal radial MRA.

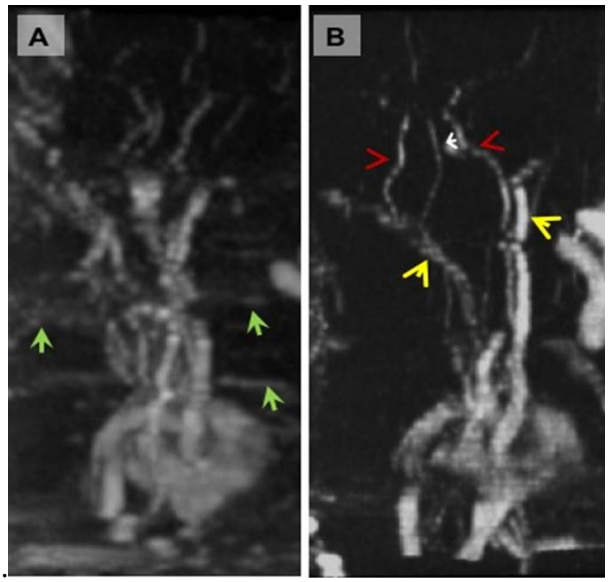

Figure 5.7: Comparison of radial (B) vs. Cartesian (A) sampling for fetal angiography. The data corruption from motion, which appears as streaks (green arrows) and broken vessels in the left image (Cartesian) are absent in the image on the right (Radial) taken from a fetus in third trimester. Fetal internal carotids (red arrowhead), jugular (yellow arrowhead) and the basilar artery (small white arrow) are clearly seen in the radial MRA image.

The previously described Cartesian TOF – MRA sequence was modified to readout data radially. The duration of each slice was 4.5- 5.5 sec depending on the resolution and FOV used. The sequence parameters are summarized in the table 5.2. The images were reconstructed by performing gridding (http://mrsrl.stanford.edu/~brian/gridding/) and inverse Fourier transform. The added advantage of using radial sampling is the ability to do flow-compensation in all dimensions without additional time. With long TRs used in fetal angiography for reduced SAR, multi-echo readouts were also possible, allowing for T2* quantification of fetal blood at the same time. Fetal MRI was performed on a subset of the cases where there was moderate to no motion artifacts seen on the Cartesian MRA datasets.

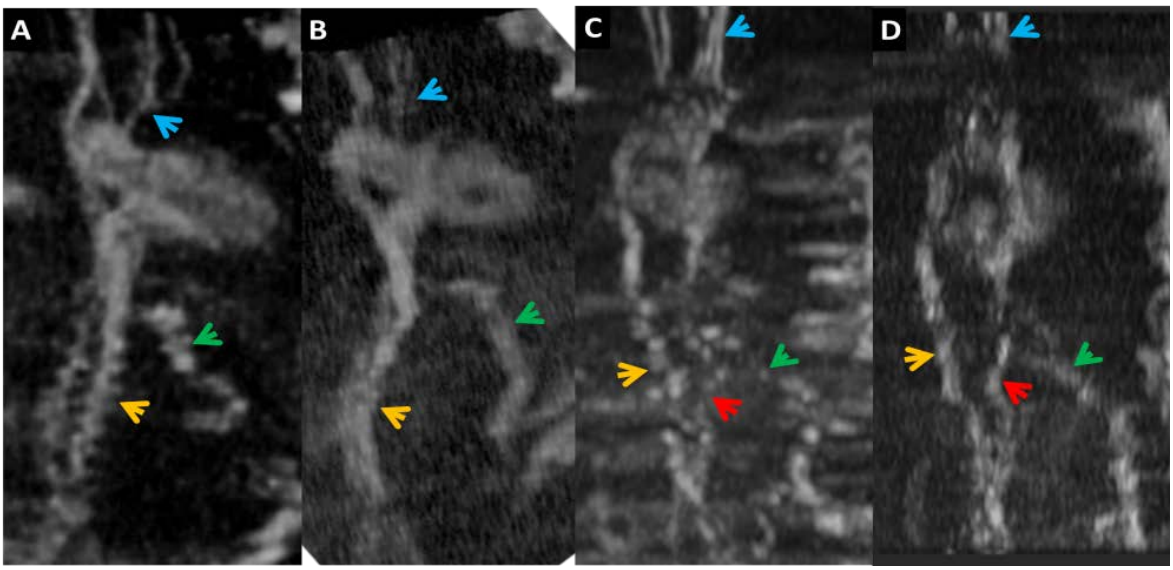

Figure 5.8: MIPS of two fetuses; conventional Cartesian MRA with TE = 4.92ms (A,C) alongside their corresponding radial MRA (B,D) with TE = 5.33ms, Note the edges of the vessel lumen (yellow arrowhead), the continuity of the umbilical vein (green arrowhead) and the inferior Venacava (red arrowhead), however the Cartesian data showed the neck vessel more distinctly. Please note the fetus could have changed position between the two successive scans. Gestational Age of A,B: 27 weeks and 6 days; Of C,D 26 weeks 6 days

5.5.1 Preliminary results: In cases of no fetal motion, particularly in the third trimester, the radial-MRAs were as good as those obtained from regular Cartesian MRA (Figure 5.7 & 5.9), however, in cases of moderate fetal motion, the rMRAs performed much better (Figure 5.8). The advantages of radial were more evident when maximum intensity projections were made to visualize the whole volume. The following images highlight the potential for radial sampling in fetal angiographic applications

5.5.2 Discussion: As demonstrated in the above images, radially sampled data provided the touted advantage of motion-insensitivity in fetal angiography. The long TR allowed (for SAR considerations) fully FC multi-echo readouts that offers: (a) T2* mapping of the fetal vasculature (fig 5.9 a,b); b) enhancement of the SNR of the first echo through data averaging (figure 5.9.c); and (c) using the phase from the second echo for MR susceptometry However, the challenges with trajectory corrections and reconstructions impede the rapid acceptance of such non-conventional approaches for applications in clinic. Due to the nature of the coverage of the k-space, any small deviations in the gradient timings or amplitudes results in the spoke not passing thorough the center of k-space. This can result in signal voids or mis-registration artifacts while reconstructing the image. These effects can often be detrimental to the quality of the final images making it non-diagnostic. This effect is further enhanced at higher echo times due to influences of local ΔB. Another potential concern is the relative lower SNR and higher time for polar sampling when compared to corresponding to Cartesian imaging. This can be easily offset by use of appropriate filtering, accelerating techniques like parallel imaging (radial-GRAPPA, Espirit)[207], partial Fourier[208] and compressed sensing[209]. This feasibility study concludes that, the radial sampling scheme holds great promise for fetal angiography applications. Future works that can incorporate flow compensated multi-spoke readout within the same TR could further accelerate such acquisitions, bringing the acquisition time under 2 or 3 seconds per slice, with the ability for simultaneous T2* quantification.

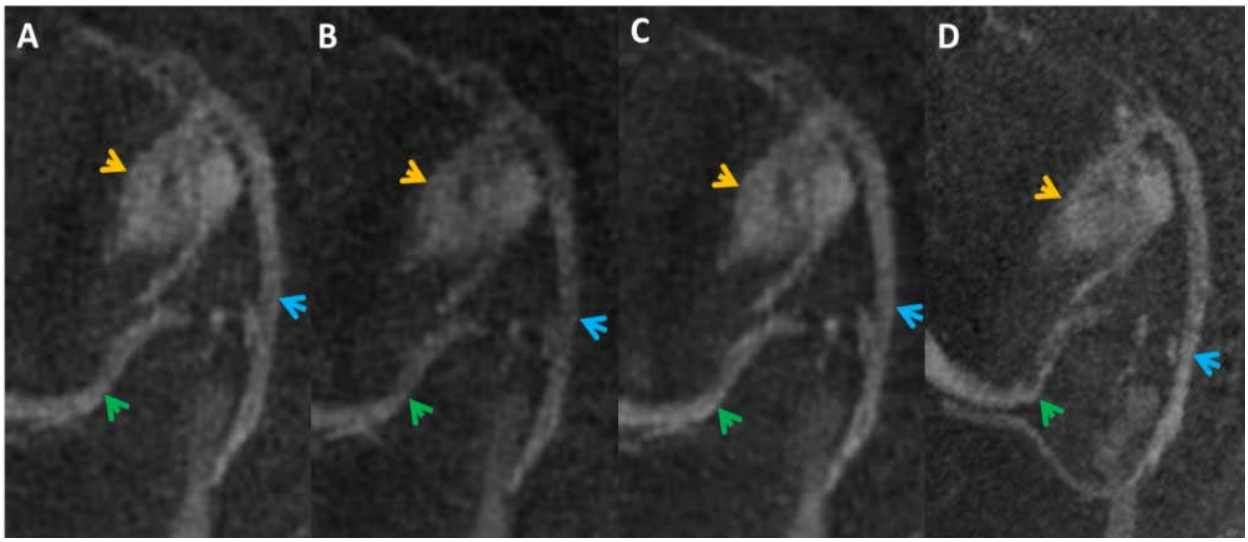

Figure 5.9: MIPS (10 mm) of the dual echo radial MRA with TE = 5.33ms (A) and TE = 10.33ms (B), alongside the averaged image of the two echos (C) and conventional Cartesian MRA (TE = 4.92ms) (D). Fetal heart (orange arrowhead), fetal aorta (blue arrowhead) and umbilical vein (green arrowhead), are clearly seen. The dual echo data (A,B) can be used to estimate the T2* map. Gestational Age: 27 weeks and 5 days

CHAPTER 6: SUMMARY AND FUTURE DIRECTIONS

The development of MRI methods for imaging the feto-placental vasculature and blood flow was the major focus of this thesis. To address this, Cartesian 2D TOF imaging sequence was optimized and a new 2D TOF sequence with polar sampling was developed and applied successfully on the fetus. A simple non-gated Phase-Contrast (ng-PC) was also optimized and applied. The simulations indicated that the quantified flow measurements have an error of the order of ~10%. All this was done on a 3.0T research MRI setting. This has more relevance than ever before as more and more research sites and hospitals are migrating to 3.0T MRI for all their fetal MR scans.

While, all the methods and sequences discussed herein have been validated using simulations and in normal pregnant volunteers, the current studies have not been extended to clinical subjects. This might need further investigation and simplification as it needs to be used by clinicians or MR technologists without specialization in fetal imaging. The applications of these approaches go beyond fetal imaging and have great potential in general abdominal imaging, where patient conditions preclude breath-holds or use of any exogenous contrast agents and in pediatric and patients having motion artifacts. The current work in most cases should be seen as first step towards establishment of standardized protocols in clinical settings. Techniques for acceleration like compressed sensing [209, 210] and constrained reconstruction have been well studied and can be easily incorporated into the sequences discussed above for fetal applications.

Moreover, the future works should also focus on identifying subject specific localized SAR or temperature maps in real time for negating any concerns of safety. Such an approach is also necessary for optimizing sequences by having a better estimate of boundary conditions for RF based temperature increase. While many recent publications have highlighted the feasibility of such approaches, they should further be explored. Further the biological effects of exposure of fetus to different EM waves at different gestational ages must be understood. But the advantage of moving to higher fields opens up the ability to perform functional imaging and use other advanced sequences which are require high baseline SNR. The parameters used in our studies can be used by other groups when they migrate to 3.0T for their fetal

imaging workflow.

Here we have developed a non-contrast PC MRI sequence to measure the average blood flow. But this can be readily extended to perform time resolved imaging using techniques like pseudo or retrospective gating. However, even in its current form it has many application in diagnosis and for measuring the average flow [211]. Particularly combining this approach and a radial/Spiral sampling scheme, the amplitude/phase of the central point can be used to bin the data according to the different cardiac phases [212-214]. A case of immediate applications could be to combine the PCMRI measurements with other MRI based oxygenation/perfusion measurements to study the metabolic oxygen requirements of the fetus or more specifically within a fetal organ (e.g. Brain [215]). The availability of tools to perform such measurements enables us to diagnosis incidents of hypo-oxygenation/ischemic insults and the ability to test novel interventional approaches.

To the best of our knowledge, this is the first study demonstrating the abilty to perform non-contrast MRA in fetus in-utero. Not just in the fetus this method has also been shown to be useful in imaging the placental vasculature. This enables us to study the vasculature in the whole fetus, which otherwise is not possible with US. This now enables us to improve our other MRI sequences which require the knowledge of the spatial orientation of the vessels. The sequence has also been extended to projection reconstruction, the benefits of which have been briefly demonstrated. There is greater potential for such approaches given the ease with which they can be combined with CS based approaches. Specifically for fetal imaging the requirement for a longer TR to reduce SAR might be beneficial for the development of RARE like approaches for acquiring multiple lines within a TR even with polar sampling.

In conclusion, the field of inutero fetal imaging is still developing and there is a greater role for quantitative imaging in the diagnosis and management of perinatal conditions. The studies and results presented here provide excellent tools to develop other MRI sequences or to apply it for diagnostic applications.

APPENDIX: LOCAL SAR ESTIMATION AND TEMPERATURE INCREASE

Chapter two of this report described the possibility of performing diagnostic quality, high resolution MRI of the fetus at 3.0T all the while maintaining a specific absorption rate (SAR) levels lower than those prescribed in the regulations and lower than the levels currently being used at 1.5T. It is to be noted and acknowledged that the SAR values reported by the manufacturers are not the true SAR but only an estimation, which is usually a conservative one (i.e., overestimated) [216]. The regulatory limits for RF exposure are described only in terms of whole body SAR and are summarized in table A.1 [217]. These numbers are specified for adults; however for fetal imaging no such limits are prescribed; only recommendations are made. The ICNIRP (International commission on non-ionizing radiation protection) alone recommends a specific limit on rise of temperature to less than 0.5^0C and the temperature of any fetal organ/tissue to be below 38^0C [218, 219]. Given the new improvements in RF excitation methods such as parallel transmission and simultaneous multislice excitation (SMS) pulses, sequences with preparatory RF pulses and the migration to higher field strengths (3.0T for fetal and 7.0T for adult), SAR needs to be looked at carefully. A conservative single valued global average would not be an accurate representation of the energy deposition. And the need for an individualized local SAR measurement attains greater importance from a safety perspective and in the context of maximizing advantages of the high fields.

Regulatory Authority	Limit	Whole Body Average	Heat Average	Head, Trunk Local SAR	Extremities Local
IEC (6 Min Avg)	Normal (All patients)	2 W/Kg	3.2 W/Kg	10 W/Kg	20 W/Kg
	First level (Supervised)	4 W/Kg	3.2 W/Kg	10 W/Kg	20 W/Kg
	Second Level (Research; IRB approval)	4 W/kg	> 3.2 W/Kg	> 10 W/Kg	> 20 W/Kg
	Localized Heating limit	39^0 C in 10g tissue	38^0 C in 10g tissue		40^0 C in 10g
FDA		4 W/Kg (15 min)	3 W/Kg (10 min)	8 W/Kg in 1g (10 min)	12 W/Kg in 1g (5 min)

Table A.1: IEC (International electrotechnical commission; Europe) and FDA (Food and drug administration; USA) guidelines on SAR and heating in human studies.[217] IRB – Institutional review board

The true region by region energy deposition and the heating of the tissue depends on multiple aspects including the power deposited, frequency, orientation of the $\vec{E}$ and $\vec{B}$ fields, dimensions and orientation of the object being imaged relative to the RF transmit configuration [220]. Many research groups have looked at the local SAR and heating in pregnant women model incorporating the properties of 35 or more tissues. The true estimation of SAR for individual subjects being scanned is highly impractical as it depends on many parameters including the location of the placenta and fetus within the abdominal region [221]. However it is important to note that in general the SAR is higher in amniotic fluid and muscle tissue due to higher electrical conductivity [222]. While there are no hard restrictions on the heating due to MR RF exposure, ICNIRP suggests that there would be no fetal damage if the temperature of the fetus is always below 38^0 and the rise in maternal body temperature is below 0.5^0 C during the entire scan and recommends extreme caution when imaging fetus in 4T and greater [218].

Numerical simulations have been performed by various groups to see the compliance of the above two conditions for normal operating mode of the magnets at a SAR (Whole body average) <2 W/kg. While JW hand et al [133] report that the maximum local fetal temperature of 38^0, could be possible within 7.5 minutes of scan, Kikuchi et al [222] report that a 0.5C rise in fetal temperature would require about 47 min of scanning at 2 W/Kg (fig. A.1). The difference in these results and some of the other simulation studies is because they use different pregnant women models, different set of coil configurations, and patient locations within the bore, inclusion or the exclusion of sweating/ bioheat transfer models etc. Animal studies (pregnant pig) using fiber optic temperature sensors inserted in the uterus and within different sections of the fetus [223, 224]. The study by Cannie et. al. reported that there was less than 1^0 C rise in temperature when imaging for 30 min even using high SAR protocols [223] but a temperature increase of 2.5^0 C was possible on scans lasting greater than an hour and using high SAR sequences. On the other hand, an older study found no heating while using standard HASTE sequence[224]. These experimental and simulation studies suggest that with maternal whole body SAR < 2 W/kg, there is no major complications to the fetus if the scan time is limited to 30 min. As

recommended by Gowland et al, [225], following these minor points could further reduce any heating due to RF exposure.

A. Fetal MRI scans should only be carried under the normal operation mode SAR (Whole body) < 2W/Kg

B. High SAR a low SAR sequences must be interspersed.

C. Ambient scanner environment

(1) bore temperature around 24^0C

(2) Good air flow/ventilation

(3) humidity ~ 60%

(4) No blankets on the patient

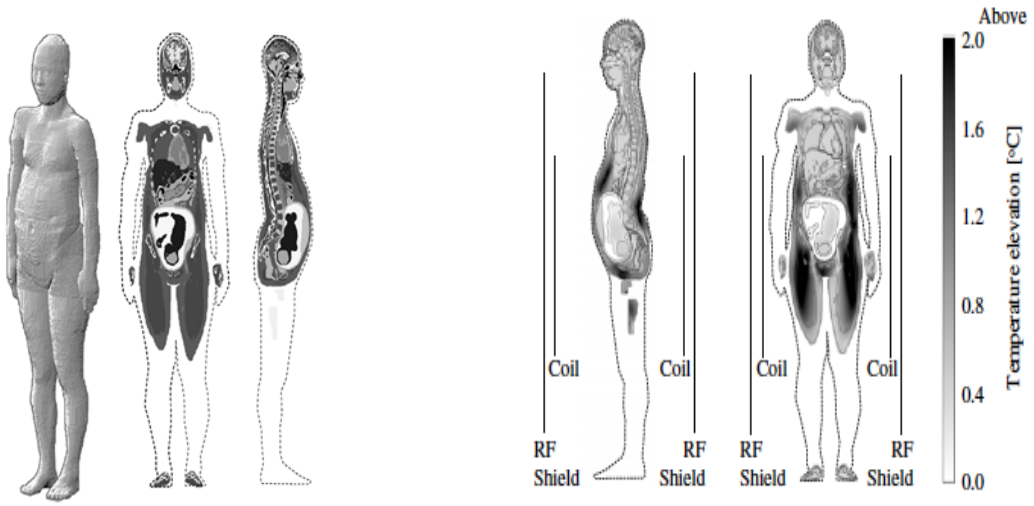

Figure A.1: human tissue model used in pregnancy to study the SAR and temperature distribution. Adopted from [222].

More recent studies have tried to develop quick methods for generation of individualized regional SAR measurements [226, 227]. These approaches are based on rapid tissue segmentation/registration. The conductivity of the target tissues are adopted from a look up table and a modified Maxwell's equation is used to solve for the voxel–by-voxel energy distribution maps. Once a nominal map is generated it can be scaled to calculate local SAR for different sequence parameters, RF pulse shapes and times. While there

have been demonstrations of the approach in abdominal imaging (for cervical imaging) no clinical implementations of the same have been reported. Another promising method to identify hot-spots and regional temperature increases using principles of frequency shifts, thermo acoustic imaging often collectively classified as MR thermometry have also been proposed [228-230]. These approaches might in future be able to predict patient specific local SAR and allow us to exploit the MRI sequences, within safety limits for better image quality.

REFERENCES

1. Garel, C., et al., *Fetal MRI: normal gestational landmarks for cerebral biometry, gyration and myelination.* Child's Nervous System, 2003. **19**(7-8): p. 422-425.
2. Garel, C., et al., *Fetal cerebral cortex: normal gestational landmarks identified using prenatal MR imaging.* American Journal of Neuroradiology, 2001. **22**(1): p. 184-189.
3. Paul, T., *The Future of qMRI: Conclusions and Speculation*, in *Quantitative MRI of the Brain: Measuring Changes Caused by Disease*, T. Paul, Editor. 2005, John Wiley & Sons. p. 613 - 618.
4. Lequin, M., et al. *Magnetic resonance imaging in neonatal stroke*. in *Seminars in Fetal and Neonatal Medicine*. 2009. Elsevier.
5. Clouchoux, C. and C. Limperopoulos, *Novel applications of quantitative MRI for the fetal brain.* Pediatric radiology, 2012. **42**(1): p. 24-32.
6. Biegon, A. and C. Hoffmann, *Quantitative magnetic resonance imaging of the fetal brain in utero: Methods and applications.* World journal of radiology, 2014. **6**(8): p. 523.
7. Gardosi, J., *Clinical strategies for improving the detection of fetal growth restriction.* Clinics in perinatology, 2011. **38**(1): p. 21-31.
8. Haddad, L.J., J.S. Ross, and N, *United Nations System Standing Committee on, 5th report on the world nutrition situation : nutrition for improved development outcomes.* 2004.
9. Kady, S.M. and J. Gardosi, *Perinatal mortality and fetal growth restriction.* Best practice & research Clinical obstetrics & gynaecology, 2004. **18**(3): p. 397-410.
10. Longo, S., et al., *Short-term and long-term sequelae in intrauterine growth retardation (IUGR).* The Journal of Maternal-Fetal & Neonatal Medicine, 2013. **26**(3): p. 222-225.
11. Papageorghiou, A., et al., *Multicenter screening for pre-eclampsia and fetal growth restriction by transvaginal uterine artery Doppler at 23 weeks of gestation.* Ultrasound in Obstetrics and Gynecology, 2001. **18**(5): p. 441-449.

12. Backe, B., *Effectiveness of antenatal care: a population based study.* BJOG: An International Journal of Obstetrics & Gynaecology, 1993. **100**(8): p. 727-732.

13. Baschat, A.A., *Pathophysiology of fetal growth restriction: implications for diagnosis and surveillance.* Obstetrical & gynecological survey, 2004. **59**(8): p. 617-627.

14. Figueras, F. and J. Gardosi, *Intrauterine growth restriction: new concepts in antenatal surveillance, diagnosis, and management.* American journal of obstetrics and gynecology, 2011. **204**(4): p. 288-300.

15. Giles, W.B., B.J. Trudinger, and P.J. Baird, *Fetal umbilical artery flow velocity waveforms and placental resistance: pathological correlation.* Br J Obstet Gynaecol, 1985. **92**(1): p. 31-38.

16. Ferrazzi, E., et al., *Uterine Doppler velocimetry and placental hypoxic-ischemic lesion in pregnancies with fetal intrauterine growth restriction.* Placenta, 1999. **20**(5): p. 389-394.

17. Buehler, D.M., et al., *Effectiveness of individualized developmental care for low-risk preterm infants: behavioral and electrophysiologic evidence.* Pediatrics, 1995. **96**(5): p. 923-932.

18. D, P., *Fetal MRI*. 2011.

19. Raju, T.N., et al., *Ischemic perinatal stroke: summary of a workshop sponsored by the National Institute of Child Health and Human Development and the National Institute of Neurological Disorders and Stroke.* Pediatrics, 2007. **120**(3): p. 609-616.

20. Kirton, A., et al., *Presumed perinatal ischemic stroke: vascular classification predicts outcomes.* Annals of neurology, 2008. **63**(4): p. 436-443.

21. Victoria, T., et al., *Fetal magnetic resonance imaging: jumping from 1.5 to 3 tesla (preliminary experience).* Pediatric radiology, 2014. **44**(4): p. 376-386.

22. Welsh, R.C., U. Nemec, and M.E. Thomason, *Fetal magnetic resonance imaging at 3.0 T.* Topics in Magnetic Resonance Imaging, 2011. **22**(3): p. 119-131.

23. Lauterbur, P.C., *Image formation by induced local interactions. Examples employing nuclear magnetic resonance. 1973.* Clin Orthop Relat Res, 1989(244): p. 3-6.

24. OECD, *Magnetic resonance imaging (MRI) exams (indicator).* 2016.

25. Brown, R.W., et al., *Magnetic resonance imaging: physical principles and sequence design*. 2014: John Wiley & Sons.

26. Hennig, J., A. Nauerth, and H. Friedburg, *RARE imaging: a fast imaging method for clinical MR.* Magnetic resonance in medicine, 1986. **3**(6): p. 823-833.

27. Hennig, J. and H. Friedburg, *Clinical applications and methodological developments of the RARE technique.* Magnetic resonance imaging, 1988. **6**(4): p. 391-395.

28. Patel, M.R., et al., *Half-fourier acquisition single-shot turbo spin-echo (HASTE) MR: comparison with fast spin-echo MR in diseases of the brain.* American journal of neuroradiology, 1997. **18**(9): p. 1635-1640.

29. Vimercati, A., et al., *The diagnostic role of "in utero" magnetic resonance imaging.* J Perinat Med, 1999. **27**(4): p. 303-8.

30. Levine, D., et al., *Placenta accreta: evaluation with color Doppler US, power Doppler US, and MR imaging.* Radiology, 1997. **205**(3): p. 773-6.

31. Hubbard, A.M., T.M. Crombleholme, and N.S. Adzick, *Prenatal MRI evaluation of giant neck masses in preparation for the fetal exit procedure.* Am J Perinatol, 1998. **15**(4): p. 253-7.

32. Levine, D., *Ultrasound versus magnetic resonance imaging in fetal evaluation.* Top Magn Reson Imaging, 2001. **12**(1): p. 25-38.

33. Levine, D., et al., *Central nervous system abnormalities assessed with prenatal magnetic resonance imaging.* Obstet Gynecol, 1999. **94**(6): p. 1011-9.

34. Huisman, T.A., et al., *Fetal magnetic resonance imaging of the central nervous system: a pictorial essay.* Eur Radiol, 2002. **12**(8): p. 1952-61.

35. Sharma, G., et al., *Use of fetal magnetic resonance imaging in patients electing termination of pregnancy by dilation and evacuation.* Am J Obstet Gynecol, 2003. **189**(4): p. 990-3.

36. Baker, P.N., et al., *A three-year follow-up of children imaged in utero with echo-planar magnetic resonance.* Am J Obstet Gynecol, 1994. **170**(1 Pt 1): p. 32-3.

37. Fenton, B.W., et al., *Magnetic resonance spectroscopy to detect lecithin in amniotic fluid and fetal lung.* Obstet Gynecol, 2000. **95**(3): p. 457-60.

38. Duncan, K., P. Baker, and I. Johnson, *The complementary role of echoplanar magnetic resonance imaging and three-dimensional ultrasonography in fetal lung assessment.* Am J Obstet Gynecol, 1997. **177**(1): p. 244-5.

39. Duncan, K.R., et al., *The investigation of placental relaxation and estimation of placental perfusion using echo-planar magnetic resonance imaging.* Placenta, 1998. **19**(7): p. 539-43.

40. Duncan, K.R., et al., *Assessment of fetal lung growth in utero with echo-planar MR imaging.* Radiology, 1999. **210**(1): p. 197-200.

41. Baker, P.N., et al., *Estimation of fetal lung volume using echo-planar magnetic resonance imaging.* Obstet Gynecol, 1994. **83**(6): p. 951-4.

42. Langer, B., et al., *Low-field dedicated magnetic resonance imaging: a potential tool for assisting perinatal autopsy.* Ultrasound Obstet Gynecol, 1998. **12**(4): p. 271-5.

43. Malinger, G., et al., *Fetal brain imaging: a comparison between magnetic resonance imaging and dedicated neurosonography.* Ultrasound Obstet Gynecol, 2004. **23**(4): p. 333-40.

44. Malinger, G., D. Lev, and T. Lerman-Sagie, *Is fetal magnetic resonance imaging superior to neurosonography for detection of brain anomalies?* Ultrasound Obstet Gynecol, 2002. **20**(4): p. 317-21.

45. Manganaro, L., et al., *Role of foetal MRI in the evaluation of ischaemic-haemorrhagic lesions of the foetal brain.* Journal of Perinatal Medicine, 2012. **40**(4): p. 419-426.

46. Manganaro, L., et al., *Fetal MRI with diffusion-weighted imaging (DWI) and apparent diffusion coefficient (ADC) assessment in the evaluation of renal development: preliminary experience in normal kidneys.* Radiologia Medica, 2009. **114**(3): p. 403-13.

47. Manganaro, L., et al., *Diffusion-weighted MR imaging and apparent diffusion coefficient of the normal fetal lung: preliminary experience.* Prenatal Diagnosis, 2008. **28**(8): p. 745-748.

48. Johnson, I.R., et al., *Study of internal structure of the human fetus in utero by echo-planar magnetic resonance imaging.* Am J Obstet Gynecol, 1990. **163**(2): p. 601-7.

49. Gowland, P.A., et al., *In vivo relaxation time measurements in the human placenta using echo planar imaging at 0.5 T.* Magn Reson Imaging, 1998. **16**(3): p. 241-7.

50. Alderliesten, M.E., et al., *Perinatal mortality: clinical value of postmortem magnetic resonance imaging compared with autopsy in routine obstetric practice.* BJOG, 2003. **110**(4): p. 378-82.

51. Huisman, T.A., et al., *MR autopsy in fetuses.* Fetal Diagn Ther, 2002. **17**(1): p. 58-64.

52. Meyer-Wittkopf, M., et al., *Evaluation of three-dimensional ultrasonography and magnetic resonance imaging in assessment of congenital heart anomalies in fetal cardiac specimens.* Ultrasound Obstet Gynecol, 1996. **8**(5): p. 303-8.

53. Lee, W., et al., *A diagnostic approach for the evaluation of spina bifida by three-dimensional ultrasonography.* J Ultrasound Med, 2002. **21**(6): p. 619-26.

54. Lee, W., et al., *Non-invasive fetal lung assessment using diffusion-weighted imaging.* Ultrasound in Obstetrics & Gynecology, 2009. **34**(6): p. 673-677.

55. Kok, R.D., et al., *Decreased relative brain tissue levels of inositol in fetal hydrocephalus.* Am J Obstet Gynecol, 2003. **188**(4): p. 978-80.

56. Kadri, M., et al., *Proton magnetic resonance spectroscopy improves outcome prediction in perinatal CNS insults.* J Perinatol, 2003. **23**(3): p. 181-5.

57. Emamian, S.A., et al., *Fetal MRI evaluation of an intracranial mass: in utero evolution of hemorrhage.* Pediatr Radiol, 2002. **32**(8): p. 593-7.

58. Kathary, N., et al., *MRI imaging of fetal neck masses with airway compromise: utility in delivery planning.* Pediatr Radiol, 2001. **31**(10): p. 727-31.

59. Tanaka, Y.O., et al., *High temporal resolution dynamic contrast MRI in a high risk group for placenta accreta.* Magn Reson Imaging, 2001. **19**(5): p. 635-42.

60. Regan, F., J. Cavaluzzi, and B. Nguyen, *Fast MR abdominal imaging using the HASTE sequence.* AJR Am J Roentgenol, 1998. **170**(6): p. 1471-6.

61. Yamashita, Y., et al., *MR imaging of the fetus by a HASTE sequence.* AJR Am J Roentgenol, 1997. **168**(2): p. 513-9.

62. Whitby, E.H., et al., *Comparison of ultrasound and magnetic resonance imaging in 100 singleton pregnancies with suspected brain abnormalities.* BJOG, 2004. **111**(8): p. 784-92.

63. Laurichesse Delmas, H., et al., *Prenatal diagnosis of thrombosis of the dural sinuses: report of six cases, review of the literature and suggested management.* Ultrasound Obstet Gynecol, 2008. **32**(2): p. 188-98.

64. Powell, M.C., et al., *Magnetic resonance imaging (MRI) in obstetrics. II. Fetal anatomy.* Br J Obstet Gynaecol, 1988. **95**(1): p. 38-46.

65. Mansfield, P., et al., *Echo planar imaging of the human fetus in utero at 0.5 T.* Br J Radiol, 1990. **63**(755): p. 833-41.

66. Stehling, M.K., et al., *Echo-planar imaging of the human fetus in utero.* Magn Reson Med, 1990. **13**(2): p. 314-8.

67. Baldoli, C., et al., *Demonstration of acute ischemic lesions in the fetal brain by diffusion magnetic resonance imaging.* Ann Neurol, 2002. **52**(2): p. 243-6.

68. Guimiot, F., et al., *Contribution of diffusion-weighted imaging in the evaluation of diffuse white matter ischemic lesions in fetuses: correlations with fetopathologic findings.* AJNR Am J Neuroradiol, 2008. **29**(1): p. 110-5.

69. Righini, A., et al., *Diffusion-weighted magnetic resonance imaging of acute hypoxic-ischemic cerebral lesions in the survivor of a monochorionic twin pregnancy: case report.* Ultrasound Obstet Gynecol, 2007. **29**(4): p. 453-6.

70. Oubel, E., et al., *Reconstruction of scattered data in fetal diffusion MRI.* Med Image Comput Comput Assist Interv, 2010. **13**(Pt 1): p. 574-81.

71. Oubel, E., et al., *Reconstruction of scattered data in fetal diffusion MRI.* Med Image Anal, 2012. **16**(1): p. 28-37.

72. Oubel, E., et al., *Evaluation of different strategies for distortion correction in fetal diffusion-weighted imaging*, in *MICCAI workshop: Image Analysis for the Developing Brain*. 2009: London, U.K.

73. Jiang, S., et al., *In-utero three dimension high resolution fetal brain diffusion tensor imaging.* Med Image Comput Comput Assist Interv, 2007. **10**(Pt 1): p. 18-26.

74. Jiang, S., et al., *Diffusion tensor imaging (DTI) of the brain in moving subjects: application to in-utero fetal and ex-utero studies.* Magn Reson Med, 2009. **62**(3): p. 645-55.

75. Moore, R.J., et al., *In vivo diffusion measurements as an indication of fetal lung maturation using echo planar imaging at 0.5T.* Magnetic Resonance in Medicine, 2001. **45**(2): p. 247-253.

76. Moore, R.J., et al., *In utero perfusing fraction maps in normal and growth restricted pregnancy measured using IVIM echo-planar MRI.* Placenta, 2000. **21**(7): p. 726-32.

77. Francis, S.T., et al., *Non-invasive mapping of placental perfusion.* Lancet, 1998. **351**(9113): p. 1397-9.

78. Moore, R.J., et al., *Antenatal determination of fetal brain activity in response to an acoustic stimulus using functional magnetic resonance imaging.* Hum Brain Mapp, 2001. **12**(2): p. 94-99.

79. Wedegartner, U., et al., *Functional MR imaging: comparison of BOLD signal intensity changes in fetal organs with fetal and maternal oxyhemoglobin saturation during hypoxia in sheep.* Radiology, 2006. **238**(3): p. 872-80.

80. Fulford, J., et al., *Fetal brain activity in response to a visual stimulus.* Hum Brain Mapp, 2003. **20**(4): p. 239-45.

81. Gowland, P. and J. Fulford, *Initial experiences of performing fetal fMRI.* Exp Neurol, 2004. **190 Suppl 1**: p. S22-7.

82. Thomason, M.E., et al., *Cross-hemispheric functional connectivity in the human fetal brain.* Sci Transl Med, 2013. **5**(173): p. 173ra24.

83. van Cappellen van Walsum, A.M., et al., *Proton magnetic resonance spectroscopy of fetal lamb brain during hypoxia.* Am J Obstet Gynecol, 1998. **179**(3 Pt 1): p. 756-7.

84. Fenton, B.W., et al., *The fetus at term: in utero volume-selected proton MR spectroscopy with a breath-hold technique--a feasibility study.* Radiology, 2001. **219**(2): p. 563-6.

85. Girard, N., et al., *MRS of normal and impaired fetal brain development.* Eur J Radiol, 2006. **57**(2): p. 217-25.

86. Kimura, H., et al., *Metabolic alterations in the neonate and infant brain during development: evaluation with proton MR spectroscopy.* Radiology, 1995. **194**(2): p. 483-9.

87. Girard, N., et al., *Assessment of normal fetal brain maturation in utero by proton magnetic resonance spectroscopy.* Magn Reson Med, 2006. **56**(4): p. 768-75.

88. Brighina, E., et al., *Human Fetal Brain Chemistry as Detected by Proton Magnetic Resonance Spectroscopy.* Pediatr Neurol, 2009. **40**(5): p. 327-342.

89. Cetin, I., et al., *Lactate detection in the brain of growth-restricted fetuses with magnetic resonance spectroscopy.* Am J Obstet Gynecol, 2011. **205**(4): p. 350 e1-7.

90. Clouchoux, C. and C. Limperopoulos, *Novel applications of quantitative MRI for the fetal brain.* Pediatr Radiol, 2012. **42**: p. 24-32.

91. Heerschap, A., R.D. Kok, and P.P. van den Berg, *Antenatal proton MR spectroscopy of the human brain in vivo.* Childs Nerv Syst, 2003. **19**(7-8): p. 418-21.

92. Kok, R.D., et al., *Maturation of the human fetal brain as observed by H-1 MR spectroscopy.* Magnetic Resonance in Medicine, 2002. **48**(4): p. 611-616.

93. Nemec, S.F., et al., *Abnormalities of the penis in utero--hypospadias on fetal MRI.* J Perinat Med, 2011. **39**(4): p. 451-6.

94. Matsuda, H., et al., *Cerebral edema on MRI in severe preeclamptic women developing eclampsia.* J Perinat Med, 2005. **33**(3): p. 199-205.

95. Ikeda, K., et al., *Intrauterine MRI with single-shot fast-spin echo imaging showed different signal intensities in hypoplastic lungs.* J Perinat Med, 2000. **28**(2): p. 151-4.

96. Trop, I. and D. Levine, *Normal fetal anatomy as visualized with fast magnetic resonance imaging.* Top Magn Reson Imaging, 2001. **12**(1): p. 3-17.

97. Levine, D., *Atlas of fetal MRI*. 2005, Boca Raton: Taylor & Francis. 1 online resource (xi, 239 p.).

98. Levine, D., et al., *Fetal central nervous system anomalies: MR imaging augments sonographic diagnosis.* Radiology, 1997. **204**(3): p. 635-42.

99. Kubik-Huch, R.A., et al., *Ultrafast MR imaging of the fetus.* AJR Am J Roentgenol, 2000. **174**(6): p. 1599-606.

100. Prayer, D., *Fetal MRI*. 2011: Springer.

101. Debillon, T., et al., *Limitations of ultrasonography for diagnosing white matter damage in preterm infants.* Arch Dis Child Fetal Neonatal Ed, 2003. **88**(4): p. F275-9.

102. Inder, T.E., et al., *White matter injury in the premature infant: a comparison between serial cranial sonographic and MR findings at term.* AJNR Am J Neuroradiol, 2003. **24**(5): p. 805-9.

103. Jung, E., et al., *Spontaneous resolution of prenatally diagnosed dural sinus thrombosis: a case report.* Ultrasound Obstet Gynecol, 2006. **27**(5): p. 562-5.

104. Ghi, T., et al., *Outcome of antenatally diagnosed intracranial hemorrhage: case series and review of the literature.* Ultrasound Obstet Gynecol, 2003. **22**(2): p. 121-30.

105. Smith, F.W., A.H. Adam, and W.D. Phillips, *NMR imaging in pregnancy.* Lancet, 1983. **1**(8314-5): p. 61-2.

106. Filippi, C.G., et al. *Fetal Imaging with Multitransmit MR at 3.0T: Preliminary Findings*. in *Joint Annual Meeting ISMRM-ESMRMB 2010*. 2010. Stockholm, Sweden: Poster# 2023.

107. Barr, S.M., et al., *Assessment of intra-hepatic and intra-muscular lipid in obese pregnant women: an application of 3-tesla MRI.* Archives of Disease in Childhood - Fetal and Neonatal Edition, 2011. **96**(Suppl 1): p. Fa118.

108. Welsh, R.C., U. Nemec, and M.E. Thomason, *Fetal magnetic resonance imaging at 3.0 T.* Top Magn Reson Imaging, 2011. **22**(3): p. 119-31.

109. Victoria, T., et al., *Fetal magnetic resonance imaging: jumping from 1.5 to 3 tesla (preliminary experience).* Pediatr Radiol, 2014. **44**(4): p. 376-86.

110. Wardlaw, J.M., et al., *A systematic review of the utility of 1.5 versus 3 Tesla magnetic resonance brain imaging in clinical practice and research.* European Radiology, 2012. **22**(11): p. 2295-2303.

111. Wood, R., et al., *1.5 tesla magnetic resonance imaging scanners compared with 3.0 tesla magnetic resonance imaging scanners: systematic review of clinical effectiveness.* CADTH Technol Overv, 2012. **2**(2): p. e2201.

112. Knickmeyer, R.C., et al., *A structural MRI study of human brain development from birth to 2 years.* J Neurosci, 2008. **28**(47): p. 12176-82.

113. Gilmore, J.H., et al., *3 Tesla magnetic resonance imaging of the brain in newborns.* Psychiatry Res, 2004. **132**(1): p. 81-5.

114. Alvarez-Linera, J., *3T MRI: advances in brain imaging.* Eur J Radiol, 2008. **67**(3): p. 415-26.

115. Machann, J., H.P. Schlemmer, and F. Schick, *Technical challenges and opportunities of whole-body magnetic resonance imaging at 3T.* Phys Med, 2008. **24**(2): p. 63-70.

116. Soher, B.J., B.M. Dale, and E.M. Merkle, *A review of MR physics: 3T versus 1.5T.* Magn Reson Imaging Clin N Am, 2007. **15**(3): p. 277-90, v.

117. Akisik, F.M., et al., *Abdominal MR Imaging at 3.0 T.* Radiographics, 2007. **27**(5).

118. Hoult, D.I., *Sensitivity and power deposition in a high-field imaging experiment.* Journal of Magnetic Resonance Imaging, 2000. **12**(1): p. 46-67.

119. Hoult, D.I. and P.C. Lauterbur, *Sensitivity of the Zeugmatographic Experiment Involving Human Samples.* J Magn Reson, 1979. **34**(2): p. 425-433.

120. Roschmann, P., *Radiofrequency Penetration and Absorption in the Human-Body - Limitations to High-Field Whole-Body Nuclear-Magnetic-Resonance Imaging.* Med Phys, 1987. **14**(6): p. 922-931.

121. *Institute of Electrical and Electronic Engineers (IEEE) 2002 IEEE recommended practice for measurements and computations of radio frequency electromagnetic fields with respect to human exposure to such fields, 100 kHz– 300 GHz.* IEEE C95.3-2002 (New York: IEEE).

122. *International Commission on Non-Ionizing Radiation Protection (ICNIRP) 2009a ICNIRP statement on the 'Guidelines for limiting exposure to time-varying electric, magnetic, and electromagnetic fields (up to 300 GHz)'* Health Physics, 2009a. **97**: p. 257-258.

123. *International Commission on Non-Ionizing Radiation Protection (ICNIRP) 2009b Amendment to the ICNIRP 'Statement on medical Magnetic Resonance (MR) procedures: protection of patients'* Health Physics, 2009b. **97**: p. 259-61.

124. Neelavalli, J., *T1 and susceptibility contrast at high fields*. 2008. p. 110 p.

125. Sarkar, S.N., et al., *Brain MR Imaging at Ultra-low Radiofrequency Power.* Radiology, 2011. **259**(2): p. 550-557.

126. Busse, R.F., *Reduced RF power without blurring: Correcting for modulation of refocusing flip angle in FSE sequences.* Magnetic Resonance in Medicine, 2004. **51**(5): p. 1031-1037.

127. Hennig, J., M. Weigel, and K. Scheffler, *Multiecho sequences with variable refocusing flip angles: Optimization of signal behavior using smooth transitions between pseudo steady states (TRAPS).* Magnetic Resonance in Medicine, 2003. **49**(3): p. 527-535.

128. Brugger, P.C. and D. Prayer, *Actual imaging time in fetal MRI.* Eur J Radiol, 2012. **81**(3): p. e194-6.

129. Elmaoğlu, M. and A. Çelik, *MRI handbook : MR physics, patient positioning, and protocols*. 2012, New York: Springer. xii, 318 p.

130. Hussain, S.M., et al., *MR imaging of the female pelvis at 3T.* Magn Reson Imaging Clin N Am, 2006. **14**(4): p. 537-44, vii.

131. Kataoka, M., et al., *MR imaging of the female pelvis at 3 Tesla: Evaluation of image homogeneity using different dielectric pads.* Journal of Magnetic Resonance Imaging, 2007. **26**(6): p. 1572-1577.

132. National Electrical Manufacturers Association. and American College of Radiology., *Digital imaging and communications in medicine (DICOM)*. 1998, Washington, D.C.: National Electrical Manufacturers Association. v. <1-8, 10-15>.

133. Hand, J., Y. Li, and J. Hajnal, *Numerical study of RF exposure and the resulting temperature rise in the foetus during a magnetic resonance procedure.* Physics in medicine and biology, 2010. **55**(4): p. 913.

134. Kikuchi, S., et al., *Temperature elevation in the fetus from electromagnetic exposure during magnetic resonance imaging.* Phys Med Biol, 2010. **55**(8): p. 2411-26.

135. Hirata, A., et al., *The relationship between specific absorption rate and temperature elevation in anatomically based human body models for plane wave exposure from 30 MHz to 6 GHz.* Physics in medicine and biology, 2013. **58**(4): p. 903.

136. Levine, D., et al., *Fetal fast MR imaging: reproducibility, technical quality, and conspicuity of anatomy.* Radiology, 1998. **206**(2): p. 549-54.

137. Troiano, R.N., R.C. Lange, and S. McCarthy, *Conspicuity of normal and pathologic female pelvic anatomy: comparison of gadolinium-enhanced T1-weighted images and fast spin echo T2-weighted images.* J Comput Assist Tomogr, 1996. **20**(6): p. 871-7.

138. Bottomley, P.A., et al., *A Review of Normal Tissue Hydrogen Nmr Relaxation-Times and Relaxation Mechanisms from 1-100 Mhz - Dependence on Tissue-Type, Nmr Frequency, Temperature, Species, Excision, and Age.* Med Phys, 1984. **11**(4): p. 425-448.

139. Stanisz, G.J., et al., *T-1, T-2 relaxation and magnetization transfer in tissue at 3T.* Magnetic Resonance in Medicine, 2005. **54**(3): p. 507-512.

140. Wansapura, J.P., et al., *NMR relaxation times in the human brain at 3.0 tesla.* Jmri-Journal of Magnetic Resonance Imaging, 1999. **9**(4): p. 531-538.

141. Wang, Z.W. and J.C. Lin, *SAR Calculations in MRI Scanning Systems.* Ieee Microwave Magazine, 2012. **13**(5): p. 22-29.

142. Edelstein, W.A., et al., *The Intrinsic Signal-to-Noise Ratio in Nmr Imaging.* Magnetic Resonance in Medicine, 1986. **3**(4): p. 604-618.

143. Kiefer B, Grassner J, and Hausman K, *Image acquisition in a second with half Fourier acquisition single shot turbo spin echo.* J Magn Reson Imaging, 1994. **4 (P):86**.

144. Semelka, R.C., et al., *HASTE MR imaging: description of technique and preliminary results in the abdomen.* J Magn Reson Imaging, 1996. **6**(4): p. 698-9.

145. Hennig, J. and K. Scheffler, *Hyperechoes.* Magn Reson Med, 2001. **46**(1): p. 6-12.

146. *A Primer on Medical Device Interactions with Magnetic Resonance Imaging Systems*. 1997; Available from: http://www.fda.gov/MedicalDevices/DeviceRegulationandGuidance/GuidanceDocuments/ucm107721.htm.

147. *Guidance for Industry and FDA Staff: Criteria for Significant Risk Investigations of Magnetic Resonance Diagnostic Devices*. 2003; Available from: http://www.fda.gov/MedicalDevices/DeviceRegulationandGuidance/GuidanceDocuments/ucm072686.htm.

148. Brugger, P.C. and D. Prayer, *Actual imaging time in fetal MRI.* Eur J Radiol, 2012. **81**(3): p. E194-E196.

149. Bhide, A., et al., *ISUOG practice guidelines: use of Doppler ultrasonography in obstetrics.* Ultrasound in obstetrics & gynecology: the official journal of the International Society of Ultrasound in Obstetrics and Gynecology, 2013. **41**(2): p. 233.

150. Kypros Nicolaides, G.R., Kurt Hecher and Renato Ximenes, *Doppler ultrasound -Diploma in fetal medicine & ISUOG educational series*, in *Doppler in Obstetrics*, K. Nicolaides, Editor. 2002.

151. LAURIN, J., et al., *Ultrasound measurement of fetal blood flow in predicting fetal outcome.* BJOG: An International Journal of Obstetrics & Gynaecology, 1987. **94**(10): p. 940-948.

152. Baschat, A., et al., *Relationship between arterial and venous Doppler and perinatal outcome in fetal growth restriction.* Ultrasound in obstetrics & gynecology, 2000. **16**(5): p. 407-413.

153. Swillens, A., et al. *The accuracy of volume flow measurements derived from pulsed wave Doppler: a study in the complex setting of forearm vascular access for hemodialysis*. in *2012 IEEE International Ultrasonics Symposium*. 2012. IEEE.

154. Quinn, T.M., A.M. Hubbard, and N.S. Adzick, *Prenatal magnetic resonance imaging enhances fetal diagnosis.* Journal of pediatric surgery, 1998. **33**(4): p. 553-558.

155. Breysem, L., et al., *The value of fast MR imaging as an adjunct to ultrasound in prenatal diagnosis.* European radiology, 2003. **13**(7): p. 1538-1548.

156. Prsa, M., et al., *Reference Ranges of Blood Flow in the Major Vessels of the Normal Human Fetal Circulation at Term by Phase-Contrast Magnetic Resonance ImagingCLINICAL PERSPECTIVE.* Circulation: Cardiovascular Imaging, 2014. **7**(4): p. 663-670.

157. Seed, M., et al., *Feasibility of quantification of the distribution of blood flow in the normal human fetal circulation using CMR: a cross-sectional study.* Journal of Cardiovascular Magnetic Resonance, 2012. **14**(1): p. 79.

158. Tsai-Goodman, B., et al., *Foetal blood flow measured using phase contrast cardiovascular magnetic resonance–preliminary data comparing 1.5 T with 3.0 T.* Journal of Cardiovascular Magnetic Resonance, 2015. **17**(1): p. 30.

159. Schoennagel, B.P., et al., *Fetal blood flow velocimetry by phase-contrast MRI using a new triggering method and comparison with Doppler ultrasound in a sheep model: a pilot study.* Magnetic Resonance Materials in Physics, Biology and Medicine, 2014. **27**(3): p. 237-244.

160. KORDING, F., et al., *Doppler Ultrasound Triggering for Cardiovascular MRI at 3T in a Healthy Volunteer Study.* Magnetic Resonance in Medical Sciences, 2016(0).

161. Bakker, C., et al., *Accuracy and precision of time-averaged flow as measured by nontriggered 2D phase-contrast MR angiography, a phantom evaluation.* Magnetic resonance imaging, 1995. **13**(7): p. 959-965.

162. Hangiandreou, N.J., P.J. Rossman, and S.J. Riederer, *Analysis of MR phase-contrast measurements of pulsatile velocity waveforms.* Journal of Magnetic Resonance Imaging, 1993. **3**(2): p. 387-394.

163. Yeh, S.-Y., A. Forsythe, and E.H. Hon, *Quantification of fetal heart beat-to-beat interval differences.* Obstetrics & Gynecology, 1973. **41**(3): p. 355-363.

164. Jiang, J., et al., *Quantifying errors in flow measurement using phase contrast magnetic resonance imaging: comparison of several boundary detection methods.* Magnetic resonance imaging, 2015. **33**(2): p. 185-193.

165. Neelavalli, J., et al., *Magnetic resonance angiography of fetal vasculature at 3.0 T.* European radiology, 2016. **26**(12): p. 4570-4576.

166. Feng, W., et al., *Characteristics of flow through the internal jugular veins at cervical C2/C3 and C5/C6 levels for multiple sclerosis patients using MR phase contrast imaging.* Neurological research, 2012. **34**(8): p. 802-809.

167. Bakker, C.J., R.M. Hoogeveen, and M.A. Viergever, *Construction of a protocol for measuring blood flow by two-dimensional phase-contrast MRA.* Journal of Magnetic Resonance Imaging, 1999. **9**(1): p. 119-127.

168. Lees, C., et al., *Assessment of umbilical arterial and venous flow using color Doppler.* Ultrasound in obstetrics & gynecology, 1999. **14**(4): p. 250-255.

169. Acharya, G., et al., *Reference ranges for umbilical vein blood flow in the second half of pregnancy based on longitudinal data.* Prenatal diagnosis, 2005. **25**(2): p. 99-111.

170. Portnoy, S., et al., *Relaxation properties of human umbilical cord blood at 1.5 Tesla.* Magnetic resonance in medicine, 2016.

171. Enzmann, D.R., M.P. Marks, and N.J. Pelc, *Comparison of cerebral artery blood flow measurements with gated cine and ungated phase-contrast techniques.* Journal of Magnetic Resonance Imaging, 1993. **3**(5): p. 705-712.

172. Minette, M.S. and D.J. Sahn, *Ventricular septal defects.* Circulation, 2006. **114**(20): p. 2190-2197.

173. Savelli, S., et al., *Fetal mid-muscular ventricular septal defect: Role of fetal cardio-vascular evaluation with magnetic resonance (MR) imaging and MR-angiography.* European Journal of Radiology Extra, 2009. **69**(3): p. e101-e103.

174. Malian, V. and J.E. Lee, *MR imaging and MR angiography of an abdominal pregnancy with placental infarction.* American Journal of Roentgenology, 2001. **177**(6): p. 1305-1306.

175. Goncalves, L.F., et al., *Four-dimensional ultrasonography of the fetal heart using color Doppler spatiotemporal image correlation.* J Ultrasound Med, 2004. **23**(4): p. 473-81.

176. Goncalves, L.F., et al., *Four-dimensional ultrasonography of the fetal heart with spatiotemporal image correlation.* Am J Obstet Gynecol, 2003. **189**(6): p. 1792-802.

177. Yagel, S., et al., *3D and 4D ultrasound in fetal cardiac scanning: a new look at the fetal heart.* Ultrasound in obstetrics & gynecology, 2007. **29**(1): p. 81-95.

178. Hendler, I., et al., *Suboptimal Second-Trimester Ultrasonographic Visualization of the Fetal Heart in Obese Women Should We Repeat the Examination?* Journal of ultrasound in medicine, 2005. **24**(9): p. 1205-1209.

179. Radiology, A.C.o. *ACR-SPR practice parameter for the safe and optimal performance of fetal magnetic resonance imaging (MRA)*. 2015.

180. Malinger, G., et al., *Fetal brain imaging: a comparison between magnetic resonance imaging and dedicated neurosonography.* Ultrasound in obstetrics & gynecology, 2004. **23**(4): p. 333-340.

181. Levine, D., *Ultrasound versus magnetic resonance imaging in fetal evaluation.* Topics in Magnetic Resonance Imaging, 2001. **12**(1): p. 25-38.

182. *Fetal MRI*. 1 ed. Diagnostic Imaging, ed. D. Wimberger-Prayer. 2001: Springer-Verlag Berlin Heidelberg. XIII, 528.

183. Yamamura, J., et al., *Magnetic resonance angiography of fetal vessels: feasibility study in the sheep fetus.* Jpn J Radiol, 2010. **28**(10): p. 720-6.

184. Krishnamurthy, U., et al., *MR imaging of the fetal brain at 1.5 T and 3.0 T field strengths: comparing specific absorption rate (SAR) and image quality.* Journal of perinatal medicine, 2015. **43**(2): p. 209-220.

185. Victoria, T., et al., *Fetal magnetic resonance imaging: jumping from 1.5 to 3 tesla (preliminary experience).* Pediatr Radiol, 2014. **44**(4): p. 376-86; quiz 373-5.

186. Zungho Zun, A.S., Dorothy Bulas, Adre J. Du Plessis, Catherine Limperopoulos. *Three-dimensional placental perfusion imaging using velocity-selective arterial spin labeled MRI: Preliminary results*. in *ISPD 19th International Conference on Prenatal Diagnosis and Therapy*. 2015. Washington, DC, USA.

187. Uday Krishnamurthy, W.F., Jaladhar Neelavalli, Pavan Kumar Jella, Ehsan Hamtaei, Edgar Hernandez-Andrade, Swati Mody, Lami Yeo, Ewart Mark Haacke, and Roberto Romero. *Quantitative flow imaging in the human umbilical vessels in-utero using non-triggered phase contrast MRI*. in *Joint Annual Meeting ISMRM-ESMRMB*. 2014. Milan, Italy.

188. Neelavalli, J., et al., *Measuring venous blood oxygenation in fetal brain using susceptibility-weighted imaging.* Journal of Magnetic Resonance Imaging, 2014. **39**(4): p. 998-1006.

189. Bilardo, C.M., S. Campbell, and K.H. Nicolaides, *Mean blood velocities and flow impedance in the fetal descending thoracic aorta and common carotid artery in normal pregnancy.* Early human development, 1988. **18**(2): p. 213-221.

190. Weissman, A., et al., *Sonographic measurements of the umbilical cord and vessels during normal pregnancies.* J Ultrasound Med, 1994. **13**(1): p. 11-4.

191. Seydel, H.G., *The Diameters of the Cerebral Arteries of the Human Fetus.* Anat Rec, 1964. **150**: p. 79-88.

192. Cartier, M.S., et al., *The normal diameter of the fetal aorta and pulmonary artery: echocardiographic evaluation in utero.* AJR Am J Roentgenol, 1987. **149**(5): p. 1003-7.

193. Spees, W.M., et al., *Water proton MR properties of human blood at 1.5 Tesla: Magnetic susceptibility, T1, T2, T* 2, and non-Lorentzian signal behavior.* Magnetic resonance in medicine, 2001. **45**(4): p. 533-542.

194. De Vis, J.B., et al., *Impact of neonate haematocrit variability on the longitudinal relaxation time of blood: Implications for arterial spin labelling MRI.* Neuroimage Clin, 2014. **4**: p. 517-25.

195. Williams, L.-A., et al., *Neonatal Brain: Regional Variability of in Vivo MR Imaging Relaxation Rates at 3.0 T—Initial Experience 1.* Radiology, 2005. **235**(2): p. 595-603.

196. Jones, R.A., S. Palasis, and J.D. Grattan-Smith, *MRI of the neonatal brain: optimization of spin-echo parameters.* American Journal of Roentgenology, 2004. **182**(2): p. 367-372.

197. Atlas, S.W., *Magnetic resonance imaging of the brain and spine*. Vol. 1. 2009: Lippincott Williams & Wilkins.

198. Li, D., Y. Wang, and D.J. Waight, *Blood oxygen saturation assessment in vivo using T2* estimation.* Magnetic resonance in medicine, 1998. **39**(5): p. 685-690.

199. Ibanez, S., Ng, Cates., *The ITK Software Guide*. 2005: Kitware Inc.

200. Haacke, E.M., G.W. Lenz, and A.D. Nelson, *Pseudo-gating: Elimination of periodic motion artifacts in magnetic resonance imaging without gating.* Magnetic resonance in medicine, 1987. **4**(2): p. 162-174.

201. Salafia, C.M., et al., *Placental surface shape, function, and effects of maternal and fetal vascular pathology.* Placenta, 2010. **31**(11): p. 958-62.

202. Yampolsky, M., et al., *Centrality of the umbilical cord insertion in a human placenta influences the placental efficiency.* Placenta, 2009. **30**(12): p. 1058-64.

203. Edelman, R.R., et al., *Quiescent-inflow single-shot magnetic resonance angiography using a highly undersampled radial k-space trajectory.* Magnetic Resonance in Medicine, 2013. **70**(6): p. 1662-1668.

204. Glover, G. and J. Pauly, *Projection reconstruction techniques for reduction of motion effects in MRI.* Magnetic Resonance in Medicine, 1992. **28**(2): p. 275-289.

205. Meyer, C.H., et al., *Fast spiral coronary artery imaging.* Magnetic Resonance in Medicine, 1992. **28**(2): p. 202-213.

206. Shankaranarayanan, A., et al., *Two-step navigatorless correction algorithm for radial k-space MRI acquisitions.* Magnetic resonance in medicine, 2001. **45**(2): p. 277-288.

207. Arunachalam, A., A. Samsonov, and W.F. Block, *Self-calibrated GRAPPA method for 2D and 3D radial data.* Magnetic resonance in medicine, 2007. **57**(5): p. 931-938.

208. Lee, J.H., J.M. Pauly, and D.G. Nishimura, *Partial k-space reconstruction for radial k-space trajectories in magnetic resonance imaging*. 2007, Google Patents.

209. Hamtaei, E.N., Jaladhar ; Jella, Pavan ; Krishnamurthy, Uday ; Yadav, Brijesh ; Cabrera, Maria ; Ehterami, Shadi ; Hernandez, Edgar ; Lami, Yeo ; Mody, Swathi ; Hassan, Sonia ; Haacke, Mark ; Romero, Robert. *Compressed Sensing MRA in the Human Fetus*. in *36th annual international conference of the IEEE engineering in medicine and biology society*. 2014. Chicago, IL.

210. Lustig, M., et al., *Compressed sensing MRI.* IEEE Signal Processing Magazine, 2008. **25**(2): p. 72-82.

211. Hata, N., et al., *Non-gated fetal MRI of umbilical blood flow in an acardiac twin.* Pediatric radiology, 2005. **35**(8): p. 826-829.

212. Liu, J., et al., *Respiratory and cardiac self-gated free-breathing cardiac CINE imaging with multiecho 3D hybrid radial SSFP acquisition.* Magnetic resonance in medicine, 2010. **63**(5): p. 1230-1237.

213. Hiba, B., et al., *Cardiac and respiratory double self-gated cine MRI in the mouse at 7 T.* Magnetic resonance in medicine, 2006. **55**(3): p. 506-513.

214. Nezafat, R., et al., *Real-time blood flow imaging using autocalibrated spiral sensitivity encoding.* Magnetic resonance in medicine, 2005. **54**(6): p. 1557-1561.

215. Neelavalli, J., et al., *OC11. 08: Estimation of the cerebral metabolic rate of oxygen (CMRO2) in the human fetus.* Ultrasound in Obstetrics & Gynecology, 2015. **46**(S1): p. 25-25.

216. Wang, J., *Issues with radiofrequency heating in MRI.* Journal of Applied Clinical Medical Physics, 2014. **15**(5).

217. Bottomley, P.A., *Turning up the heat on MRI.* Journal of the American College of Radiology: JACR, 2008. **5**(7): p. 853.

218. Protection, I.C.o.N.-I.R., *Amendment to the ICNIRP "Statement on medical magnetic resonance (MR) procedures: protection of patients".* Health Physics, 2009. **97**(3): p. 259-261.

219. Protection, I.C.o.N.-I.R., *Medical magnetic resonance (MR) procedures: protection of patients.* Health Physics, 2004. **87**(2): p. 197-216.

220. Gandhi, O.P., *State of the knowledge for electromagnetic absorbed dose in man and animals.* Proceedings of the IEEE, 1980. **68**(1): p. 24-32.

221. Dimbylow, P.J., T. Nagaoka, and X.G. Xu, *A comparison of foetal SAR in three sets of pregnant female models.* Physics in medicine and biology, 2009. **54**(9): p. 2755.

222. Kikuchi, S., et al., *Temperature elevation in the fetus from electromagnetic exposure during magnetic resonance imaging.* Physics in medicine and biology, 2010. **55**(8): p. 2411.

223. Cannie, M.M., et al., *Potential heating effect in the gravid uterus by using 3-T MR imaging protocols: experimental study in miniature pigs.* Radiology, 2015. **279**(3): p. 754-761.

224. Levine, D., et al., *Potential heating effect in the gravid uterus during MR HASTE imaging.* Journal of Magnetic Resonance Imaging, 2001. **13**(6): p. 856-861.

225. Gowland, P. and J. De Wilde, *Temperature increase in the fetus due to radio frequency exposure during magnetic resonance scanning.* Physics in medicine and biology, 2008. **53**(21): p. L15.

226. Voigt, T., et al., *Patient-individual local SAR determination: In vivo measurements and numerical validation.* Magnetic resonance in medicine, 2012. **68**(4): p. 1117-1126.

227. Jin, J., et al., *Improving SAR estimations in MRI using subject-specific models.* Physics in medicine and biology, 2012. **57**(24): p. 8153.

228. Winkler, S.A., et al., *Direct SAR mapping by thermoacoustic imaging: a feasibility study.* Magnetic Resonance in Medicine, 2016.

229. Oh, S., et al., *Measurement of SAR-induced temperature increase in a phantom and in vivo with comparison to numerical simulation.* Magnetic resonance in medicine, 2014. **71**(5): p. 1923-1931.

230. Simonis, F.F., et al., *Feasibility of measuring thermoregulation during RF heating of the human calf muscle using MR based methods.* Magnetic resonance in medicine, 2015.

ABSTRACT

MRI METHODS FOR IMAGING THE FETO-PLACENTAL VASCULATURE AND BLOOD FLOW

by

UDAY BHASKAR KRISHNAMURTHY

May 2017

Advisor: Dr. E Mark Haacke

Major: Biomedical Engineering (Dual title Biomedical Imaging Program)

Degree: Doctor of Philosophy

Fetal magnetic resonance imaging (MRI) in recent times has become a well-established adjunct to ultrasound (US) in routine clinical prenatal care and diagnostics. The majority of fetal MRI is restricted to T2-weighted scans, where the diagnosis is based on the appearance of normal and abnormal tissue. Although there have been many advancements in MRI and a plethora of sequences, that probe different anatomical and different physiological process, the adaptation of these in fetal imaging has been rather slow. Many of these can extract quantitative parameters that can throw light on the underlying tissue's normal/patho-physiology. But the use of such quantitative MRI methods has been extremely limited in fetal imaging due to its unique and dynamic physiological milieu that pose several technical challenges including low signal to noise and/or resolution, artifacts associated with abdominal imaging and most importantly fetal motion. These limitations are expected to be overcome by (a) optimizing and (b) developing novel MR imaging sequences, both of which constitute the primary aim of my work.

This work develops a framework that allows for vascular imaging in the fetus and placenta. This includes both qualitative vascular imaging and blood flow quantification. Towards this, three broad directions were explored (a) Moving to higher field imaging, while optimizing parameters for low energy deposition and (b) application of non-gated phase contrast MRI and (c) optimization of conventional time-of-flight angiography for fetal applications.

AUTOBIOGRAPHICAL STATEMENT

EDUCATION:

- 2011 – 2017 Ph.D., Biomedical Engineering, Wayne State University, Detroit, USA
- 2006 – 2010 B.S., Biomedical Engineering, Osmania University, Hyderabad, India.

PEER-REVIEWED PUBLICATIONS:

- **Krishnamurthy U**, Neelavalli J, Mody S, Yeo L, Jella PK, Saleem S, Korzeniewski SJ, Cabrera MD, Ehterami S, Bahado-singh RO, Katkuri Y, Haacke EM, Hernandez-Andrade E, Hassan SS, and Romero R.,"*MR Imaging of the Fetal Brain at 1.5T and 3.0T Field Strengths: Initial Experience with Specific Absorption Rate (SAR) and Image Quality*". Journal of Perinatal Medicine (2014).
- **Krishnamurthy U**, Szalai G, Neelavalli J, Shen Y, Chaiworapongsa T, Hernandez-Andrade E, Than NG, Wu Z, Yeo L, Haacke EM, and Romero R, "*Quantitative T2 changes and susceptibility weighted magnetic resonance imaging in the murine pregnancy*". Gynecologic and Obstetric Investigation, (2014).
- **Krishnamurthy U**, Neelavalli J, Szalai G, Shen Y, Wu Z, Yadav BK, Tarca AL, Chaiworapongsa T, Hernandez-Andrade E, Than NG, Haacke EM, and Romero R., "*Longitudinal Changes in Placental MRI Relaxation Parameter in Murine Pregnancy: Compartmental Analysis*". Gynecologic and Obstetric Investigation, (2015).
- Neelavalli J, **Krishnamurthy U**, Jella PK, Mody S, Yadav BK, Hendershot K, Hernandez-Andrade E, Yeo L, Cabrera M, Haacke EM, Hassan SS, Romero R., "*Magnetic resonance angiography of fetal vasculature at 3.0 T*". European Radiology (2016).
- Neelavalli J, Jella PK, **Krishnamurthy U**, Buch S, Mody S, Yeo L, Katkuri Y, Bahado-Singh RO, Hassan SS, Haacke EM, Romero R. and, Thomason M., "*Measuring Venous Blood Oxygenation in Fetal Brain using Susceptibility Weighted Imaging*". Journal of Magnetic Resonance Imaging, 39.4 (2014): 998-1006.
- Yadav BK, Neelavalli J., **Krishnamurthy U**, Szalai G, Shen Y, Nayak NR, ... & Romero R., "*A Longitudinal Study of Placental Perfusion Using Dynamic Contrast Enhanced Magnetic Resonance Imaging in Murine Pregnancy*". Placenta (2016).
- Munevar G, Cole ML, Ye Y, Yang Y, **Krishnamurthy U**, Haacke EM., "***fMRI** study of self vs. others' attributions of traits consistent with evolutionary understanding of the self*". Neuroscience Discovery, 2014; 2:3.

HONORS AND MERITS:

2016 Distinguished Achievement in Graduate Student Research, 56th Honors Convocation, WSU
2015 Best Oral Communication, 25th World Congress on Ultrasound in Obstetrics and Gynecology
Trainee Travel Award, Magnetic Resonance Angiography 27th Annual International Conference
Magna Cum Laude, Summa Cum laude (co-author), ISMRM, 23rd Annual Meeting
President's Award (co-author), SMRT, 24th Annual Meeting, Toronto, Canada
2014 Thomas Rumble University, Graduate Fellowship, WSU, Detroit, MI
2013 Best Poster Award, European Society of MRI in Neuropediatrics
2013 – 2015 Educational/travel Stipends from ISMRM
2010 Best Undergraduate Thesis Award, Osmania University
Biomedical Instrumentation Centre Gold Medal, Osmania University
Best Outgoing Student Award (2006 – 2010), Osmania University
Research Fellowship, Indian Academy of Science
All India design finalist in a biomedical design competition,
Cash award of INR 3000, Chennai, India